Dissertation zur Erlangung des Doktorgrades der Technischen Fakultät der Albert-Ludwigs-Universität Freiburg im Breisgau

Electronic Transport in Ordered Silicon Nanocrystal Networks

Sebastian Gutsch

Albert-Ludwigs-Universität Freiburg im Breisgau
Technische Fakultät
Institut für Mikrosystemtechnik

Dekan

Prof. Dr. Yiannos Manoli

Referenten

Prof. Dr. Margit Zacharias

Prof. Dr. Christoph Nebel

Datum der Disputation

28.02.2014

Contents

Abstract **1**

Zusammenfassung **3**

1 Introduction **5**

1.1 Charge Transport in Silicon Nanocrystal Ensembles 6
1.2 Demand of Silicon Nanocrystal Doping 7
1.3 Challenges of Doping Silicon Nanocrystals 8
1.4 Aims and Outline 10

2 Experimental Details **11**

2.1 Sample Fabrication 11
2.1.1 Method of Silicon Nanocrystal Preparation 11
2.1.2 Substrate Choice 12
2.1.3 Process Flow 12
2.2 Characterization Methods 13
2.2.1 Electrical Characterization 13
2.2.2 Photoluminescence Spectroscopy 15
2.2.3 Transmission Electron Microscopy 15
2.2.4 X-Ray Photoelectron Spectroscopy 17
2.2.5 X-Ray Absorption Spectroscopy 18
2.2.6 Molecular Cs^+ Secondary Ion Mass Spectrometry 19
2.2.7 Elastic Recoil Detection Analysis 19
2.2.8 Atom Probe Tomography 20

3 Material Properties of Silicon Nanocrystals **23**

3.1 Basic Structrual and Optical Properties of Intrinsic Silicon Nanocrystals 23
3.2 In-plane Order of Silicon Nanocrystals 26
3.3 Silicon Oxide Barrier Thickness Control 32
3.4 Phosphorus-doped Silicon Nanocrystals 36

3.4.1 Phosphorus Quantification 36
3.4.2 Localization of Phosphorus 38
3.4.2.1 X-Ray Photoelectron Spectroscopy 39
3.4.2.2 X-Ray Absorption Spectroscopy 40
3.4.2.3 Atom Probe Tomography 43
3.4.3 Photoluminescence Behaviour 51

4 Charge Transport 53
4.1 Microscopic Transport 53
4.1.1 Quantum Confinement 53
4.1.2 Charging of a single Silicon Nanocrystal 55
4.1.3 Configuration Coordinate Diagram 56
4.1.4 Fermi's Golden Rule and Marcus Equation 58
4.1.5 Reorganization Energy 59
4.1.6 Electronic Coupling between two Si Nanocrystals 60
4.1.7 Electron Transfer Time between Silicon Nanocrystals 62
4.1.8 The Effect of an Applied Electric Field 63
4.1.9 Interface Defects 66
4.2 Macroscopic Transport 67
4.3 Electrical Measurements 71
4.3.1 Space-Charge Effects 71
4.3.2 On the Role of Si Surface Defects 76
4.3.3 Effect of the Silicon Oxide Barrier Thickness 80
4.3.4 Effect of Silicon Nanocrystal Areal Density and Size 82
4.3.5 Phosphorus Doped Superlattices 85
4.4 Charge Transport Regimes and Mechanisms 88

5 Summary and Outlook 91

A Appendix 95
A.1 Calculation of the total Wave-function of a Spherical Si Nanocrystal Embedded in Silicon Dioxide 95
A.2 Numerical Calculation of Space-Charge-Limited Currents 97

Bibliography 99

List of Abbreviations 119

List of Symbols **121**

Publication List **123**

Acknowledgements **125**

Abstract

The present work deals with the structural and electrical characterization of size-controlled silicon nanocrystals. Superlattices consisting of alternating layers of silicon-rich oxynitride and silicon oxide are prepared by plasma-enhanced chemical vapor deposition. The subsequent high temperature annealing allows to precipate and crystallize ordered arrays of silicon nanocrystals in a silicon oxynitride matrix.

A detailed structural analysis is carried out using transmission electron microscopy leading to exceptional findings in terms of silicon nanocrystal size dispersion, shape and three-dimensional order. Furthermore, phosphorus doped silicon nanocrystals are prepared and investigated in terms of phosphorus quantification and localization within the films. By using X-ray absorption spectroscopy and atomprobe tomography it is found that phosphorus is incorporated into the silicon nanocrystals, but also strongly segregates at the nanocrystalline Si/SiO_2 interface.

Moreover, quantum mechanical electron transfer theory is considered for neighboring silicon nanocrystals. The numerical calculation of the electronic matrix element allows to obtain the electron transfer rate as a function of the structural parameters. Furthermore, it is argued that the idealized I-V characteristics of such superlattices are well described by a space-charge limited current of an insulator in the presence of traps.

The theoretical predictions are then verified by I-V and C-V measurements on selected samples. An important role is attributed to Si/SiO_2 interface defects that act as carrier trapping sites at low electric fields, but also allow for defect-assisted tunneling between valence and conduction band at sufficiently high electric fields. The transport properties are investigated for a wide range of structural properties and the critical role of the tunneling barrier width and the Si excess is discussed. In addition, it is found that only about 1% of the phosphorus dopants seem to be optically and electronic active.

Zusammenfassung

Die vorliegende Arbeit beschäftigt sich mit der strukturellen und elektrischen Charakterisierung größenkontrollierter Silizium-Nanokristalle. Diese werden mittels Übergitterstrukturen aus alternierenden Schichten von siliziumreichen Siliziumoxynitriden und Siliziumdioxid und anschließender Hochtemperaturbehandlung hergestellt.

Zunächst wird eine Strukturanalyse mit Transmissionselektronenmikroskopie durchgeführt. Dadurch werden detaillierte Erkenntnisse hinsichtlich Größenverteilung, Form und dreidimensionaler Anordnung der Silizium-Nanokristalle gewonnen. Weiterhin werden Phosphor-dotierte Silizium-Nanokristalle hergestellt und auf ihren Phosphorgehalt und der Phosphorlokalisierung hin untersucht. Durch Verwendung von Röntgenabsorption und Atomsondentomographie wird nachgewiesen, dass sich Phosphor sowohl in den Nanokristallen als auch in der Si/SiO_2-Grenzflächenregion anreichert.

Der Ladungstransport in den Übergitterstrukturen wird anschließend anhand der quantenmechanischen Elektronentransfertheorie dargestellt. Die numerische Ermittlung der elektronischen Matrixelemente ermöglicht die Berechnung der Elektronentransferrate zwischen benachbarten Silizium-Nanokristallen in Abhängigkeit der strukturellen Parameter. Weiterhin wird die ideale I-V Kennlinie der Übergitter berechnet, die im undotierten Fall im Wesentlichen dem raumladungsbegrenzten Strom eines defektreichen Isolators entspricht.

Diese Vorbetrachtungen lassen sich daraufhin mit I-V und C-V Messungen durch systematische Probenvariation bestätigen. Eine besondere Rolle kommt hierbei den Si/SiO_2-Grenzflächendefekten zu. Bei niedriger elektrischer Feldstärke fungieren sie als Ladungsträgerfallen, wohingegen sie bei hinreichender elektrischer Feldstärke defektassistierte Tunnelprozesse zwischen Valenz- und Leitungsband erlauben. Der Einfluss der Tunnelbarrierendicke und des Siliziumüberschusses auf die Transporteigenschaften wird daraufhin untersucht und diskutiert. Im Falle von Phosphor-dotierten Schichten ergeben die Messungen, dass lediglich 1% der eingebauten Phosphoratome optisch und elektronisch aktiv sind.

1 Introduction

The idea of the integrated circuit can be traced back to the late fourties and it took more than 10 years until the first operational integrated circuit was manufactured in 1960 by Fairchild Semiconductor. It was made possible by solving the three main issues of microelectronics namely the integration of different electronic components in a single silicon (Si) crystal, their electrical isolation and interconnection. Since then, the number of transistors per chip is increasing exponentially following closely the predictions of Moore's law and culminating in the digital revolution. Nowadays, everyone benefits from the advances in silicon technology.

The transistor dimensions have now been scaled down to the nanometer range such that quantum physics start to influence the device characteristics. More importantly, the metal interconnects are becoming too resistive and are already a major issue to meet the requirements of the technology roadmap. Therefore, it is desirable to replace part of the metal interconnects by optical ones, ideally fully integrated on a silicon based chip.

Unfortunately, Si is an indirect semiconductor resulting in a very long radiative lifetime. As a consequence, non-radiative recombination at material imperfections dominates the recombination rendering light emission extremely inefficient. A reduction of the Si volume decreases the bulk recombination losses, but at the same time increases surface losses. However, when a silicon nanocrystal (Si NC) is made sufficiently small, the probability to obtain a defect free surface increases drastically allowing for a technologically relevant radiative efficiency.

Furthermore, quantum confinement pushes the Si bandgap from the infrared towards the visible region for very small Si NCs. This has been observed for porous Si by absorption [1] and by room-temperature visible luminescence [2]. Consequently, light emitting devices based on Si NCs have been realized [3–5]. Although the emission band of these devices is tuned by changing the Si NC size, they cannot yet outperform the best bulk Si light emitting diodes with a power conversion efficiency of 1% [6]. In addition, the observation of optical gain in ensembles of Si NCs [7, 8]

might allow for an electrically pumped, wavelength-tunable laser, whereas bulk Si may only work as an optically light amplifier [9, 10]. It must be noted however that gain in Si NCs is still a matter of intense scientific debate [11] and no lasing has been achieved so far.

Another particularly appealing application is the integration of Si NCs in novel solar cell concepts [12]. On the one hand the bandgap can be tuned to suit a Si-only based tandem cell concept. On the other hand, the enhancement of the carrier multiplication efficiency [13] might allow for efficient harvesting of high energy photons.

Last but not least, it is noted that further applications of Si NCs were considered. Embedded in a dielectric, Si NCs may be used as a conventional charge storage memory [14] or as an optical memory [15]. Furthermore, Si NCs can be used as a photosensitizer for oxygen molecules by acting as a spin-flip activator [16]. In addition, it was found that nanocrystalline Si is bioactive and biodegradable [17] which allows to use it as luminescence markers for in vivo applications [18].

In order to exploit the exciting potential of Si NCs, a detailed basic understanding in terms of both optical and electrical properties is mandatory. Therefore this thesis investigates the transport properties of ensembles of Si NCs using a model system of size-controlled Si NCs fabricated by the superlattice approach [19].

1.1 Charge Transport in Silicon Nanocrystal Ensembles

The conductivity of Si NC ensembles embedded in silicon dioxide (SiO_2) is strongly dependent on the degree of connectivity between the Si NCs [20, 21]. Hence the system is often described in terms of a percolation model that leads to a conductivity jump once the percolation threshold is reached. In fact, the term conductivity is a macroscopically defined property of a semiconductor that is proportional to the product of the free charge carrier density available for transport and the mobility of these carriers. The nature of a percolation model suggests that these parameters are non-uniform across the sample volume. It is therefore desirable to engineer the Si NC ensembles in a way that maximizes the percolation path density.

The electronic structure is then close to the one depicted in Fig. 1.1(a). In this one-dimensional view, the electron wavefunction is confined and localized to the

individual Si NCs and the adjacent Si NCs are connected by equidistant barriers. In this idealized system, the connectivity and hence the carrier mobility is largely dependent on the quantum mechanical transparency of the barrier. By increasing the barrier transmission, the system developes into a macroscopic, nanostructured semiconductor. The electron wavefunctions essentially delocalize leading to the formation of minibands (see Fig. 1.1(b)) [22]. The transport mechanism then changes from sequential carrier tunneling to band-like transport [23, 24].

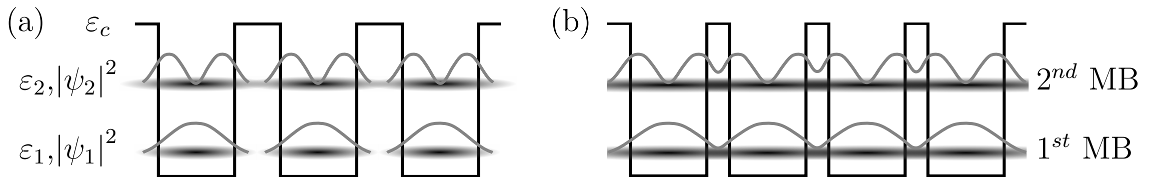

Figure 1.1: (a) Illustration of a 1D periodic array of semiconductor nanostructures in a high bandgap material showing highly localized wavefunctions $\psi_{1,2}$ at the two confined energy states $\varepsilon_{1,2}$. ε_c denotes the conduction band. (b) The same as for (a), but with a carrier transparent barrier that leads to the formation of minibands due to the large wavefunction overlap.

The second requirement for transport is the availability of free carriers. However, the Si NCs are usually extremely pure and the intrinsic carrier density is neglible. That means that carriers either have to be injected from the device contacts or created by optical generation. Another possibility is to introduce majority carriers by doping. Since this work investigates the transport properties in dark, intrinsic Si NC films are studied with the prerequisite of carrier injection. In addition, the feasibility of Si NC phosphorus (P) doping and its effect on transport is investigated.

1.2 Demand of Silicon Nanocrystal Doping

The ubiquitous Moore's law predicts that the transistor integration density approximately doubles within a constant timescale. Hence, the semiconductor industry is driven to continuously decreasing feature sizes and complex 3D transistor morphologies are natural consequences [25–30]. As the transistors shrink in dimensionality, the ultrasmall device performance becomes prone to enormous statistical fluctuations as the doping level depends merely on individual dopant atoms. In addition, surface effects begin to have a profound impact on the device

level in the sense that majority carriers may be trapped at surface defects and hence are not available for transport. The close vicinity of dopant atoms towards the dielectric interface induces an increase of the donor ionization energy largely before quantum size effects set in [31–34]. Moreover, ohmic contacts with low series resistances need to be realized with small contact areas and hence degenerately doped nanoscale contact regions are mandatory.

A very promising application of Si NCs is the realization of third-generation tandem solar cells that are entirely made of Si-based materials. Here, it is anticipated to make use of the bandgap tunability of Si NCs by precise size control and stack a Si NC-based solar cell on top of a regular crystalline Si solar cell [35, 36]. In this way, a larger part of the solar spectrum can, in principle, be harvested while thermalization losses are reduced and the overall solar cell efficiency may be increased. In this straightforward realization scheme, the two cells are stacked directly on top of each other, i.e. they operate in a series configuration. In order to maximize the efficiency, a tunnel junction is needed to connect the two cells and therefore degenerate doping of part of the Si NC layer is possibly needed. In addition, efficient exciton separation is usually accomplished by a built-in electric field and carrier selective contacts that are conventionally realized by a pn-junction within the absorber material.

1.3 Challenges of Doping Silicon Nanocrystals

The doping of nanostructures faces two fundamental challenges - self-purification [37–39] and the increase of the dopant ionization energy [32–34, 40–42]. In fact, doping means that an impurity atom that is usually different from the host lattice, is substitutionally incorporated into the crystalline nanostructure. This will inevitably lead to local stress and strain and eventually expell the impurity atom towards the nanostructure surface. The self-purification effect [37, 39] becomes stronger as the nanocrystal diameter decreases, because of the large impurity formation energy [43]. This has been shown experimentally for gas-phase synthesized Si NCs leading to a very low doping efficiency for Si NCs with diameters below 5 nm [44] as schematically shown in Fig. 1.2(a). During the synthesis, the dopants are expelled towards the surface and are trapped within a thin amorphous silicon dioxide shell that inactivates the dopant. It was shown that etching off the shell in hydrofluoric acid (HF) efficiently removed the dopants [44].

In contrast, the situation is less clear-cut in solid-state heterosystems such as the here investigated Si NCs within an embedding SiO_2 medium (Fig. 1.2(b)). In that case, dopants are present in the system, but they may reside within the Si NC, in the matrix surrounding the Si NC or at the interface between the two phases. As a consequence, the number of potential substituitional dopants within the Si NCs is greatly reduced.

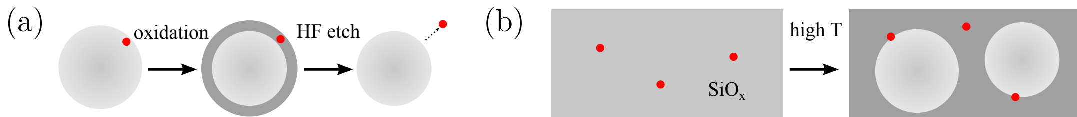

Figure 1.2: Self-purification in Si NCs: (a) a gas-phase synthesized doped Si NC, see text for explanation and (b) Schematic of solid state preparation of Si NCs from phase separation of silicon rich oxide, the dopants are expelled from the Si NCs, segregate at the interface and penetrate into the silicon dioxide matrix

Assuming now that the Si NCs can be substitutionally doped, the question arises how quantum confinement and the local dielectric environment affect the electronic structure of such a doped Si NC. In the bulk Si case, strong dielectric screening of the donor/acceptor ion leads to a narrow coulomb potential. Consequently the donor/acceptor energy level appears close to the bulk band edges and can be easily ionized at room temperature and small electric fields [45, 46].

As mentioned before, at the nanoscale, the screening may be less effective due to the low dielectric constant material surrounding the nanocrystal effectively localizing the electron at the donor ion (see Fig. 1.3). In addition, the intrinsic nanocrystal electronic states are shifted to higher energy due to quantum confinement imposed by the dielectric potential barrier. Thereby, the effective ionization energy of the doped nanocrystals is increased further, making room temperature dopant ionization highly unlikely.

In fact, it is a challenge to prove that the impurity atoms have really substituted a host atom within the nanocrystal in order to understand their properties [38, 47, 48]. In particular, for Si NCs embedded in SiO_2, the most commonly used techniques for quantification of electronically active carrier densities and mobility such as four point probe and Hall measurements are not applicable.

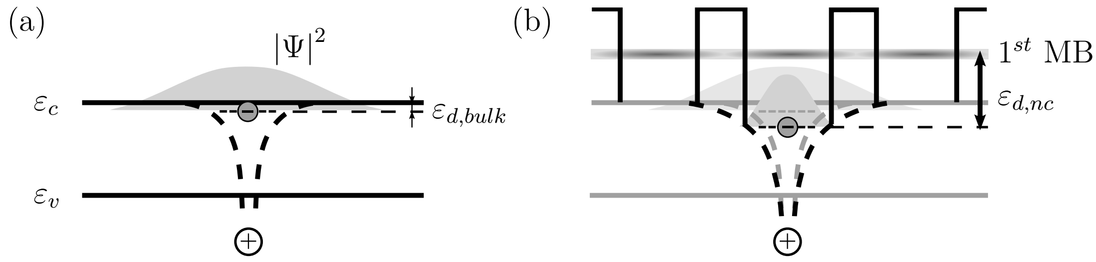

Figure 1.3: (a) Schematic representation of a donor in a bulk Si crystal, the donor electron is loosely bound to the donor ion leading to a well delocalized electron wave function $|\psi|^2$ and a shallow energy level; (b) Schematic representation of a doped Si NC/SiO_2 system. The donor wavefunction is influenced by the dielectric environment. The ionization energy is then the difference between the first miniband and the donor electron bound state energy.

1.4 Aims and Outline

This thesis studies three main aspects: the network morphology, P doping and the charge transport properties of Si NC-SiO_2 superlattices (SLs). In the second chapter, the relevant sample processing details as well as the characterization methods are described. The third chapter begins with a summary on the structural and optical properties of intrinsic Si NCs and is followed by a detailed investigation of the three-dimensional Si NC network revealing in particular the areal microstructure of size controlled Si NC ensembles. Another section is then devoted to the P doping of such Si NC ensembles and their structural properties focussing on the localization of P in the nanoscale composite material. The fourth chapter deals with charge transport in those ensembles. First, the quantum mechanical microscopic process of single carrier charge transfer is presented followed by the description of a macroscopic approach that appears sufficient to decribe the measurable macroscopic quantities in terms of current density and charge trapping. Moreover, electrical measurements are presented and discussed. The chapter finishes with a summary of transport regimes and mechanisms that have been revealed within this work. Finally, the results of this thesis are summarized and suggestions for future possible work are given.

2 Experimental Details

2.1 Sample Fabrication

2.1.1 Method of Silicon Nanocrystal Preparation

The Si NCs are prepared by the SL approach [49]. Silicon rich amorphous oxides are sandwiched between Si diffusion barriers (here SiO_2). Then, a high temperature treatment induces phase separation of the silicon rich oxide and crystallization of the resulting Si clusters. In the ideal picture, the size of the Si NCs is tuned by the silicon rich oxide layer thickness, whereas the areal density of Si NCs is adjusted by the amount of Si excess within the silicon rich layer as schematically shown in Fig. 2.1.

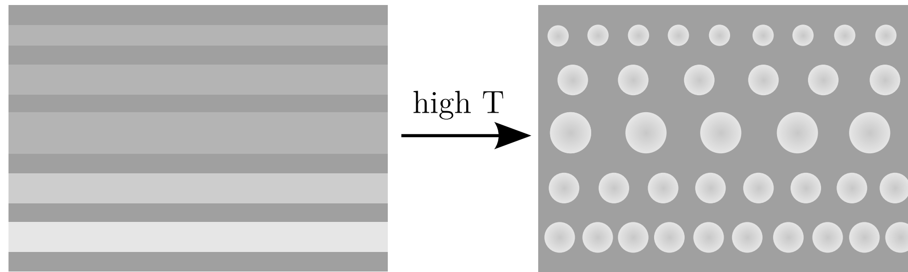

Figure 2.1: Schematic of the SL approach. The dark regions correspond to SiO_2, whereas the lighter regions correspond to increasingly more Si excess (left).

An Oxford Instruments Plasmalab 100 with a 13.56 MHz driven parallel plate reactor was used to deposit the ultrathin layers by plasma-enhanced chemical vapor deposition (PECVD) [50]. A N_2O/SiH_4 based precursor chemistry allows to achieve various silicon oxide compositions as a function of their gas flow ratio γ. Please note that significant amounts of nitrogen are incorporated in the silicon rich films, hence these layers are referred to as silicon-rich oxynitride (SRON) hereafter. The

precursor gases were diluted by a high flow of Ar in order to increase the film homogeneity and decrease the growth rate. The films were grown at a temperature of 375 °C, a chamber pressure of 600 mTorr and a plasma power of 13 W. In this way growth rates in the order of 2 Å/s were realized. Between subsequent layer depositions, the chamber was pumped to base pressure. Phosphorus doping was achieved by replacing part of the Ar carrier gas by a mixture of 1% PH_3 in Ar of up to 10 sccm.

2.1.2 Substrate Choice

All samples were deposited on (100)-silicon wafers or smaller pieces thereof. Lowly doped n-type 100 mm (100)-silicon wafers (phosphorus doped, conductivity 5–20 Ωcm) were used for capacitance-voltage (C-V), current-voltage (I-V), photoluminescence (PL) characterization as well as the structural analyses. The electrical characterization is simplified when n-type substrates are used, because at forward bias only electrons can be injected from the substrate whereas no carriers are injected from the front metal contact. This is in contrast to light emitting devices (LEDs) based on Si NCs that require bipolar carrier injection. Samples used for phosphorus quantification and localization were deposited on lowly doped p-type material (boron doped, conductivity 5–20 Ωcm) to avoid any ambiguity during the characterization. Within a sample series wafers of the same batch were used.

2.1.3 Process Flow

First, all samples were cleaned in Caro's acid for 10 min followed by a 15 s etch in diluted HF to remove the chemically formed SiO_2. Immediately after the HF dip, the samples were loaded into the PECVD chamber. A substrate heating step was followed by a 1 min Ar plasma cleaning step. Then the intended layer stack was grown, mostly consisting of alternating layers of SiO_2 and SRON. The samples were usually capped with a 10 nm SiO_2 layer that serves as annealing protection. Subsequently, all samples were annealed at 1150 °C in purified N_2 atmosphere to induce precipitation and crystallization of the Si NCs followed by a hydrogen passivation in a pure molecular hydrogen atmosphere for 1 h at 500 °C. Deviations from the above described treatment are henceforth indicated.

For electrical characterization, aluminum was evaporated and patterned by conventional lift-off technology. For some samples a transparent conducting indium

tin oxide (ITO) front contact was sputtered and patterned at Fraunhofer ISE. In order to achieve a good front contact, the SiO_2 capping layer was etched in highly diluted buffered HF prior to the top contact deposition. The etch rate was always determined from a reference SiO_2 piece. After patterning, the wafer front side was protected by a standard photoresist followed by backside metallization using aluminum sputtering.

2.2 Characterization Methods

In this section, the characterization methods used within this thesis are presented. While the electrical and optical properties were characterized at IMTEK, cooperations were sought for transmission electron microscopy (TEM) and elemental analysis techniques.

2.2.1 Electrical Characterization

All electrical characterizations were carried out using an Agilent B1500A device analyzer equipped with a multifrequency and a high resolution measurement unit. A positive voltage (forward bias) is defined to be applied to the aluminum gate of the device structure.

The static I-V measurements have been performed in a slow sweep regime if not stated otherwise. It is reasonable to use a constant change of electric field with time, i.e., $\mathrm{d}\mathcal{E}/\mathrm{d}t = \mathrm{const}$ to ensure identical measurement conditions for different sample thicknesses. A sweep rate of around 860 $\mathrm{kVm^{-1}s^{-1}}$ turned out to be sufficient to minimize transient effects due to charging and dielectric relaxation [51–54], if not otherwise indicated. The current density J is obtained by normalizing the measured current to the nominal device area defined by the size of the aluminum top contact. The electric field is calculated by dividing the applied gate voltage by the nominal thickness of the layer stack.

The dynamic measurements are realized by measuring the complex impedance at a fixed frequency within a predefined range of bias voltages. The samples incorporating Si NCs in SiO_2 on Si substrate and contacted by aluminum can be understood as a leaky metal-oxide-semiconductor structure. A common way of representation is therefore to express the impedance in terms of a parallel capacitance and conductance. The capacitive part stems from a series connection

of the semiconductor capacitance and the oxide capacitance. In accumulation, i.e. forward bias for n-type substrates, the parallel capacitance is equal to the oxide capacitance provided that the series resistance of the structure is low, because the semiconductor accumulation capacitance of the substrate becomes infinite. A typical high frequency C-V measurement is shown in Fig. 2.2. The C-V curve in Fig. 2.2(a) shows two saturating regions (accumulation and inversion) and a transition depletion region. The G-V curve is dominated by a single peak in the depletion region which is due to capture and release of interface trap states. From the dynamic measurements many oxide and semiconductor parameters can be extracted [55]. However, most relevant to the present thesis is only the bias dependence of the trapped charges that manifests itself in a flatband voltage shift ΔV_{FB}, i.e. a bias voltage shift of the whole C-V curve.

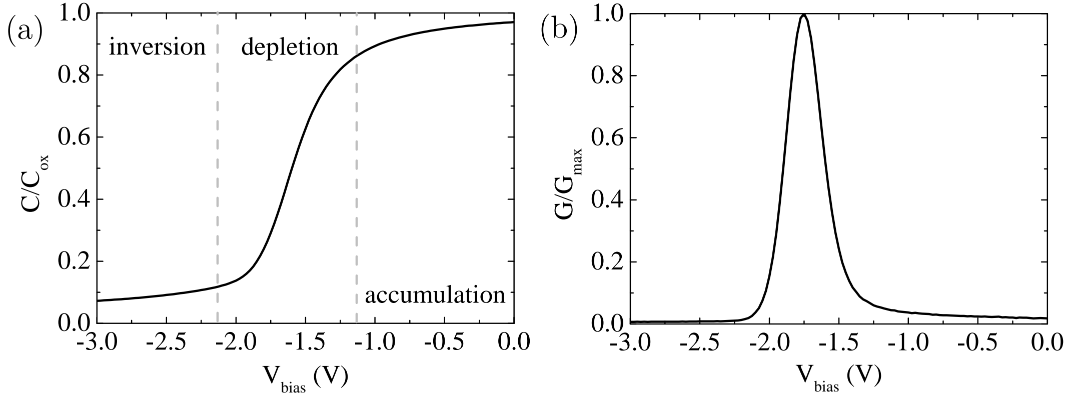

Figure 2.2: High frequency C-V measurement of an annealed and passivated PECVD-SiO_2 reference layer: (a) C-V graph, (b) G-V after correction of the series resistance

The carrier trapping effects were studied in a single pulse C-V mode. First a voltage was applied to the gate and hold for 5 s, if not stated otherwise, immediately followed by a fast C-V sweep in a narrow voltage range around the previously determined flatband voltage. In this way, the C-V curve can be taken in less than 1 s so that slower detrapping and mobile charge effects can be measured by means of ΔV_{FB}. In order to correct for the effect of the dielectric stack thickness and to make ΔV_{FB} comparable between different samples, the effective net mobile charge per unit area has been calculated by the well-known expression $Q_{eff} = -C_{ox}\Delta V_{FB}/q$ [46, 55]. Here, $q = 1.602 \times 10^{-19}$ As is the elementary electric charge and C_{ox} is the oxide capacitance per unit area of the device in accumulation that has been corrected for

the effect of series resistance. All C-V measurements were carried out at a frequency of 300 kHz.

Please note that the measurements were performed in dark with the Si substrate in accumulation, although the measurements do not change, when performed under illuminated conditions.

2.2.2 Photoluminescence Spectroscopy

PL is a non-destructive and valuable tool to characterize optical transitions in semiconductor nanocrystals. Under excitation with photons of energy in excess of the material's bandgap, excitons are created, thermalize to the conduction and the valence bandedge respectively and recombine at least partly radiatively. The emission spectrum thus reflects the bandgap energy distribution of the nanocrystal ensemble. Therefore, PL is ideally suited as a process monitor for Si NC fabrication, but can also be used to study the influence of sample variations.

The PL was measured at room temperature with a liquid N_2 - cooled Si CCD camera attached to a single grating monochromator using a HeCd laser (325 nm line) as excitation source. An excitation power density well below the saturation threshold at room-temperature was used throughout this thesis [56, 57]. The PL spectra were corrected for the spectral response of the system.

2.2.3 Transmission Electron Microscopy

Due to the small size of Si NCs, TEM is an extremely valuable tool to provide detailed nanostructural insight into the material's morphology. For TEM the sample under study has to be prepared as thin as possible to be electron transparent and minimize multiple inelastic scattering events of the electrons while transversing the sample. Two methods are commonly applied for sample preparation, namely the focussed ion beam (FIB) lift-out technique and the ion milling technique. In the former, a dual beam electron microscope equipped with an ion beam is used to literally cut out a very thin slice of the sample and attach it on a TEM grid. In the latter technique, the sample is cut and glued face-to-face followed by mechanical thinning down to a few tens of microns. Then, the sample is milled to electron transparency by ion beam milling under grazing incidence. Optical monitoring is used to determine the endpoint. In this way, very thin regions are

often created that can be imaged in a TEM. The above preparation methods give rise to thin film cross sections. In the simpliest way, this allows to measure the film thicknesses of individual sublayers in a multilayer with atomic precision in case of single crystalline epitaxial layers.

In a TEM, a high energy electron beam is focussed on the sample by electromagnetic lenses. After passing the specimen, the electrons are filtered according to their scattering angle or energy and projected on a camera to yield a two dimensional micrograph of the imaging area. Hence, different contrast mechanisms can be harnessed that are explained in extensive details in standard textbooks [58]. A common approach to visualize Si NC/SiO_2 multilayers is to use defocussed brigthfield imaging [49, 59, 60]. Provided a highly coherent electron beam is used and the sample is extremely thin, the defocus condition gives a strong contrast at the Si/silicon dioxide interface due to the phase contrast of electron waves travelling through different regions of the material. In this way, individual Si NCs as well as Si NC/SiO_2 multilayers can be imaged in the TEM.

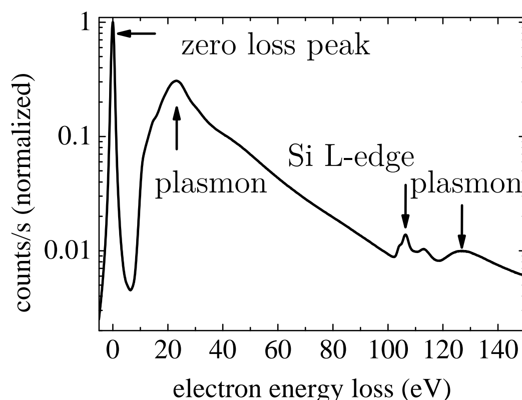

Figure 2.3: Experimental EELS-spectrum of a 20 nm SiO_2 film showing that plasmon losses dominate the spectrum making them suitable for mapping purposes.

Another popular technique is energy-filtered TEM (EF-TEM). Here, the collected electron intensity is mapped out at a certain energy window. A partial electron energy loss spectroscopy (EELS) spectrum is presented in Fig. 2.3. The strong zero loss line is followed by valence band and plasmon losses. The main Si plasmon loss peak is a relatively sharp peak at around 17 eV, whereas the SiO_2 plasmon loss peak is broader and centered at around 23 eV. Hence, the Si plasmon peak is commonly

exploited to map Si nanostructures in a dielectric matrix as it usually provides the best available contrast. However, it has to be noted that this imaging mode does not distinguish between amorphous and crystalline nanoparticles. Further loss features in the EELS spectrum are the element specific core absorption edges lines that can be used to determine the site specific nanoscale material composition. It has to be noted that the absorption decreases rather exponentially with energy such that high order core level transitions suffer from a bad signal-to-noise ratio. Thus the elemental quantification is usually limited to within a few absolute percent and the lower detection limit depends strongly on the material under study.

Another possibility is to collect the emitted X-ray photons that follow the core absorption event (energy dispersive x-ray spectroscopy (EDX)). The lower background signal associated with the EDX analysis may in fact simplify elemental analysis, but has the disadvantage that only few x-ray photons can be collected by the detector due to geometrical restrictions within the electron column. In addition, the TEM is operated in a scanning mode, when lateral resolution is required. In combination with the low detection efficiency of the X-ray photons, a mapping is extremely inefficient and prone to sample drift that essentially limits the lateral resolution.

The following transmission electron microscopes have been used in the course of this thesis:

- JEOL J2010F, 200 kV, Gatan Image Filter (University of Barcelona, Spain), data presented in Fig. 3.2 and Fig. 3.9
- JEOL JEM 4010, 400 kV (Max-Planck Institute of Microstructure Physics Halle, Germany), data presented in Fig. 3.11
- aberration corrected FEI Titan 80-300, 300 kV & 80 kV, Gatan Image Filter (Karlsruhe Institute of Technology, Germany), data presented in sec. 3.2

2.2.4 X-Ray Photoelectron Spectroscopy

X-ray photoelectron spectroscopy (XPS) is a non-destructive technique that allows to obtain chemical information of the sample surface. The basic idea is to use high energetic X-rays to irradiate a specimen and thus triggering photoelectron emission. The electron kinetic energy is given by the difference of photon energy and electron binding energy. An XPS spectrum is obtained, when the electrons are

recorded as function of their kinetic energy. This spectrum constitutes a chemical fingerprint of the sample surface, because the core level electron binding energies depend on the element itself and its neighboring atoms. The quantitative analysis is usually carried out by weighting the element specific peak intensity of the loss-free core-electron peaks. The information depth is thus limited to only a few nanometers below the sample surface because of the low inelastic mean free path of electrons. The quantification is error-prone because the sensitivity factors depend on a calibration of reference samples, but any compositional change in the sample inherently changes the inelastic mean free path of electrons. The sensitivity of XPS is in the range of 1 at% due to the large noise background from inelastically scattered electrons. Peak overlapping may further complicate the analysis.

XPS was used to quantify the stoichiometry of the SRON layers and verify the presence of P dopants in the films. In addition, a detailed analysis of the P 2p peak was carried out in order to analyze the chemical surrounding of the incorporated P atoms. The following XPS tools were used:

- Physical Electronics Phi Quantum 2000, mono Al-K_α excitation, SGS Institute Fresenius GmbH Dresden (Germany), data presented in Fig. 3.1
- Kratos AXIS Nova, mono Al-K_α excitation, IFOS GmbH Kaiserslautern (Germany), data presented in Fig. 3.1 and Fig. 3.12
- Thermo Scientific K-alpha, mono Al-K_α excitation, Karlsruhe Institute of Technology (Germany), data presented in Fig. 3.14

2.2.5 X-Ray Absorption Spectroscopy

In X-ray absorption spectroscopy (XAS), the element-specific electron core level absorption is probed as a function of X-ray excitation energy. The absorption edge and fine structure serves as a fingerprint of the local chemical surrounding of the absorbing atom and hence contains detailed structural information such as neighboring atoms, bond distances and angles in principle [61]. This wealth of information comes at the cost for the need of a tunable monochromatic X-ray source that is only available at synchrotron light sources.

The P K-edge absorption (at 2140 eV) was measured at the SUL-X beamline at ANKA (Angströmquelle Karlsruhe at Karlsruhe Institute of Technology/Germany). Monochromatic X-rays were obtained by using a Si(111) double crystal

monochromator with an energy resolution of about 0.2 eV at 2150 eV and with fixed exit. Due to the large X-ray absorption length in the range of micrometers, the excitation was carried out using a shallow angle to maximize the excitation volume. The absorption was measured by monitoring the P-Kα fluorescence emission using a seven element Si(Li) fluorescence detector (SGX Sensortech, former e2v, former Gresham, UK). The signal is normalized to the incident photon flux that is measured simultaneously by a custom made ionization chamber (ADC, US) filled with about 50 mbar N_2 gas. The energy has been calibrated to 2152 eV at the white line maximum of the P K X-ray absorption near-edge structure (XANES) spectrum of $NaH_2PO_4 \bullet 2H_2O$. The energy step size across the XANES region was 0.2 eV.

2.2.6 Molecular Cs^+ Secondary Ion Mass Spectrometry

The quantification of low amounts of P in SRON layers is a challenging task. This was tackled by using molecular Cs^+ secondary ion mass spectrometry (MCs^+) [62, 63] to determine the P content within the films. In MCs^+ the detection and elemental sensitivity of secondary ion mass spectroscopy in the range of a few ppm is coupled with the reduced Cs^+ ion yield susceptibility to sample composition. When Cs^+ ions are used to sputter a sample, stable MCs^+ species form, where M denotes an element of interest. These ions can then be detected according to their mass to charge ratio.

The MCs^+ measurements were carried out at IFOS (Kaiserslautern/Germany) with a Cameca IMS-4f ion microscope using 5.5 keV Cs^+ for sputtering. The sensitivity factors were determined from a reference measurement on P doped amorphous Si of known composition. In order to account for the different silicon excess variations in the SRON layers, oxygen was implanted into the amorphous Si layer and a second order sensitivity factor correction was applied to capture possible ion yield changes induced by the SRON stoichiometry [63].

2.2.7 Elastic Recoil Detection Analysis

Elemental quantification based on XPS or MCs^+ are prone to systemic errors due to the use of sensitivity factors that are sample specific and therefore need precise calibration. Hence, ion beam based material analyses can be used, since they are standard-free and absolute elemental quantification methods. When a high energy ion beam is directed onto a specimen, the ions can either be backscattered at higher

Z elements or kick out lower Z elements. The first mechanism is referred to as Rutherford backscattering spectrometry whereas the latter is called elastic recoil detection analysis (ERDA). In any case the sensitivity can be as low as a few ppm, but strongly depends on the details of the sample composition and measurement conditions. In case of ERDA, the recoiled ions are detected by a Bragg ionization chamber with energy and mass resolution.

The ERDA measurements were carried out at Helmholtz-Zentrum Dresden-Rossendorf (Germany) using 45 MeV Cl^{7+} ions impinging at an angle of 75°, whereas the recoiled ions were detected at a scattering angle of 31°.

2.2.8 Atom Probe Tomography

The atom probe tomography (APT) is a powerful technique to obtain a three-dimensional elemental map of a sample with high spatial resolution of down to 0.3 nm. At the same time up to 60% of all atoms within the probed nanoscale volume are detected [64]. In order to achieve this ultimate resolution, monolayers of atoms are ionized and emitted off a needle-shaped specimen with a tip radius below 100 nm and projected onto a position sensitive mass detector. Repetition of this process allows then for a three-dimensional data reconstruction of the specimen. The evaporation is achieved by biasing the specimen with a high voltage with respect to the local ion collecting electrode. In this way an intense electric field is created at the specimen surface which should be below the field evaporation threshold of the material under study. In order to evaporate single atomic layers, a short pulsed voltage is superimposed on the bias voltage to trigger the field evaporation. While this approach works well for metals, it cannot be applied to semiconductors or insulators. Therefore, the pulsed voltage is replaced by a UV laser pulse to supply sufficient energy for ion evaporation.

The APT has been carried out at IFOS GmbH (Kaiserslautern, Germany) using a LEAP 4000X HR instrument (Cameca) which is equipped with a reflectron-type time-of-flight mass spectrometer and a pulsed UV laser (λ=355 nm, pulse length 10 ps, pulse energy was 70 pJ, repetition rate 100 kHz). During the analyses (chamber pressure about 1×10^{-11} mbar), the specimens were cooled to a temperature of around 76 K. The mass resolution of the system was $m/\Delta m \approx 800$ and around 36% of all atoms are detected. The specimen tips have been prepared by the cut-and-lift-out technique using an ALTURA 875 dual-beam FIB instrument

(FEI). First the sample is covered with a thin chromium layer that serves as a protection layer against the subsequent ion beam treatment. A wedge-shaped part of the sample is cut out from the sample by FIB and attached to a Si microtip that is specially designed for the APT analysis. The final needle-like tip shape is then obtained by ion beam milling. Most of the data reconstruction and analysis was carried out with the instrument's software package IVAS3.6.4.

3 Material Properties of Silicon Nanocrystals

3.1 Basic Structrual and Optical Properties of Intrinsic Silicon Nanocrystals

The SL approach suggests that the Si NC diameter can be tuned by changing the thickness of the SRON layer, whereas the Si NC areal density is controlled by the SRON stoichiometry. Therefore, it is important to know the SRON film stoichiometry as a function of the process parameter γ, the gas flow ratio of N_2O and SiH_4.

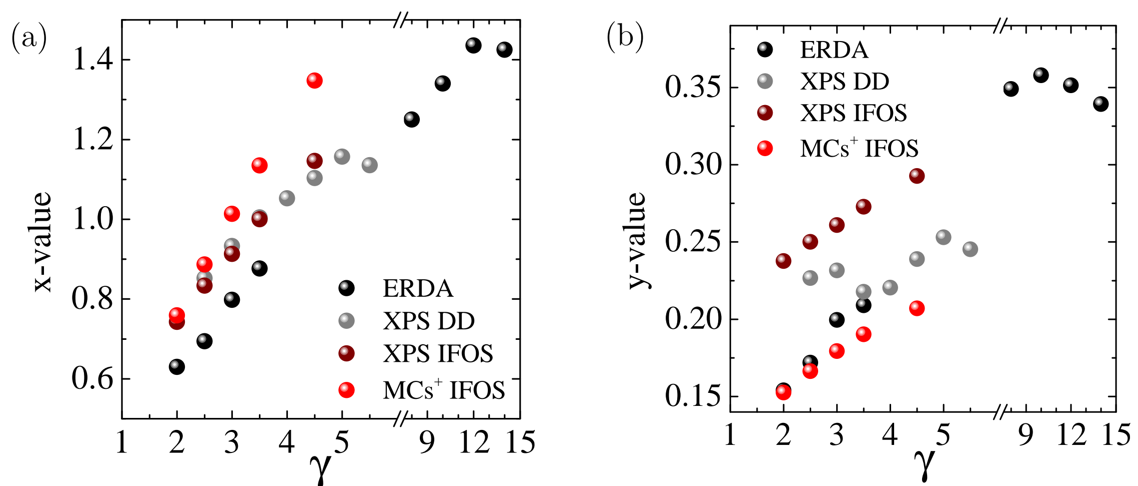

Figure 3.1: Summary of SRON stoichiometries measured by XPS, ERDA and MCs^+: x-value (a) and y-value (b) in SiO_xN_y as a function of the process gas flow ratio γ. The data from IFOS was extracted from the depth profile of P doped samples shown in Fig. 3.12. All measurements have been carried out on as deposited samples.

Fig. 3.1 shows the calculated x and y values in SiO_xN_y as determined from XPS, ERDA and MCs^+ measurements for as deposited bulk SRON layers. It can be seen that the Si excess can be tuned solely by controlling the gas flow ratio γ. However, an undesired side-effect is the non-neglible amount of nitrogen incorporation into the SRON layer of up to around 10 at%.

A significant quantification difference exists between the used characterization methods. A systematic error might be present in the XPS and MCs^+ due to changes induced on the sample surface by sputtering and due to uncertainty of the sensitivity factors. Therefore, the ERDA results are most trustworthy. However, in the following, the x-value of the XPS measurements on as deposited bulk films (XPS DD in Fig. 3.1) are used for consistency reasons with other works [50, 56, 57] and because of the larger accessible range of measurements in the interesting low x regime. Henceforth, the N content as described by the y-value is omitted for clarity. However, it must be kept in mind that the presence of nitrogen affects phase separation and diffusion during annealing and thus may lead to different structural, optical and electrical properties as compared to nitrogen-free material [65].

The hydrogen content was determined from ERDA to be about 10 at%, while similar amounts were detected by MCs^+. However, our studies showed that the high temperature annealing causes out-diffusion of hydrogen [50, 66] which is then below the detection limit of ERDA for hydrogen of about 0.1 at%.

A typical EF-TEM image of a SL is shown in Fig. 3.2(a) [50]. The Si NCs are well confined to the bands of initial SRON. In addition, the Si NC diameter was measured for varying SRON thickness as demonstrated in Fig. 3.2(b) and (c). Clearly, there is a correlation between the SRON thickness and the resulting Si NC diameter. However, at low thicknesses, the diameter becomes slightly larger when compared to the SRON thickness, whereas at larger SRON thicknesses, the diameter becomes smaller than the intial thickness.

In general, the initial phase separation of SRON is followed by particle growth via Ostwald ripening which is limited by the diffusion of Si in SRON [67]. At small SRON thickness the interparticle distance is also small and hence Ostwald ripening is pronounced. This effectively leads to clusters larger than the SRON thickness. The opposite effect is observed as the SRON thickness is increased. Since the interparticle distance increases, Ostwald ripening is also reduced due to longer diffusion paths. Consequently, the particles grow smaller as compared to the initial SRON thickness.

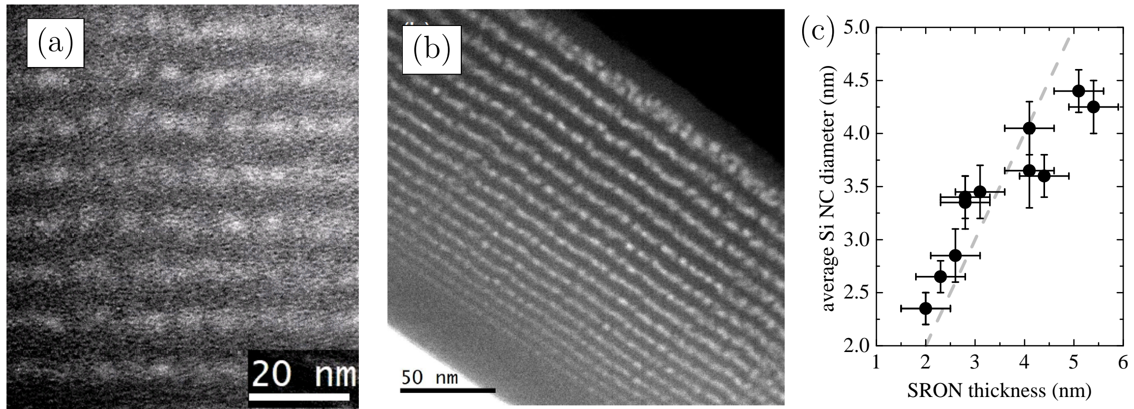

Figure 3.2: (a) EF-TEM of a annealed 4nm $SiO_{1.0}$/4nm SiO_2 SL showing the presence of Si nanoparticles; (b) EF-TEM of a SL sample, where the $SiO_{1.0}$ thickness is increased continuously; (c) Si NC diameter as a function of $SiO_{1.0}$ thickness that was measured separately on a as deposited sample, the dashed line denotes the case where the Si NC diameter is equal to the SRON thickness. The diameter error bars involve the complete range of diameters measured by EF-TEM.

The PL of Si NC ensembles with varying Si NC diameter is plotted in Fig. 3.3(a). There is a pronounced high energy shift, when the size is decreased that is due the bandgap increase caused by quantum confinement. In addition hydrogen passivation increases the PL intensity significantly for all size ranges (Fig. 3.3(b)). This is most likely associated with the passivation of Si surface dangling bonds [68, 69].

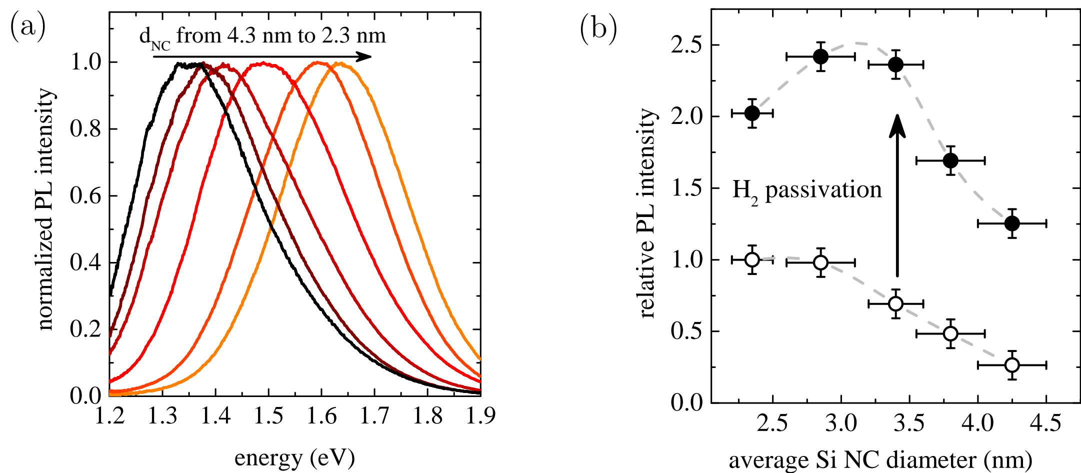

Figure 3.3: (a) normalized PL spectra of Si NCs SLs for different average diameters (20 bilayers, 4 nm SiO_2 barrier); (b) the enhancement of the PL intensity after hydrogen passivation - the dotted lines are guides for the eye.

So far, it has been implicitly assumed that the Si nanoclusters are crystalline. Hence it should be noted that the samples feature a high amount of crystalline Si as shown by Raman measurements [70]. In addition, Si crystal planes are observed by high-resolution TEM (HR-TEM) and X-ray diffraction (not shown).

3.2 In-plane Order of Silicon Nanocrystals

The conventional way of imaging Si NCs by TEM is carried out in a cross-sectional imaging mode. This usually nicely demonstrates the multilayer structure, however, the in-plane order of Si NCs is not revealed and only limited information can be obtained. Hence, it is desirable to image single layers in a plane-view configuration. This is most conveniently realized by depositing single layers of Si NCs directly on thin membranes that are available commercially.[1] In this way, the tedious TEM preparation can be avoided, there is plenty of equal imaging area and the imaging plane is extremely homogeneous which is beneficial for EF-TEM.

In preliminary experiments, it turned out that TEM-grids with a 5 nm silicon nitride membrane are best suited. The main advantage is its high temperature stability that is needed for the precipitation and crystallization of the Si NCs. In a first attempt, the single Si NC layer was sandwiched between two 10 nm thick SiO_2 layers in order to protect the SRON layer from parasitic oxidation. Silicon nanoparticles were imaged by EF-TEM, but it was realized that there exists a time-dependence and particles began to appear after long exposure to the electron beam. In addition, the available contrast between the Si nanoparticles and the matrix was weak due to overlap of the Si plasmon loss at 17 eV and the large SiO_2 plasmon background (broad peak at about 23 eV). Hence, the barrier and capping layer was reduced down to 2 nm.

In Fig. 3.4, EF-TEM images of a sample with 2 nm SiO_2 buffer and capping are presented. Silicon nanoparticles are clearly visible (Fig. 3.4(a)), but also heavy sample transformations occur upon electron irradiation that manifest themselves in the increase of particle size and creation of new particles (see Fig. 3.4(b) and (c)). The intense electron beam obviously causes the breaking of Si-O bonds accompanied by the creation of volatile O_2 molecules which is supported by the creation of defects in SiO_2 after electron irradiation [71] and a SiO_2 thickness dependence on the hole

[1]see www.temwindows.com for a detailed list of available TEM-grids

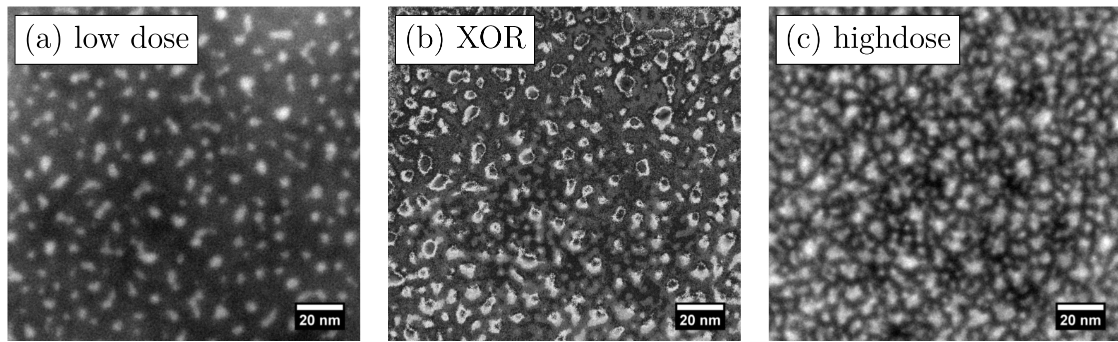

Figure 3.4: EF-TEM images at 300 kV of a sample with a 4.5 nm $SiO_{0.64}$ layer sandwiched between two 2 nm SiO_2 layers and annealed at 1150 °C for one hour in nitrogen atmosphere. (a) image in a fresh area, (c) after around 10 min exposure to the intense electron beam and (b) XOR image of (a) and (c) that highlights the apparent change (denoted by white regions). Clearly, the nanoparticles seem to grow and new particles begin to appear.

drilling time when exposed to an intense electron probe [72]. Another possible explanation would be preferential sputtering or knock-on of oxygen [73–75].

A common way to reduce the electron beam damage is to reduce the operating voltage of the TEM. Therefore, two reference samples were imaged by EF-TEM at 80 kV (see Fig. 3.5). Surprisingly, both samples were again subject to electron beam damage that resulted in the creation of dense ensembles of Si nanoparticles after about 1 min of irradiation (Fig. 3.5(b) and (c)). However, the damage is neglible, when a fresh sample area is imaged. Hence, care must be taken when Si NCs embedded in SiO_2 are investigated by TEM. Operation at 80 kV combined with a low imaging dose seems to be a suitable compromise and is therefore used in the following experiments.

Another issue that arises from closer inspection of Fig. 3.4(a) is the apparent low areal density of Si NCs for a stoichiometry of $SiO_{0.64}$ with a SRON thickness of 4.5 nm that represents a rather high Si excess concentration with an estimated precipitated Si volume excess of 40 %. Lower Si excess concentrations and smaller SRON thicknesses resulted in even lower areal densities. In addition the PL of the single Si NC layer was blueshifted as compared to a SL with the same SRON thickness. In some cases, even no PL was observed. All these results suggest that the single Si NC layer is subject to a loss of excess Si during the annealing process.

Oxidation of excess Si by some species in the annealing ambient is unlikely because of the highly purified inert gases used during the annealing process. However,

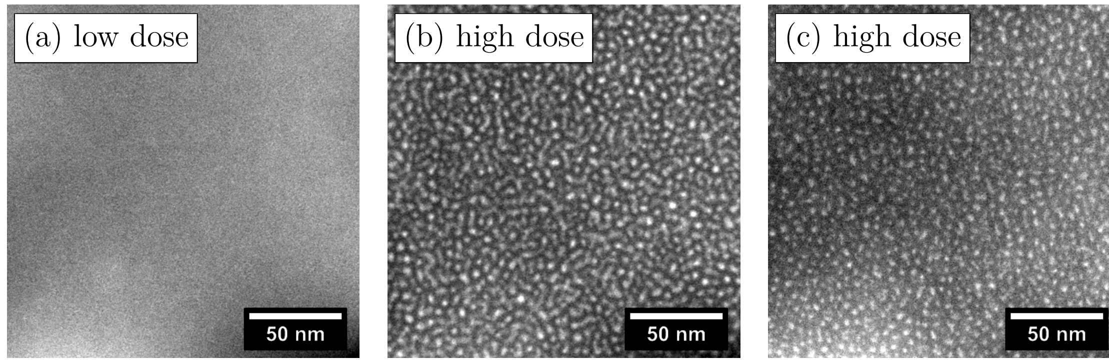

Figure 3.5: EF-TEM images at 80 kV of two reference samples: a virgin 20 nm SiO_2 TEM-grid (a,b) and 10 nm PECVD-SiO_2 on a 5 nm SiN-TEM-grid annealed at 1100 °C (c). At low dose, no Si particles can be observed (a), whereas a high dose leads to dense arrays of Si nanoparticles ((b) and (c))

out-diffusion of Si has to be considered. The diffusion of Si in SiO_2 is known to be mediated by co-diffusion of SiO molecules and hence strongly depends on the nature of Si/SiO_2 interface [76]. Using the values from literature, [76] the diffusion length of Si $2\sqrt{\mathcal{D}_{Si}t}$ within a standard 1 h annealing is determined to be around 2.6 nm which is larger than the 2 nm capping SiO_2 even though the heating and cooling ramps were not considered. Although, the Si loss rate is not exactly known, Si out-diffusion may well explain the observed effects.

The diffusion length can be reduced by shortening the annealing time and lowering the annealing temperature. Hence, a series of PL experiments was carried out on Si pieces in order to find the best annealing conditions to preserve a single Si NC layer while still maintaining a considerable PL emission. Applying faster temperature ramps with a short peak temperature at 1100 °C appeared to give the highest PL intensity and gave reasonable PL peak energies for small and large Si NCs. It was further found that annealings in Ar ambient gave higher PL intensities when compared to N_2 ambient which is in contrast to multilayers, where N_2 annealing is usually reducing interface defects and hence leads to superior quantum efficiencies [65, 69, 77].

Therefore, 10 nm $SiO_{0.93}$ films were annealed in Ar and N_2 atmosphere and compared by plane-view EF-TEM which is presented in Fig. 3.6. As can be seen at lower magnification (Fig. 3.6(a)), the Ar annealed sample exhibits a high density of surface defects. It appears that part of the layer has been removed (darker regions). These surface damages are absent for the N_2 annealed sample which is very homogeneous across the whole sample area. Similar effects have been reported for Ar annealed SiO_2

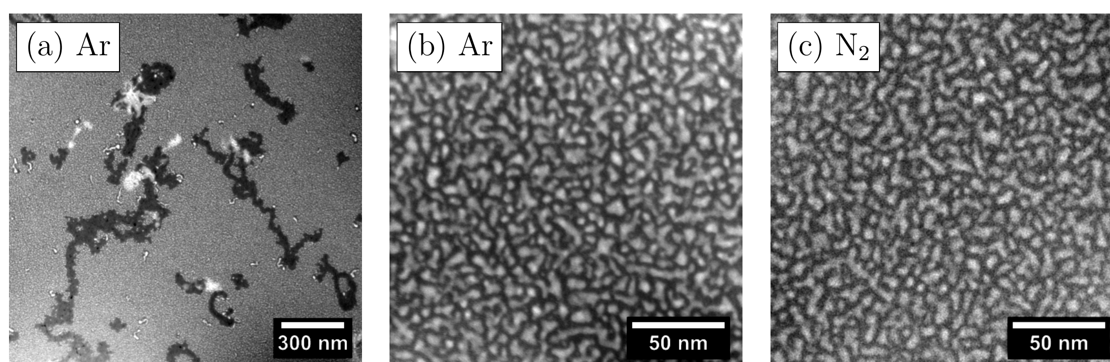

Figure 3.6: EF-TEM images at 80 kV of a sample with a 10 nm $SiO_{0.93}$ layer sandwiched between two 2 nm SiO_2 layers and annealed in Ar (a,b) and N_2 (c) using fast temperature ramps up to a peak temperature of 1100 °C. (a) low magnification image of the Ar annealed sample, (b) high magnification image of (a) in an undamaged area, (c) high magnification image of the N_2 annealed sample

thin films on Si and were ascribed to out-diffusion of SiO-molecules [78]. Therefore, it can be concluded that annealing in N_2 hampers the Si out-diffusion. However, the undamaged microstructures (cf. Fig. 3.6(b) and (c)) are very similar for both annealings.

From HR-TEM and electron diffraction, it was found that both samples feature a high degree of crystallinity, albeit the Si NC shape is not spherical at all. Due to the minimization of Gibb's free energy, a spherical shape is expected which is limited by the possibility of atomic rearrangement. Since the phase separation is completed within a few seconds due to diffusion of oxygen [79], the nanoparticle growth and shaping can only be achieved by diffusion of Si within SiO_2 which is extremely low at the here employed annealing procedure. Longer and higher temperature annealings would certainly lead to larger amounts of spherical particles with a reduced density [80, 81].

Once the annealing conditions and TEM routines have been specified, it is straightforward to investigate the influence of the SRON layer thickness and stoichiometry on the Si NC density, size and shape. In Fig. 3.7 a series of EF-TEM images is presented for three samples with SRON thicknesses of 10, 4.5 and 3.5 nm annealed up to a peak temperature of 1100 °C.

A transition from irregular and large towards spherical and smaller precipitates is clearly observed. Owing to the excellent contrast, the images can be evaluated by image processing software such as ImageJ in order to analyze the particle distribution. Based on the two dimensional projection of the particles, an effective

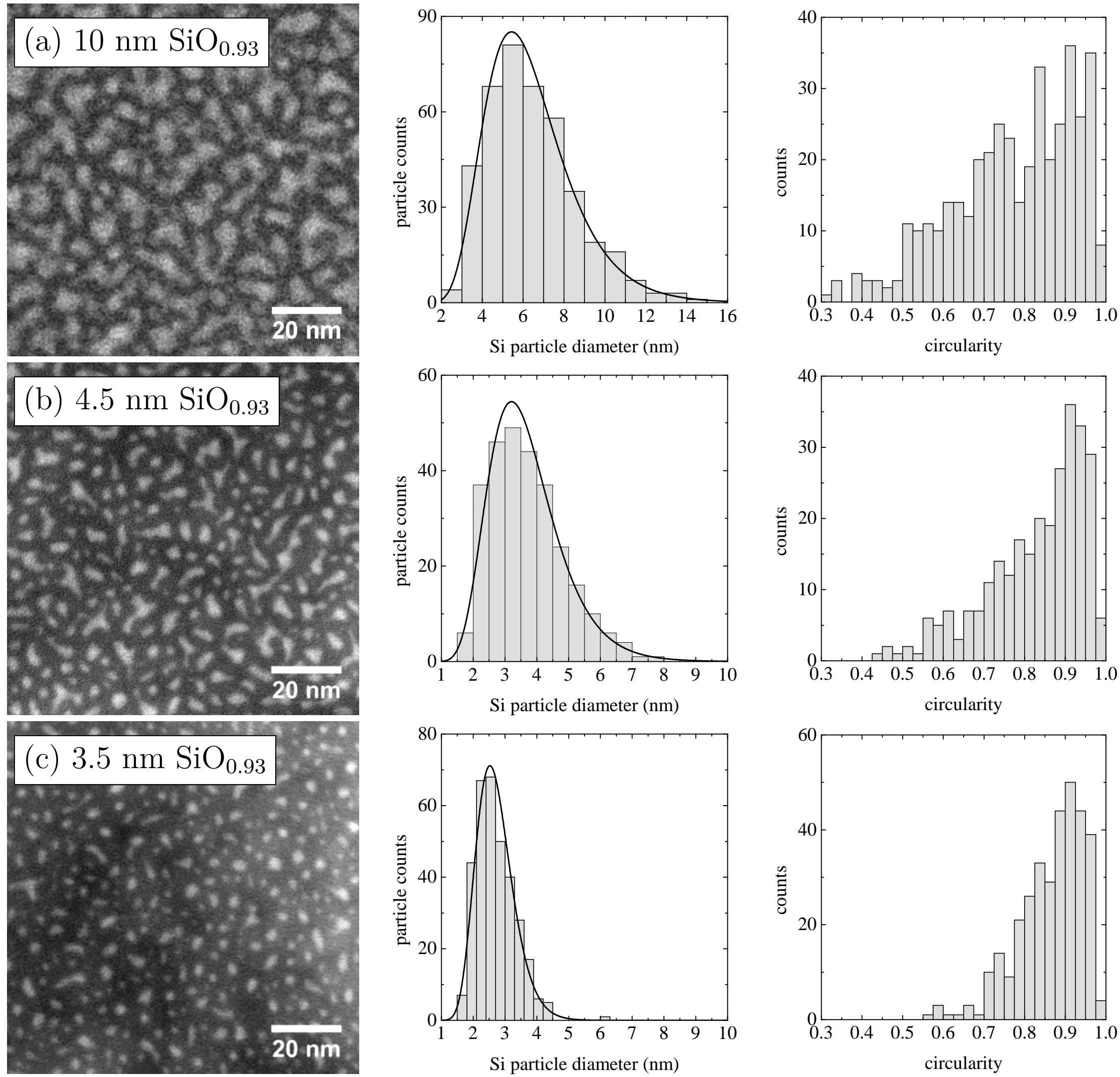

Figure 3.7: EF-TEM images for single $SiO_{0.93}$ layers with different thicknesses of 10 nm (a), 4.5 nm (b) and 3.5 nm (c). All samples have a 2 nm buffer and capping SiO_2. Next to the EF-TEM images, the particle diameter and circularity distributions are shown.

particle diameter has been calculated from the particle area A according to $\sqrt{4A/\pi}$. In addition the so called circularity is used to describe the particle shape and is defined as $4\pi A/p^2$, where p is the particle perimeter. A circularity value equal to 1 corresponds to a perfect circle, whereas smaller values indicate elongated or irregular shapes. The particle and circularity distributions in Fig. 3.7 unambiguously reflect the observations made in the EF-TEM images. The diameter distribution can be fitted excellently by a log-normal distribution for all samples studied.

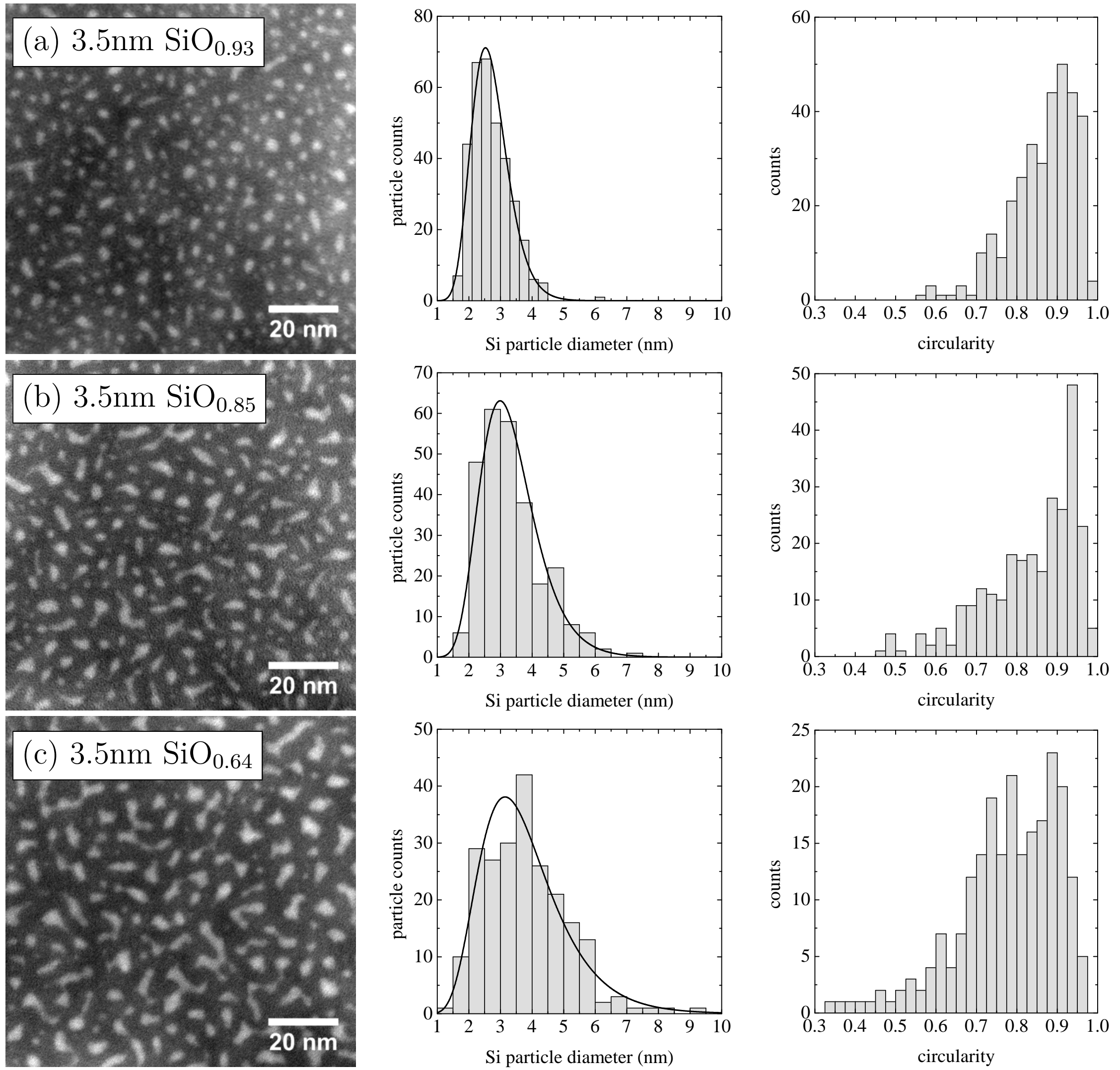

Figure 3.8: EF-TEM images for single 3.5 nm thin SRON layers with different stoichiometires of $SiO_{0.93}$ (a), $SiO_{0.85}$ (b) and $SiO_{0.64}$ (c). All samples have a 2 nm buffer and capping SiO_2. Next to the EF-TEM images, the particle diameter and circularity distributions are shown.

Furthermore, the influence of the SRON stoichiometry on Si nanoparticle formation is demonstrated in Fig. 3.8. Interestingly, increasing the Si excess exhibits a similar effect on the Si NC size and shape as the SRON thickness increase.

The transition from clustering to spinodal-like decomposition [82–84] is obviously a sensitive function of SRON thickness and stoichiometry. Due to the one dimensional geometrical confinement imposed by the SiO_2 barriers, the effective excess Si available for particle formation is reduced and hence spinodal growth sets in at higher SRON thicknesses [85]. As the Si excess in the SRON layer is increased, the

SRON thickness threshold for spinodal decomposition is shifted to smaller values [67, 85], a fact that is experimentally demonstrated in Fig. 3.7 and Fig. 3.8.

The EF-TEM studies are summarized in Tab. 3.1, where the maximum of the diameter distribution as well the particle areal density A_{NC} and the particle area fill fraction are given. The areal particle density is increased and the Si NC diameter is decreased, when the SRON layer thickness is reduced as expected. However, increasing the Si excess, reduces the areal density. This behavior is not quite intuitive, because the opposite effect would be expected from the ideal SL approach and has been indirectly measured from C-V measurements [86]. The reason is apparently that at such high Si excess concentration, larger Si regions form as is indicated by the increased average Si NC diameter. Finally, it must be noted that a certain amount of Si still appears to be lost by Si out-diffusion during the optimized annealing that effectively decreases the particle size.

Table 3.1: List of parameters extracted from the EF-TEM investigations. The Si NC diameter D_{nc} corresponds to the maximum of the log-normal distribution fit.

d_{SRON} (nm)	stoichiometry	D_{nc} (nm)	A_{nc} (NC/cm^2)	area fill fraction (%)
10	$SiO_{0.93}$	5.4	(1.13 ± 0.02)x10^{12}	40.8
4.5	$SiO_{0.93}$	3.2	(2.43 ± 0.05)x10^{12}	28.8
3.5	$SiO_{0.93}$	2.6	(2.88 ± 0.06)x10^{12}	17.7
3.5	$SiO_{0.85}$	3.0	(2.32 ± 0.05)x10^{12}	22.3
3.5	$SiO_{0.64}$	3.2	(1.95 ± 0.04)x10^{12}	24.6

3.3 Silicon Oxide Barrier Thickness Control

It will be shown in sec. 4.1 that the tunnelling probability is strongly dependent on the SiO_2 barrier thickness between adjacent Si NCs. Hence this barrier has to be engineered to be as thin as possible in order to achieve efficient carrier transport. According to the SL approach the vertical distance between the Si NCs is essentially controlled by the thickness of the SiO_2 diffusion barrier.

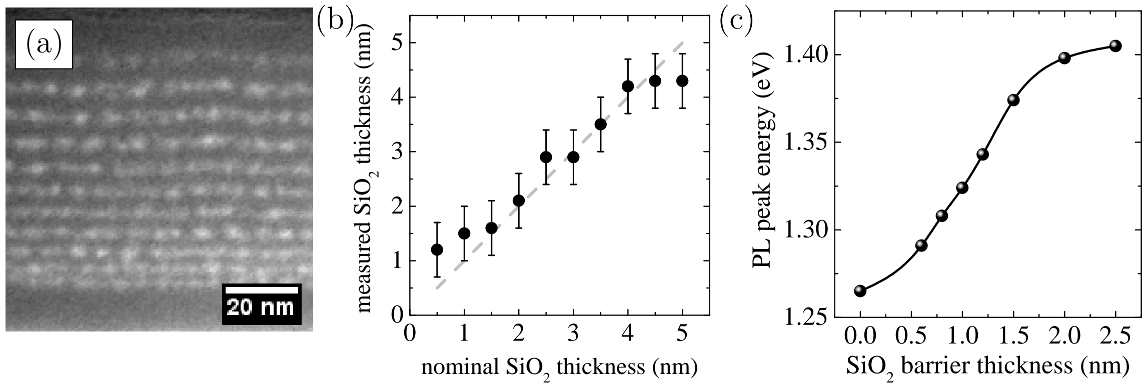

Figure 3.9: (a) EF-TEM image a sample, where the SiO_2 barrier thickness was varied from bottom to the top. The Si NC size was held constant by a 4 nm $SiO_{1.0}$ layer. (b) Evaluation of (a) that demonstrates the thickness control of the SiO_2 barriers. The error bars indicate an arbitrary ±0.5 nm variation. (c) PL peak energy as a function of SiO_2 barrier thickness for sample series B2 (Tab. 4.3). The value at 0 nm was obtained from a separate 200 nm $SiO_{0.93}$ bulk thin film. The line serves as guide to the eye.

Fig. 3.9(a) shows an EF-TEM image of a sample where the barrier is changed continuously throughout the SL from 0.5 nm to 5 nm in 0.5 nm steps and the SRON thickness and stoichiometry is held constant. It can be seen that the SL stacking is preserved for all SiO_2 thicknesses down to the second smallest barrier of 1.0 nm, whereas some particle coalescence is observed at 0.5 nm. A quantitative evaluation of the SiO_2 layer thickness obtained from an intensity depth profile is shown in Fig. 3.9(b). The measured SiO_2 thickness is quite close to the nominal one as indicated by the dotted line. A different way to probe the likeliness of layer coalescence is to measure the PL peak energy as a function of SiO_2 barrier thickness as displayed in Fig. 3.9(c). The PL peak energy is steadily increasing from 1.27 eV for the bulk layer with no diffusion barriers towards 1.41 eV for a 2.5 nm SiO_2 barrier, where the PL peak energy seems to approach a constant value. This may indicate some Si interdiffusion when the barrier is reduced leading to the growth of larger Si NCs at the expense of smaller ones. The continous trend allows to conclude that there exists no threshold thickness of the barrier, where it suddenly collapses. However, based on the TEM results (Fig. 3.9(a)), it can be argued that a 1 nm preserves the SL order to a large extent.

Another important aspect for electrical characterization is to realize good, ideally ohmic, contacts to the SL device. It is reasonable to assume that the contact SiO_2 barriers also have to be as thin as possible. We first consider now the top contact

to the Al gate. As shown in Fig. 3.4(a) the standard annealing using a 2 nm SiO_2 capping leads to a significant loss of Si at least for the topmost contact layer. The loss is partly avoided, when the capping layer is made sufficiently thick. Therefore, a 10 nm SiO_2 capping layer is used which has proven to sufficiently protect the Si NCs during annealing. It is apparent that this SiO_2 capping has to be removed prior to Al evaporation. As described in sec. 2.1.3, highly diluted HF has been used to etch the SiO_2. Fig. 3.10 demonstrates the influence of the HF etch time on the electrical properties of a particular SL sample.

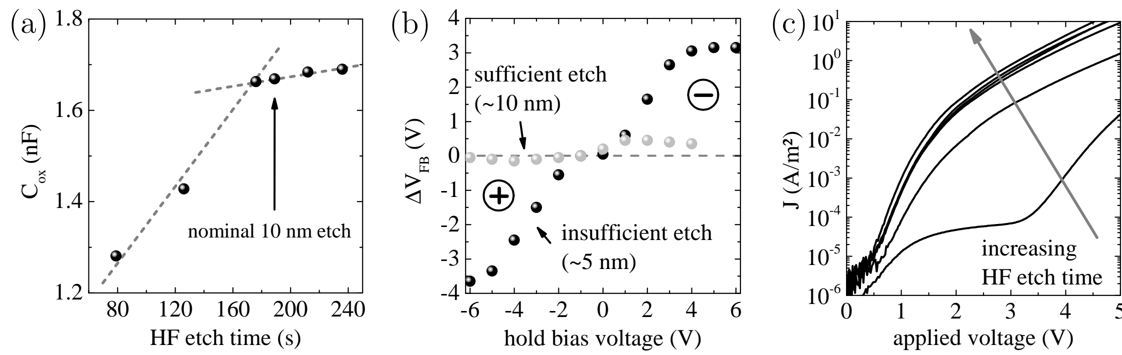

Figure 3.10: Influence of the electrical properties on the HF etch time on a 5 bilayer SL with 3.5 nm $SiO_{0.93}$ and 1 nm SiO_2 barrier. (a) the SL capacitance, (b) ΔV_{FB} determined from C-V as a function of charging voltage for two samples, (c) *J*-*V* curve for different etch times for the samples displayed in (a)

First of all, we see that the C_{ox} increases rapidly with etch time until the first Si NC layer is reached, where the change becomes very slow (Fig. 3.10(a)). Apparently, the topmost Si NC layer serves as a good etch stop. Moreover, it is observed from Fig. 3.10(b) that an insufficient etch leads to strong charging of electrons at positive bias and holes at negative bias, because the carriers cannot overcome the SiO_2 top barrier. Finally, it is shown in Fig. 3.10(c) that the current density increases by orders of magnitude, when the top SiO_2 is etched. At this point, it is referred to sec. 4.3 for a detailed discussion on the electrical properties of such SL films.

Fig. 3.11 displays four TEM images of samples (Tab. 3.2) that are later characterized electrically in sec. 4.3. In these underfocus TEM images, the layered SL structure is clearly visible for all samples down the 1 nm SiO_2 barrier. By integrating the image intensity along the layer growth direction, the individual layer thicknesses were determined [60] and are also listed in Tab. 3.2.

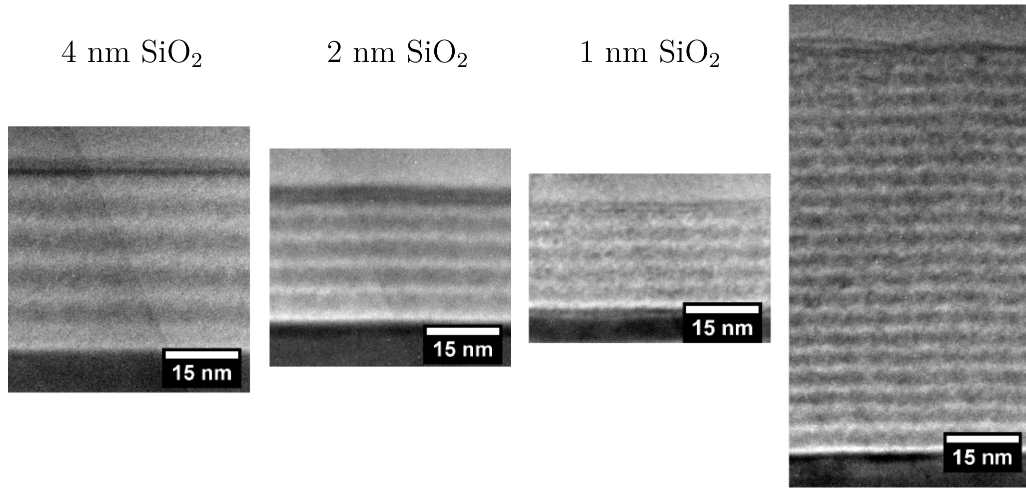

Figure 3.11: A series of underfocus TEM images for the samples listed in Tab. 3.2 (from left to right): 4 nm SiO_2, 2 nm SiO_2, 1 nm SiO_2 with 5 bilayers and 1 nm SiO_2 with 20 bilayers. The Al contact is always at the top, whereas the n-Si contact is at the bottom.

Table 3.2: TEM evaluation of the images presented in Fig. 3.11.

name	SL structure	d_{nom} (nm)	d_{TEM} (nm)	d_{SRON} (nm)	d_{SiO_2} (nm)
B1.1	5×(4nm SiO_2/3.5nm $SiO_{0.93}$)	37.5	39.7±1	3.6±0.2	3.9±0.2
B1.2	5×(2nm SiO_2/3.5nm $SiO_{0.93}$)	27.5	28.7±1	3.2±0.3	2.3±0.3
B1.3	5×(1nm SiO_2/3.5nm $SiO_{0.93}$)	22.5	21.9±1	2.4±0.4	2.0±0.3
N3	20×(1nm SiO_2/3.5nm $SiO_{0.93}$)	90.0	86.2±1	2.1±0.3	2.0±0.3

The SRON layer thicknesses should be constant for all samples. However, this is not the case as the SiO_2 layer thickness is decreased. In contrast the SiO_2 barrier appears larger than expected, but the total stack thickness is in good agreement with the nominal thickness. Hence, it can be concluded that the deposited SiO_2 thicknesses for sample B1.2 and B1.3 are in the range of 1 nm. From Fig. 3.11 the thickness of the first SiO_2 layer between the Si substrate and the first SRON layer is measured to about 50% larger than intended. This effect is possibly due to a parasitic oxidation of the Si substrate that is inherent to the here used PECVD process as we have found in a recent study [66]. On the other hand, the aluminum gate appears to be in direct contact with the topmost Si NC which further supports the view of a successful realization of the top contact.

3.4 Phosphorus-doped Silicon Nanocrystals

3.4.1 Phosphorus Quantification

The phosphorus concentration c_p in the as deposited film needs to be known in order to link the optical and electrical properties to the P incorporation. Therefore, two samples have been fabricated that consist of 50 nm SRON layers of varying doping concentration with a fixed Si excess (schematic in Fig. 3.12(a)) and varying Si excess at maximum PH_3 flow (schematic in Fig. 3.12(b)). The individual layers were separated by 10 nm of undoped SiO_2.

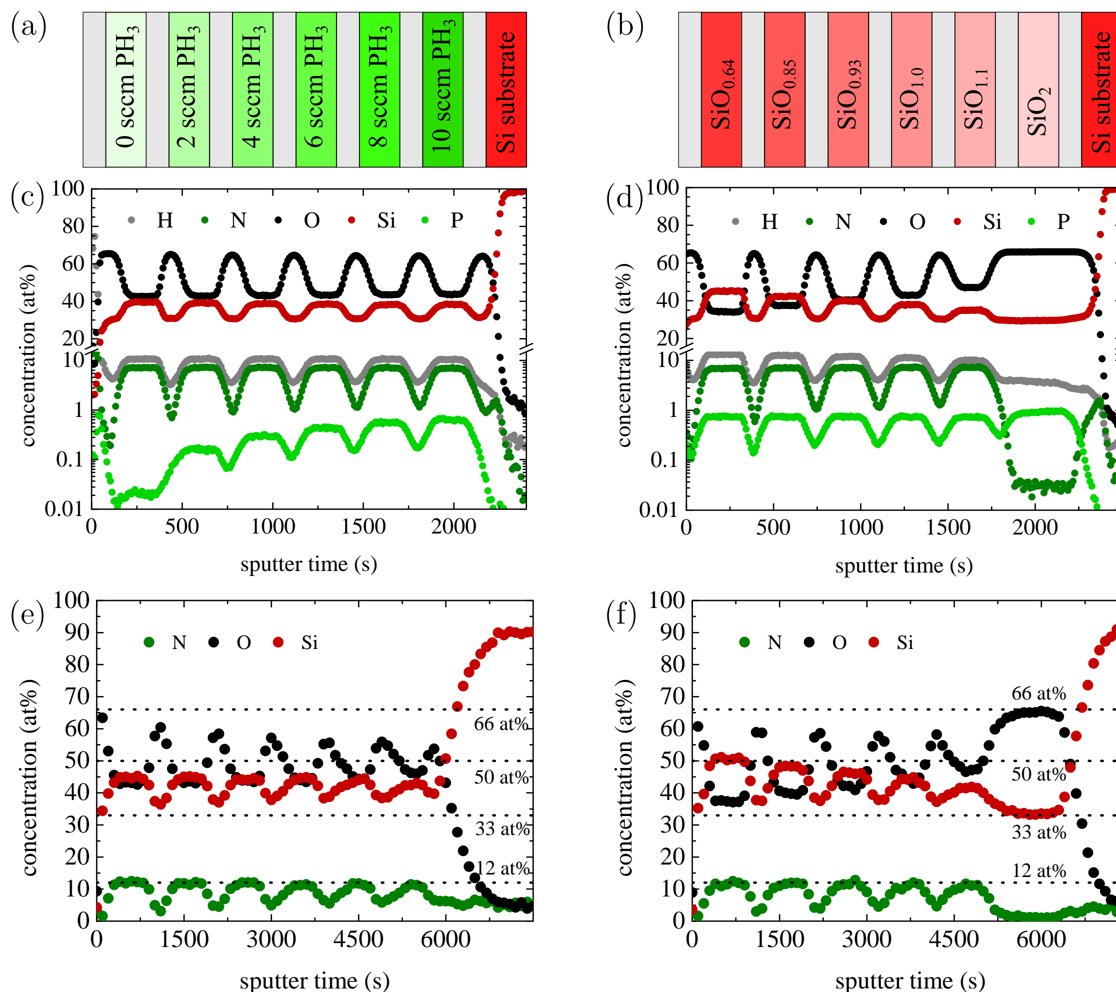

Figure 3.12: (a,b) schematic of the investigated layer stack (see text for further information), (c,d) MCs^+ depth profile, (e,f) XPS depth profile, where c_p is not shown because the signal was around the detection limit

The multilayers were measured in the as-prepared state using MCs^+ and XPS depth profiling (Fig. 3.12(c-f)). The following qualitative observations can be made by analyzing the graphs of Fig. 3.12:

- the as deposited films contain around 10 at% hydrogen
- c_p is linearly dependent on the PH_3 flow
- c_p is almost independent of the Si excess concentration
- an increase in c_p is accompanied by a small decrease of the Si excess
- even in the absence of a nominal PH_3 flow, a low amount of P is incorporated in the films possibly due to residual PH_3 in the PECVD chamber even after two pump steps and a 10 nm SiO_2 deposition
- there exists about 1 at% of nitrogen at the Si wafer interface that gradually decreases as the SiO_2 layer is grown
- the SiO_2 layer contains about 0.03±0.01 at% of N

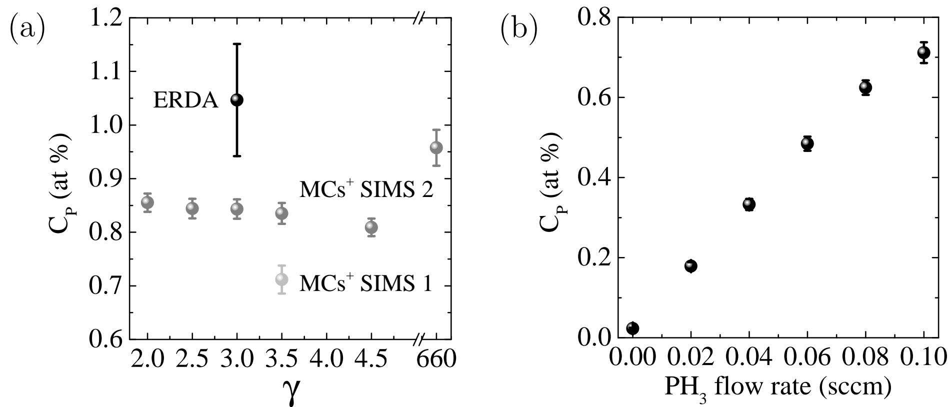

Figure 3.13: (a) extracted maximum of c_p as a function of the gas flow ratio of N_2O and SiH_4 (γ) - the ERDA error bar reflects the absolute measurement uncertainty, whereas the MCs^+ error bars only reflect noise in the plateau regions of Fig. 3.12 and no systematic error, (b) c_p as function of PH_3 flow rate showing the linearity of P incorporation

In Fig. 3.13, the measured c_p is shown as extracted from the data of the MCs^+ measurements including a reference ERDA measurement of a fully doped as deposited SRON bulk film. The MCs^+ data is about 20% below the ERDA measurement. However it has to be noted that the ERDA measurement is close to the detection limit and hence a significant error may be expected (Fig. 3.13(a)).

Taking into account the linearity of P incorporation (cf. Fig. 3.13(b)), it is reasonable to conclude that the maximum achievable c_p is about 1 at% at full PH_3 flow for any SRON stoichiometry and that it can be downscaled linearly. All c_p in the following samples are therefore calculated using the simple scaling law derived above which appears to be the best compromise.

3.4.2 Localization of Phosphorus

In this section, the localization of the P atoms of Si NCs/SiO_2 composite films after high temperature annealing is investigated. In the first part, XPS is measured on highly doped samples in order to obtain information on the chemical state of P. Due to the low sensitivity and ambiguity of XPS, the experiments are followed by XAS investigations with increased sensitivity that even allowed to measure a highly P doped Si reference wafer. Finally, APT is used on a selected sample to achieve three dimensional chemical mapping. All samples used in this study are summarized in Tab. 3.3.

Table 3.3: List of samples used to investigate the P localization

sample structure (nominal thickness in nm)	c_p (at %)	characterization
10 SiO_2 + 50x(5 $SiO_{0.93}$:P/5 SiO_2) + 10 SiO_2	0.5	XPS,APT
50 SiO_2:P	1.0	XPS
(111) Si(P) wafer (5-15 mΩcm)	0.013±0.009	XAS
30 SiO_2 + 300 $SiO_{0.93}$:P + 10 SiO_2	1.0	XAS
30 SiO_2 + 50x(5 $SiO_{0.93}$:P/2 SiO_2) + 10 SiO_2	0.71	XAS
30 SiO_2 + 50x(4 $SiO_{0.93}$:P/2 SiO_2) + 10 SiO_2	0.67	XAS
30 SiO_2 + 50x(3 $SiO_{0.93}$:P/2 SiO_2) + 10 SiO_2	0.60	XAS
30 SiO_2 + 50x(2 $SiO_{0.93}$:P/2 SiO_2) + 10 SiO_2	0.50	XAS
30 SiO_2 + 300 SiO_2:P + 10 SiO_2	1.0	XAS

3.4.2.1 X-Ray Photoelectron Spectroscopy

XPS is sensitive to the oxidation state of atoms and hence ideally suited to investigate the chemical environment of P. Since the XPS signal is very surface sensitive and due to the low sensitivity in the range of 1 at%, the annealing protection capping SiO_2 has been etched off by diluted buffered HF directly before the XPS measurement.

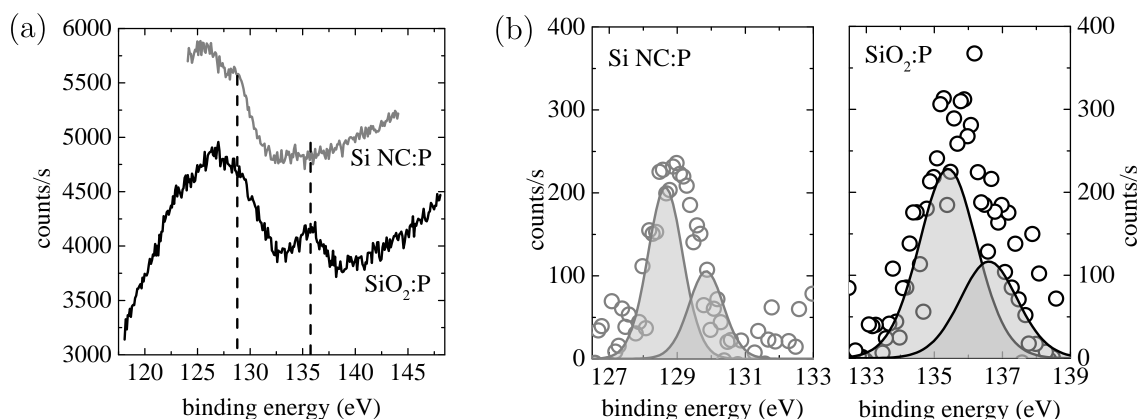

Figure 3.14: (a) P 2p high resolution scans of the two investigated samples (cf. Tab. 3.3). The upper curve is shifted by 1000 counts/s for clarity (b) doublet peak fitting for both samples after background subtraction

The P 2p scans of the doped reference SiO_2 and the Si NC sample are shown in Fig. 3.14(a). As can be seen the low intensity P 2p peak is situated in between two other broad peaks that arise from single and double scattering of Si 2p photoelectrons (99.6-103.4 eV) with plasmons (17-23 eV). This renders the background subtraction somewhat ambiguous. Nevertheless, the difference in the P 2p peak position is clear and by fitting the doublet peaks (Fig. 3.14(b)), the corresponding binding energies can be extracted. For P in SiO_2, a peak position of 135.4±0.2 eV is extracted suggesting a strongly oxidizing chemical environment of P^{5+} as in P_4O_{10} [87, 88].

In contrast, in the Si NC sample, such a peak cannot not be assigned considering the weak signal-to-noise ratio and the uncertainty in background subtraction. Instead, a peak appears at 128.6±0.2 eV which is close to a 129 eV peak found in similar investigations [89, 90]. For comparison, the peak energy of elemental P is at 130±0.2 eV [87] which corresponds to P^0 suggesting an effective negative charge state, possibly P^{-1}, for the P atoms in the Si NC sample.

It is well accepted that chemical shifts in XPS scale with the bond polarity. The electronegativity difference between Indium (In) and P is about twice as large as

between Si and P. Using the P 2p binding energy in InP of 127.3 eV [91] and the P^0 reference value, a binding energy of substituitional P in Si of ≈128.65 eV can be estimated by linear interpolation. The value is remarkable close to the measured P 2p peak position. While it was not possible to measure a P doped Si reference here, the P 2p peak was measured previously for heavily P doped Si and a peak at 129.3 eV was attributed to elemental P in the form of small P clusters or P interstitials [92, 93]. It was argued that a P donor peak is expected to have a binding energy of around 130.5 eV, 1 eV above that of elemental P.

3.4.2.2 X-Ray Absorption Spectroscopy

The low sensitivity of XPS and the difficulties in background subtraction shifted the attention towards measuring the X-ray absorption at the P K-edge. The XANES spectra for different nominal Si NC sizes and the reference samples are shown in Fig. 3.15(a). Clear peaks at the P K-edge are observed for all samples. These peaks are commonly referred to as white lines [61] and indicate transitions from the electron core level to the continuum of states.

Let us first consider the P doped SiO_2 reference sample in Fig. 3.15(a). The intense white line appears at 2152.4±0.1 eV which is in the range characteristic for PO_4 tetrahedra [94]. In addition the white line exhibits a shoulder at the low energy side and a small pre-edge peak which is characteristic for transitions to bound electronic states [61]. Plotting the derivative of the fluoroescence yield (FLY) with respect to energy (Fig. 3.15(b)) allows then to identify the absorption edge and two bound state transitions defined by the inflection point of the FLY that appear as maximum in the first derivative. The positions are marked by dashed lines in Fig. 3.15(b) and are 2151.8±0.1 eV , 2150.8±0.1 eV and 2148.1±0.1 eV respectively. The corresponding bound state energies ε_{T1} and ε_{T2} with respect to the continuum of states, i.e. the SiO_2 conduction band, are indicated in the inset of Fig. 3.15(b).

When looking at the Si NC and Si:P reference samples in Fig. 3.15(a), there is a substantial low energy shift of the white line intensity as compared to the doped SiO_2 sample. The Si:P reference peak is found at 2144.9±0.1 eV, very close to the P K-edge observed in P doped Si nanowires at 2145 eV [95]. In contrast, the white line of the Si NC samples is shifted down by 1.1 eV for all Si NC sizes to 2143.8±0.1 eV (see Fig. 3.15(c)), significantly below the absorption peak of elemental P at 2144.5 eV [96]. These results strongly support the picture that was already developed for the

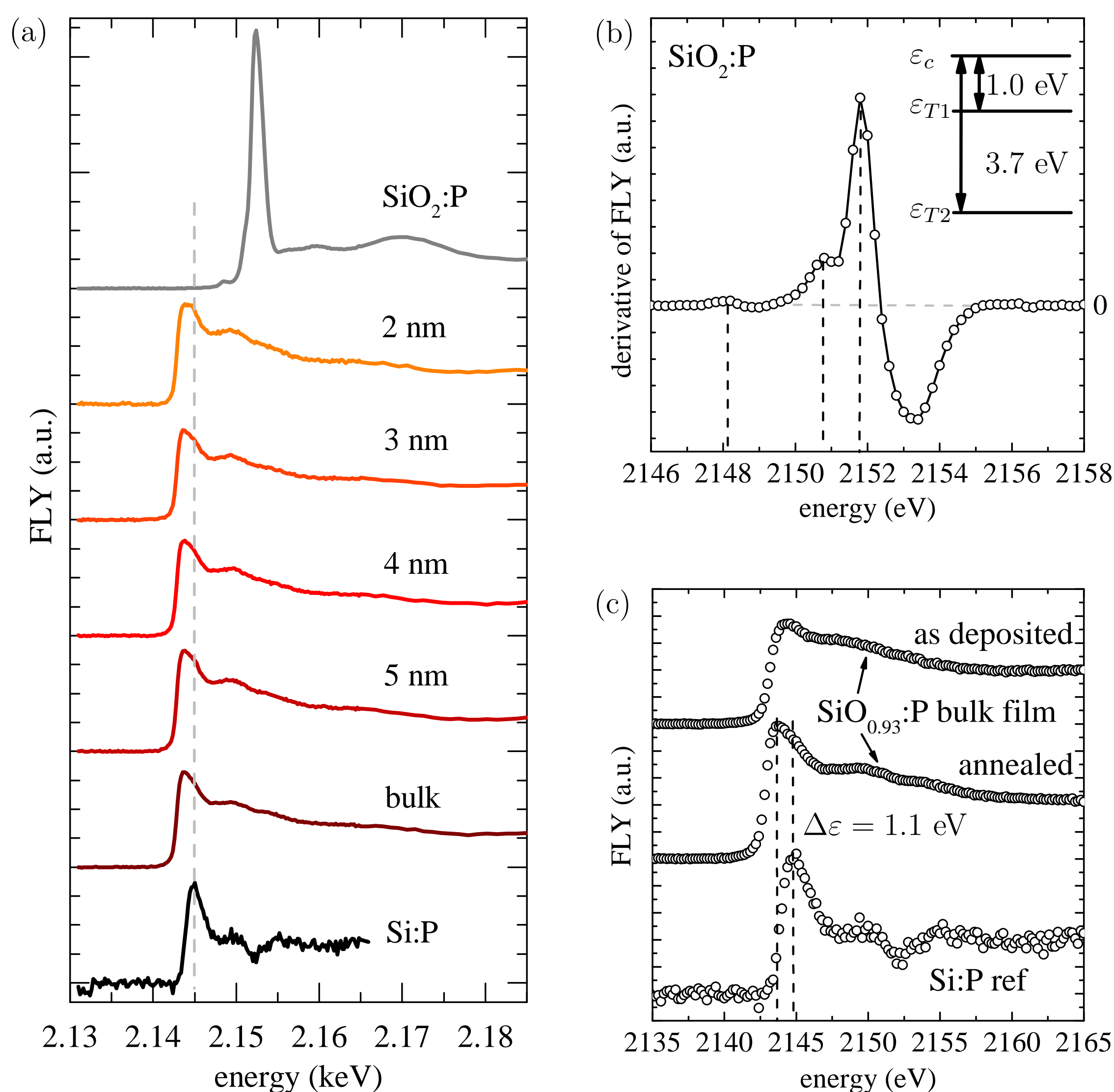

Figure 3.15: (a) XANES of the P K-edge of several P doped Si NC samples and reference samples indicated in Tab. 3.3, (b) derivative signal of the SiO_2:P sample, the dotted lines indicate the absorption edge and the bound state transitions, the inset shows the proposed interpretation of the relative energies, (c) XANES comparison of a typical P doped Si NC sample with the Si:P reference sample

XPS measurements: the majority of P atoms seems in fact localized within the Si NCs and the donor electron is effectively bound to the P nucleus.

The P K-edge spectra of the Si NC samples are remarkably similar and no size dependent features are visible (cf. Fig. 3.15(a)). Hence, it is sufficient to look at the XANES region of the bulk Si NC sample and comparing it with the Si:P reference (Fig. 3.15(c)). In general, the absorption edges consist of a white line peak followed

by a constant absorption level due to the continuation of electron transitions into the continuum of states. This lineshape is modulated by contributions from multiple scattering of high kinetic energy electrons with neighboring atoms and thereby carries direct information on the chemical environment of the absorbing atom [61]. Such oscillations are visible for the Si:P reference (Fig. 3.15(c)). In comparison, the white line of the Si NC samples falls off less steeply than the reference resulting in a broad shoulder towards higher energy. This may indicate the presence of intermediate oxidation states of P, possibly originating from P localized at the interface between the Si NCs and the surrounding matrix. In order to substantiate such a conclusion, the XANES spectrum is also shown for the same film in the as deposited state, where a mixed bonding configuration is expected. Clearly, the features are blurred out even further due to the random bonding nature of the P doped SRON layer.

Finally, the obtained P K-edge XAS results shall be compared qualitatively to similar Si K-edge measurements, because the difference between substituitional P in Si and pure Si features should be small [95]. Therefore, Si K-edge measurements have been taken from [97] and are compared to P K-edge results by referencing to the respective white line. The comparison is presented in Fig. 3.16.

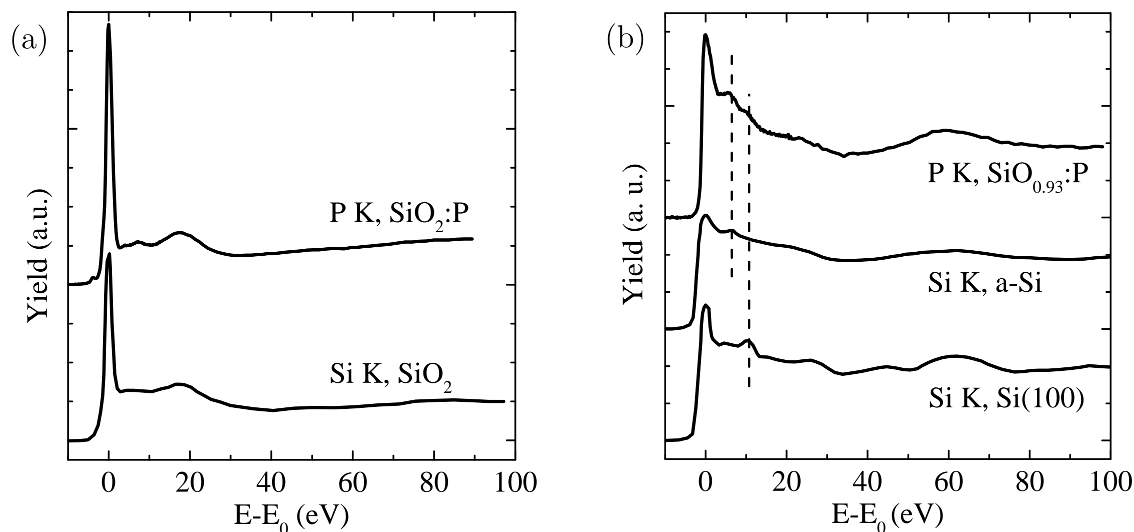

Figure 3.16: XAS spectra of the here studied P K-edge compared to the Si K-edge of (a) SiO_2, (b) crystalline Si and amorphous Si. The data is taken from [97].

The features in the SiO_2 are very similar (Fig. 3.16(a)), indicating that the chemical environment of P atoms is most likely similar to the Si sites in the amorphous Si-O

network as it was already expected from the results of Fig. 3.15(a). The situation is less clear-cut for the Si NC samples which are compared to amorphous Si and crystalline Si in Fig. 3.16. It appears that the two bumps following the white line can be also explained by a mixture of amorphous and crystalline Si features surrounding the P atom. In particular, the multiple scattering features of the initial white line at the lowest oxidation state fall in the range of higher oxidation states.

Furthermore, the distinct oscillations observed for crystalline Si are significantly blurred in the Si NC sample. In fact, this analogy demonstrates that the question of whether the blurring is due to P embedded in a crystalline or amorphous surrounding or due to overlapping of several distinct oxidation states cannot be disentangled on the basis XAS measurements alone. Therefore, it is advisable to analyze the sample crystallinity as a function of P doping with a different method such as Raman or X-ray diffraction which is beyond the scope of the present work. Please note however that such experiments show that P actually enhances the Si crystallization [98].

3.4.2.3 Atom Probe Tomography

APT has been carried out on a selected sample in order to obtain three dimensional insight into the distribution of P within the SL. Here, the data evaluation is mainly focussed on the P localization, but an in depth discussion of the APT analysis can be found elsewhere [99]. Fig. 3.17(a) shows the integrated concentration depth profile of Si, O and P after data reconstruction. A clear correlation exists between regions of enhanced Si concentration and c_p indicating already that the majority of P resides within the SRON layers. A similar tendency has already been obtained by time-of-flight secondary ion mass spectrometry (ToF-SIMS) [89, 100], but cannot be measured by means of EELS or EDX linescans in the TEM due to the low P content (not shown). Please note that the nitrogen in the sample is not considered in the analysis due to the overlap with the Si^{2+} mass signal.

A three-dimensional reconstruction of the SL is shown in Fig. 3.17(b). Regions of increased Si concentration are shown by using iso-concentration surfaces with at least 70 at% Si atoms, whereas individual P atoms are representated by green dots. In total about 350 particles are found using this approach and the SL ordering is clearly observed. Significant amounts of P atoms are detected within the matrix, whereas P atoms within the Si NCs are masked by the Si iso-concentration surfaces in this representation. The Si particles appear more spherical in comparison to the

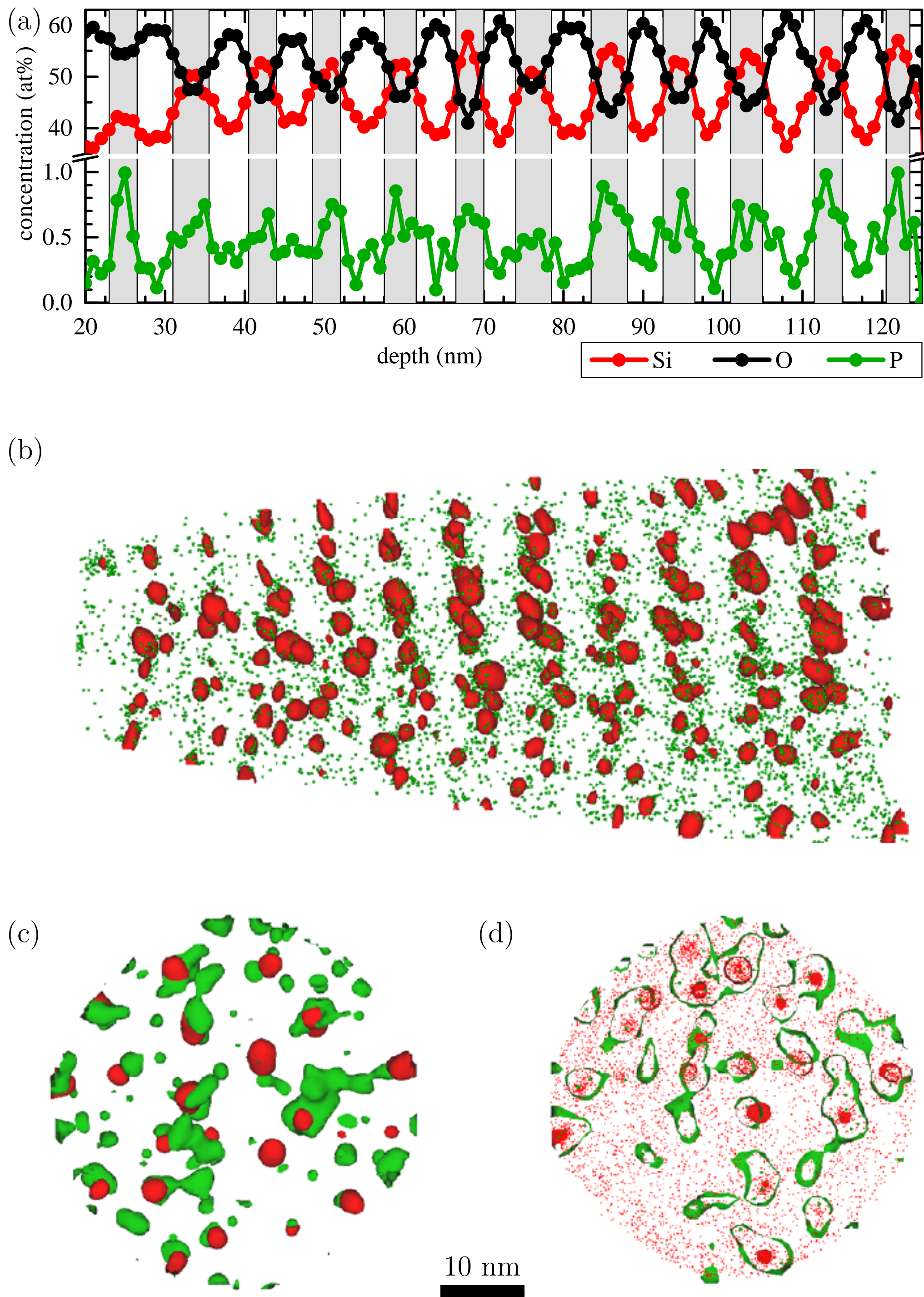

Figure 3.17: APT data analysis after reconstruction (the analysis direction was from left to right): (a) integrated concentration depth profile, (b) three-dimensional reconstruction of the analyzed volume, the green dots are P atoms, whereas the red surfaces are iso-concentration surfaces containing more than 70 at% Si, (c) a 8 nm slice taken from (b). In addition P isosurfaces with more than 1.3 at% P are shown in green, (d) a 0.3 nm slice. The isosurface peripheries are visible due to the extreme thinness. Additionally, individual Si atoms are displayed as red dots.

single layers imaged in plane-view (cf. Fig. 3.7), supporting the argument in sec. 3.2 that a larger thermal budget leads to a higher sphericity of the particles.

In Fig. 3.17(c), a slice of a SL bilayer is shown from the top view and individual P atoms have been replaced by green iso-concentration surfaces of at least 1.3 at% of P atoms. These P iso-surfaces seem to partially cover and penetrate the Si clusters. Furthermore regions of enhanced c_p are found within the matrix. Both features become more evident, when a thinner slice of 0.3 nm is selected (Fig. 3.17(d)), where the cross-sections of the iso-surfaces become visible. From the visual inspection of the APT data, it appears that there exists some correlation between the regions of enhanced Si and P concentrations.

In order to evaluate the data in a more quantitative way, a so-called proxigram is constructed based on the Si iso-concentration volumes. In the proxigram method, a concentration profile is obtained by integrating across iso-concentration surfaces [101]. In this way an averaged radial concentration profile is obtained for spherical particles.

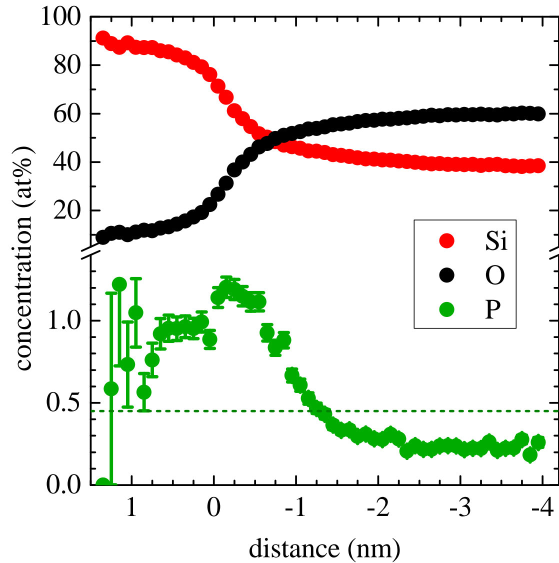

Figure 3.18: A proxigram derived from iso-concentration surfaces shown in Fig. 3.17(b). The positive distance points towards the interior of the Si NCs. The green dotted line marks the average c_p of the sample. The P accumulation at the interface region is apparent.

First of all, it can be seen in the proxigram (Fig. 3.18) that the Si concentration saturates at around 88 at%, i.e. a substantial amount of oxygen is detected within

the Si clusters. In fact, this is a result of a common APT reconstruction artifact known as local magnification effect [102, 103]. It occurs in composite materials, when regions of different atomic evaporation rates are present. This leads to surface inhomogeneities that cause the ion trajectories to overlap [104]. Indeed, it is commonly observed in APT for Si NC/SiO_2 samples [105, 106].

However, more importantly c_p peaks exactly at the transition region between the matrix and the Si cluster core, indicating a P surface segregation. Remarkably, P is enhanced in both the Si cluster and at the cluster boundary and reduced in the matrix region with respect to the average P concentration within the sample denoted by the green dotted line.

Since the iso-concentration surfaces serve as purely visual representation not allowing to extract data for individual clusters, a different data treatment is needed to characterize the amount of P atoms within the Si clusters. Therefore, a cluster identification algorithm was applied in order to identify groups of atoms that belong to the same cluster (see [99] and references therein for a detailed discussion on the cluster algorithm). 320 clusters are found using the algorithm. As an example, Si clusters of a selected slice are shown in Fig. 3.19(a) including P atoms from only within the clusters that are marked by enlarged green dots. The mean particle size determined in this way is 3.7±0.8 nm following roughly a log-normal distribution (cf. Fig. 3.19(b)). The mean cluster atomic concentrations are c_p=0.77±0.4 at%, c_o=12.3±2.1 at% and c_{si}=85.3±2.1 at% which corresponds to the plateau region in the proxigram (Fig. 3.18). Using the data, it is possible to obtain the detected number of P atoms for each individual cluster and group the clusters according to their average size. In this way, size-dependent cluster statistics can be derived. The probability to find k P atoms within a cluster of volume V_{nc} is expected to follow a Poisson distribution [100, 107]:

$$p(k) = \frac{\exp\left(-\lambda_p\right)\lambda_p^k}{k!} \tag{3.1}$$

Here λ_p is the expectation value of the number of P atoms within the cluster, i.e.:

$$\lambda_p = c_p V_{nc} \rho_{atom} \tag{3.2}$$

where ρ_{atom} is the measured cluster atomic density. The distribution of P atoms within the Si NCs is plotted together with Poisson distribution fits in Fig. 3.19(c) for five classes of cluster diameters. While the data scatters significantly due to the

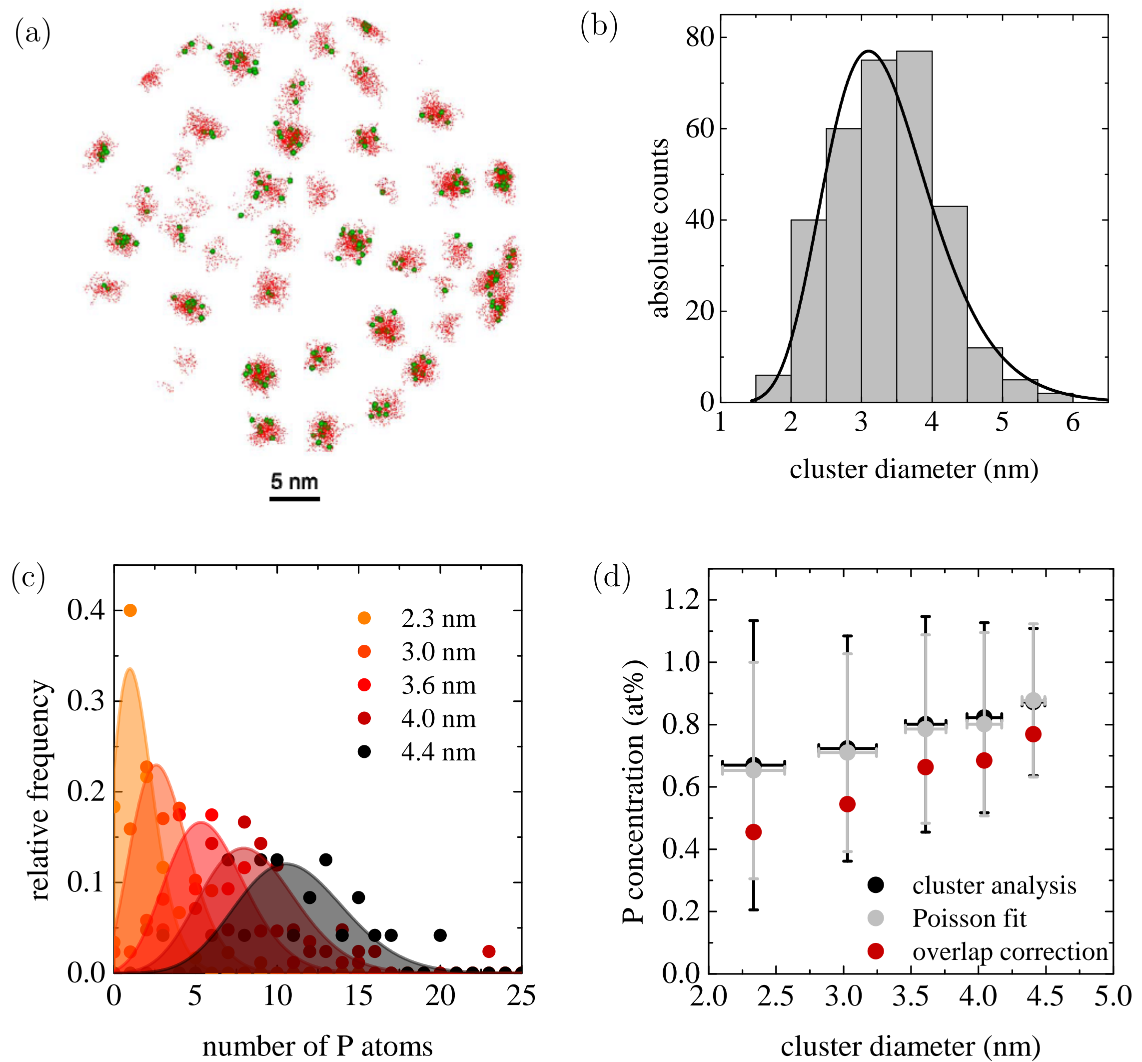

Figure 3.19: Cluster analysis evaluation of the APT measurements (a) single layer of Si NCs determined from the cluster analysis only showing atoms belonging to the identified clusters (red dots: Si, green dots: P). (b) Size distribution of the clusters fitted with a log-normal distribution. (c) Poisson distribution fits for the number of P atoms within Si NCs of different size derived from the cluster analysis. (d) Size-dependent P concentration derived from the cluster analysis. The error bars of the overlap correction are omitted for clarity.

limited number of clusters, it is clear that larger clusters contain on average more P atoms as it is expected from eqn. 3.2. It is important to note that the real number of P atoms within the Si NCs must be increased with respect to the measured values due to the limited detection efficiency of the APT. For a detection efficiency of 36%, the amount of dopants is increased by a factor of ≈2.8. It implies that a 4.5 nm Si NCs would contain around 30 P atoms, whereas a 2.0 nm Si NC would contain

around 3 P atoms on average.

Fig. 3.19(c) is not suitable to evaluate a possible self-purification mechanism [37, 43]. However, the cluster analysis allows to plot the average c_p as a function of cluster size directly as shown in Fig. 3.19(d) by the black data points. A trend of decreasing c_p with smaller cluster diameter is observed, but the statistical error is substantial. One may also use eqn. 3.2 and solve for c_p using the values of ρ_{atom} for the different subsets of clusters. In this way, the same trend is observed, but the magnitude of the error bars is somewhat decreased because it is now mainly arising from the spread in V_{nc} and ρ_{atom}.

In addition, as it was mentioned above, the local magnification effect artificially projects atoms originally located at the interfaces into the clusters. It can be corrected by defining an overlap rate η which is the ratio of projected atoms divided by the true number of atoms in the cluster [108]. Using this definition, the true P concentration c_p^* in the cluster can be calculated by [108]:

$$c_p^* = c_p + \eta(c_p - c_p^s) \tag{3.3}$$

where c_p^s is the P concentration in the region surrounding the cluster. The value of c_p^s is taken as the peak interface concentration in the proxigram (Fig. 3.18), because the projected atoms usually come from a 0.3 nm thin shell surrounding the particle [108]. The overlap rate η can be estimated provided that the cluster consists of pure Si which is well justified in the present case. Hence all the oxygen atoms must be projected into the Si NC. By assuming an interface stoichiometry of SiO, the overlap rate η can be calculated:

$$\eta = \frac{2N_O}{N_{Si} - N_O} \tag{3.4}$$

Here, N_O and N_{Si} are the total number of detected oxygen and silicon atoms within the clusters respectively. In fact the apparent oxygen concentration within the clusters as well as the cluster atomic density are a decreasing function of the cluster size. Subsequently, η is also size dependent and ranges from 0.41 to 0.31 for the cluster diameters from 2.3 nm to 4.4 nm. Applying eqn. 3.3 for the P concentration allows to calculate c_p^* due to the overlap correction (Fig. 3.19(d)). The correction brings about a significant decrease in the P concentration within the clusters and intensifies the size dependence.

As demonstrated in Fig. 3.17 and in the proxigram (Fig. 3.18), there is a clear pile up

of P at the Si NC/SiO_2 interface region culminating at about 1.2 at%. In addition, the c_p within the matrix is at 0.25 at%, whereas the overall c_p was measured to be 0.45 at% shown by the green dotted line in Fig. 3.18. It is now desirable to calculate the fraction of P atoms that are incorporated in the Si NCs, trapped at the interface or dissolved in the surrounding matrix. The total number of detected P atoms (9800) must then be equal to the sum of P atoms in the individual regions. Let us further define V_i and ρ_i to be the volume and atomic density of the three distinct sample regions denoted by the index i respectively. Then the number of P atoms in each of these regions is calculated by

$$N_{p,i} = c_{p,i} V_i \rho_i \tag{3.5}$$

In addition, it is required that the measured total volume $V_{total} \approx 1.64 \times 10^5$ nm^3 matches the volumes of the subregions

$$V_{total} = \sum_i V_i \tag{3.6}$$

and that the total number of detected atoms N_{total} matches the sum of atoms in the three regions:

$$N_{total} = \sum_i V_i \rho_i \tag{3.7}$$

The problem is now to find a self-consistent solution to the set of equations described above. This is realized by assuming spherical clusters and attributing to each of them an interface shell of a fixed thickness. This directly yields the volume occupied by the interface and using eqn. 3.6 gives the matrix volume. Using the atomic density of the matrix $\rho_m = 15.1$ atoms/nm^3 determined solely from within the barrier layers in Fig. 3.17(b), it is possible to calculate the atomic density in the interface shell from eqn. 3.7 and thereafter the total number of P atoms in each region by applying eqn. 3.5. The sum of all P atoms in the three regions must then match the total number of P atoms found in the measurements.

Thus, the interface shell thickness is increased continuously until convergence is reached. Using this algorithm an interface shell thickness of 0.84 nm is determined, well in agreement with the approximate width of the interface region in the proxigram (Fig. 3.18) and a similar work [105]. The calculated data is reported in Tab. 3.4, where ν_i is the fractional volume occupied by the respective region and

p_i and p_i^* is the probability to find a P atom in the respective region before and after overlap correction. In the final analysis, only about 15-20% of the P atoms are incorporated into the Si NCs, whereas about 30% are trapped at the interface and more than 50% reside in the surrounding matrix.

Table 3.4: Summary of the APT P localization analysis for the three different sample regions described in the text.

sample region i	$N_{p,i}$	ν_i	p_i	p_i^*
matrix	5329	0.86	0.54	0.54
Si NC	1761	0.05	0.18	0.14
Si/SiO_2 interface shell	2720	0.09	0.28	0.32

It is important to mention that the employed P dopant concentrations appear extremely high. In fact, the solid solubility limit of P in Si is about 2.5 at% [109], but the electrically active P concentration that can be achieved is one order of magnitude lower at about 0.25 at% [110]; lower than the here reported lowest concentration of P for the smallest Si NCs. In addition, such high P concentrations may promote the creation of Si selfinterstitials [111–115]. In contrast, the solid solubility of P in SiO_2 is only about 0.01 at% [116], a value that is greatly exceeded here by more than one order of magnitude. Thus one would expect P_2O_5 clustering in the SiO_2 layer. A certain tendency of P clustering is observed in Fig. 3.17(c) and (d) already. However, efficient cluster formation is hindered by the low diffusivity of P in SiO_2. The different solubilities of P in Si and in SiO_2 suggest that at low concentrations, P prefers to stay in Si. This fact is substantiated by a bulk segregation coefficient, defined as the ratio of P atoms in Si and SiO_2, in the order of 10 [117]. In contrast, the present sample yields a segregation coefficient of around 0.5, much smaller than the bulk counterpart. This result may be interpreted in terms of the nanocrystal self-purification process [37, 39, 43] which has been proven already for gas phase synthesized Si NCs [44, 118]. Finally, one may wonder, how to define a physical doping efficiency for the present case. For instance, from Tab. 3.4, it can be seen that around 20% of the P atoms are within the Si NCs, while the Si NCs only take up 8% of the entire sample volume yielding a physical doping efficiency of about 250%. On the other hand, considering just the solid solubility limits in Si and SiO_2, nearly all P atoms should be within the Si NCs giving rise to a physical doping efficiency of only 20% instead.

3.4.3 Photoluminescence Behaviour

P doping is often reported to increase the PL intensity of Si NC ensembles as compared to the undoped case [107, 118–125]. This is commonly explained by a deactivation of non-radiative channels by reduction of interface defects as a consequence of P doping [119, 120, 124, 125]. On the other hand, it has been calculated that radiative transition rates in P doped Si NCs are enhanced [126, 127]. In addition, PL quenching is often observed [100, 107, 118, 122–124] at high c_p which is preferably explained by three-body Auger recombination where the exciton transfers its energy to the P donor electron.

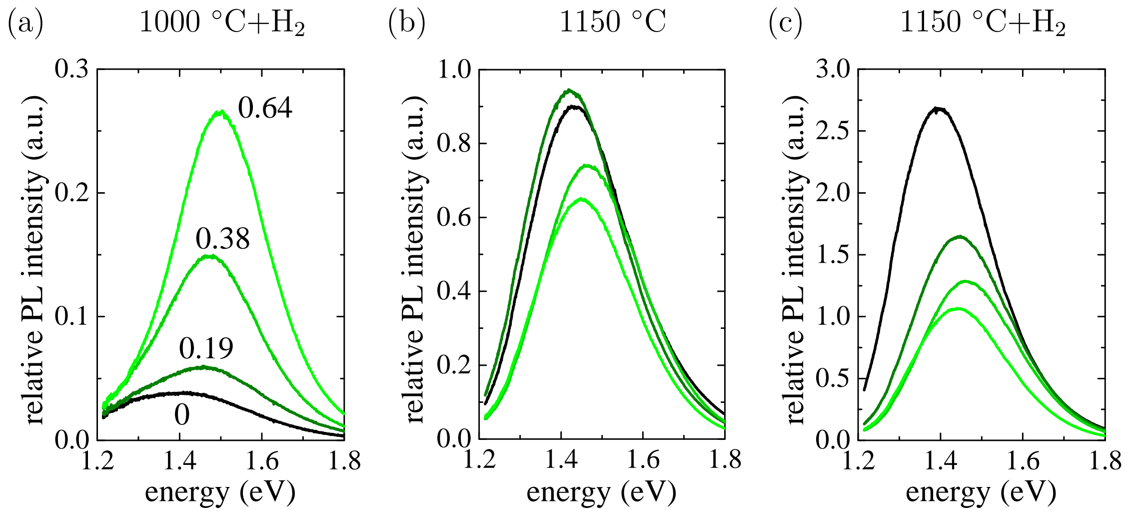

Figure 3.20: PL spectra of a series of P doped SLs treated with different annealings. 20 bilayer SLs have been used with 3.5 nm $SiO_{0.93}$ and 2 nm SiO_2. The P concentration in at% is indicated by the numbers next to the spectra in (a). The samples were annealed in N_2 atmosphere for 1 h and the indicated temperature. For (a) and (c) the standard H_2 passivation annealing was employed.

First of all, it is demonstrated in Fig. 3.20 that PL enhancement, PL quenching and a mixed behaviour can be achieved using the same samples subjected to different annealing conditions. In Fig. 3.20(a), the PL intensity increased steadily with increasing c_p and is enhanced by almost an order of magnitude for the highest P concentration. Furthermore, there is a clear high energy shift upon P doping. It may be related to the slightly decreased Si excess concentration (cf. Fig. 3.12) leading to smaller Si NCs on average (cf. Fig. 3.8). Since this change is really small, a different explanation could be the observation that P reduces the crystallization temperatures

of Si NCs [98] resulting in the creation of smaller clusters. In addition, the latter would contribute to an enhanced PL intensity that could otherwise be explained by P induced defect passivation.

The sensitive interplay of P induced PL enhancement and quenching becomes clear when comparing Fig. 3.20 (b) and (c). Before hydrogen passivation, small amounts of P increase the PL intensity, whereas high amounts have the opposite effect. However, after passivation all P doped samples show PL quenching. Assuming that the hydrogen passivation of Si surface defects is not affected by the presence of P, it can be concluded that P induced passivation and quenching mechanisms coexist [100]. Therefore PL studies of P doped Si NCs are ambiguous and its interpretation remains mostly speculative.

As can be seen in Fig. 3.20(b) and (c), the PL quenching occurs on a rather linear scale, meaning that only a few 10% of all Si NCs contain a P related quenching center. The samples contain Si NCs with a tight size distribution around a diameter of 2.5 nm (cf. Fig. 3.7(c)), but it is noted that they are possibly larger as explained in sec. 3.2. Hence, from Fig. 3.19(c) a Poisson parameter λ_p of 2 can be estimated. Assuming now that the P distribution in this sample will not be so much different here compared to the APT sample, we can scale λ_p according to the nominal c_p of the samples and correct it for the APT detection efficiency. We obtain values of 2.7, 5.4 and 9.0 for the increasing P concentrations given in Fig. 3.20(a). The probability to find no P atom within a Si NC is then simply given by $p(k = 0) = \exp(-\lambda_p)$, i.e. the number of P free Si NCs decreases exponentially, when the P concentration is increased linearly. For λ_p =9.0 (the sample of the highest P concentration), one obtains only 0.01% of pure Si NCs. It is obvious from the comparably strong PL emission in Fig. 3.20(b) and (c) that the non-radiative three-body Auger process is either much less efficient than expected or the P induced states are almost optically inactive. In fact, while the previous estimation was made for rather small Si NCs, the calculated effect increases drastically, when larger Si NCs are considered. However, the PL behaviour of samples with larger Si NCs is very similar to the measurements in Fig. 3.20.

Finally, please note that the doping concentration range employed here leads mostly to multiple dopants per Si NC. Considering that singly doped nanocrystals are still not well understood, the effect of multiple dopants is rarely considered in theory. This is in stark contrast to experimental work, where multiple dopants occur frequently [128–131].

4 Charge Transport

This chapter begins with a description of charge transport from a single carrier perspective, namely a theoretical description of the single electron transfer process between two neighboring Si NCs. The theory was first applied by Brus to explain PL quenching effects of porous Si in water [132]. The view is then changed to a macroscopic point in order to understand the shape of the measured current density vs. electric field (J-E) characteristics. This is important, because the undoped SLs contain only a neglible amount of free carriers and hence space-charge effects dominate the J-E characteristics. Thereafter, the results of electrical measurements are presented and discussed on the basis of the theoretical considerations made before. The chapter is concluded by a classification of transport regimes.

4.1 Microscopic Transport

4.1.1 Quantum Confinement

The solution of the Schrödinger equation for the spatial confinement of the electrons in Si NCs leads to discrete allowed energy levels and a probability density. The complete density of states of a Si NC is of interest for many scientific questions such as the relaxation of hot carriers [133] and charge transport as will be shown later. In general, quantum dots are referred to as artificial atoms because the wavefunctions at the discrete levels of allowed energy are similar to the atom-like description. Hence the lowest conduction band states in a Si NC are similar to a s-orbital, but six-fold degenerate due the six energy minima in the Si conduction band. Their shape is however ellipsoidal due to the Si effective mass anisotropy [134]. Furthermore, the degeneracy is lifted due to intervalley coupling and splitting energies of 68 meV were calculated for a small Si NCs (d =1.85 nm) [134]. Using a tight binding parametrization that is fitted to the Si bulk band structure [134], the general relationship of the conduction band shift $\Delta\varepsilon_C$ and the valence band

shift $\Delta\varepsilon_V$ was established as a function of the Si NC diameter D (cf. Fig. 4.1 for a graphical representation):

$$\Delta\varepsilon_c\left(D\right)/eV = \frac{5.8445}{(D/nm)^2 + 1.274(D/nm) + 0.905} \tag{4.1}$$

and

$$\Delta\varepsilon_v\left(D\right)/eV = \frac{-6.234}{(D/nm)^2 + 3.391(D/nm) + 1.412} \tag{4.2}$$

eqn. 4.1 will be used in sec. 4.1.6 and sec. 4.1.7. Please note that a more complete parametrization of the Si NC density of states is not available to date.

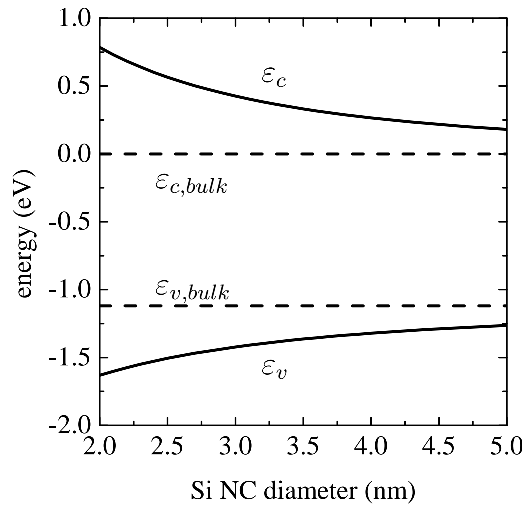

Figure 4.1: Lowest conduction band state and highest valence band state as a function of the Si NC size, the energy is referenced to the Si bulk conduction band

Due to the finite size of the barrier, the electron wavefunction penetrates into the barrier region which is of particular interest for electron transfer time calculations (see sec. 4.1.6). Thus, once the electronic energy levels have been obtained, the total wavefunction within the Si NC and in the surrounding matrix region need to be calculated. It is possible to obtain a general solution to the Schrödinger equation for

a spherical quantum dot embedded in a finite barrier material as shown in sec. A.1:

$$\psi_R(r) = \begin{cases} \propto \sin(\alpha r)/r & \text{if } r \leq R \\ \propto \exp(-\beta r)/r & \text{if } r > R \end{cases} \tag{4.3}$$

with

$$\alpha = \left[\frac{2m_{Si}(|\varepsilon_1|)}{\hbar^2}\right]^{1/2} \tag{4.4}$$

$$\beta = \left[\frac{2m_{ox}(V_0 - |\varepsilon_1|)}{\hbar^2}\right]^{1/2} \tag{4.5}$$

Here, m_{Si} and m_{ox} are the electron effective mass in the Si NC and the matrix respectively, ε_1 is the energy of the first confined state that can be calculated by means of eqn. 4.1 and V_0 is the conduction band offset between Si and SiO_2. The two parts of the wavefunction are subject to boundary conditions described in sec. A.1. Fixing now the energy level, mathematically enforces a value of m_{Si}. In this crude way, solutions of more elaborate calculations may be expressed in terms of simple effective mass analytical solutions. Please note that for all Si NC sizes of interest in the present work, the indirect nature of the Si bandgap is preserved [135, 136] which does not follow directly from the description of s-like energy states. In addition, it has been shown that the nature of the interface affects the wavefunction and energy [136–139].

4.1.2 Charging of a single Silicon Nanocrystal

When a single Si NC is charged by an electron or hole, the charge interacts with the dielectric surroundings and hence its energy is affected. The corresponding energy shift of conduction band or valence band is called the self-energy Σ (Fig. 4.2(a)) and can be calculated from a macroscopic electrostatic approach [40]:

$$\Sigma(D) = \left(\frac{1}{2}\left(\frac{1}{\epsilon_{out}} - \frac{1}{\epsilon_{in}}\right) + \frac{0.466}{\epsilon_{in}}\frac{\epsilon_{in} - \epsilon_{out}}{\epsilon_{in} + \epsilon_{out}}\right)\frac{q^2}{2\pi\epsilon_0 D} \tag{4.6}$$

Here, ϵ_{in} and ϵ_{out} are the relative dielectric constants of the Si NC and the matrix respectively. Adding yet another electron or hole to the Si NC, leads to an additional energy shift (Fig. 4.2(a)). This coulomb charging energy U is calculated in a similar

manner [40]:

$$U(D) = \left(\frac{1}{\epsilon_{out}} + \frac{0.79}{\epsilon_{in}}\right) \frac{q^2}{2\pi\epsilon_0 D} \tag{4.7}$$

The energy difference has to be overcome, when a second carrier is to be injected in the Si NC. Σ and U are of substantial magnitude as shown in Fig. 4.2(b).

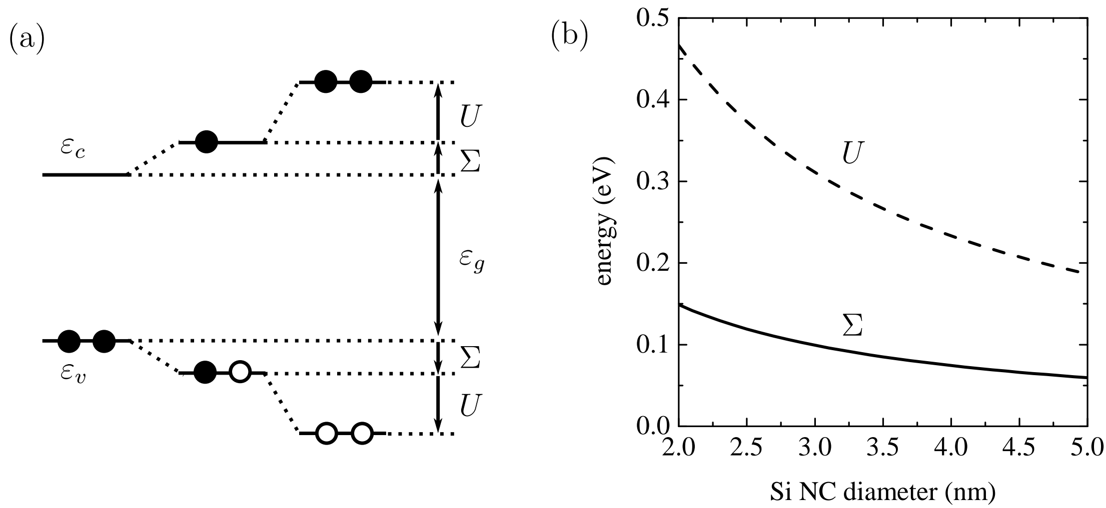

Figure 4.2: (a) schematic representation of the band edge shift as a result of Si NC charging with electrons or holes (reproduced from [135]); (b) plot of the self-energy and coulomb charging energy after eqn. 4.6 and eqn. 4.7 respectively

It has to be noted that the above considerations hold for isolated Si NCs. In a dense ensemble of Si NCs, the close vicinity of other Si NC will lead to an increase of ϵ_{out} in the framework of an effective medium approximation. Therefore, eqn. 4.6 and eqn. 4.7 should be considered as upper limits.

4.1.3 Configuration Coordinate Diagram

The use of a configuration coordinate diagram is a widely used concept in order to study electronic transitions involving electron-lattice interaction [135, 140]. The total electronic energy of a system is drawn as a function of a single generalized lattice coordinate Q for initial and final states. Around the energy minima, these potential energy curves can be approximated by a parabola as shown in Fig. 4.3. According to the Franck-Condon principle [141, 142], electronic transitions between

different potential energy surfaces are only allowed in vertical direction, because they are inherently faster than any displacement of atoms.

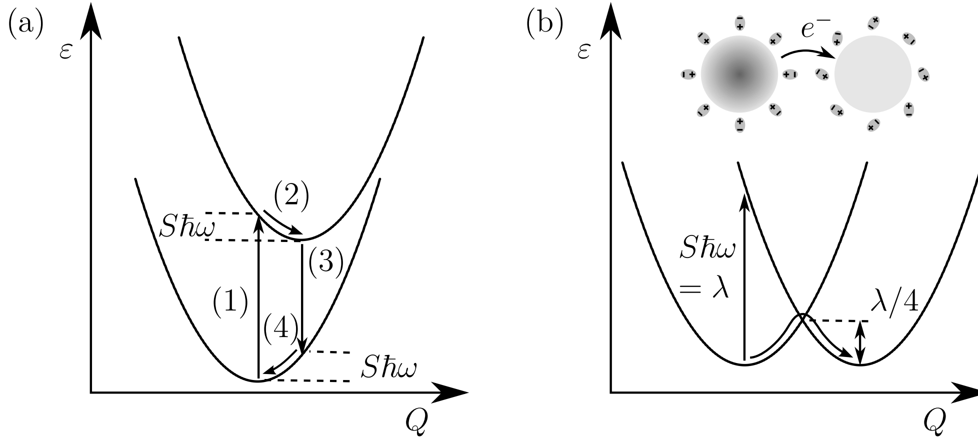

Figure 4.3: configuration coordinate diagrams of a photon absorption/emission process (a) and polaron hopping (b) (inset: illustration of polaron hopping between two Si NCs). See text for further explanation.

For instance, a photon absorption and emission cycle is drawn in Fig. 4.3(a). Following the absorption (1), the electron relaxes to the new energy minimum (2) by emission of S phonons with energy $\hbar\omega$. S is the Huang-Rhys factor that determines the strength of the electron-lattice coupling and ω is a characteristic phonon frequency. The emission process through (3) and (4) to get back to the inital state is analogous.

It is possible to draw the configuration diagram for an electron that hops from one Si NC to another one of the same size (Fig. 4.3(b)). Thus the potential minima are equal, but displaced in Q, because of the change in polarization around the two Si NCs accompanied by the transition (cf. inset of Fig. 4.3(b)). The transition between two potential curves can occur by absorption of a photon with energy $S\hbar\omega = \lambda$ or photon-free at the crossing point of the two potential curves as indicated by the arrows in Fig. 4.3(b). In the latter case, the electron faces a barrier of $\lambda/4$ which physically represents a polaron hopping energy [143, 144], i.e. the energy that is needed to polarize the environment (i.e. the SiO_2-matrix) while the electron is moving.

4.1.4 Fermi's Golden Rule and Marcus Equation

Generally, the electron transfer rate Γ_{12} between the two adjacent Si NCs can be calculated by applying Fermi's golden rule [145] and summing over all possible transitions between initial and final states [146]:

$$\Gamma_{12} = \frac{2\pi}{\hbar} \sum_{i,f} p_i \left| M_{if} \right|^2 \delta \left(\varepsilon_i - \varepsilon_f \right) \tag{4.8}$$

In eqn. 4.8, the δ-function ensures energy conservation of the transition, p_i is the probability of the electron to be in initial state i and M_{if} is the matrix element that determines the strength of the transition between the initial and final state. It is important to note that in eqn. 4.8 vibrational and electronic states have to be considered. Following the Born-Oppenheimer approximation [147], one now usually separates the total wavefunction in its vibrational and electronic part and only considers transitions at the crossing point of the potential curves between the two Si NCs. Provided the electronic coupling is much smaller than kT and only a single phonon frequency is taken into account, this approximation yields in the high temperature limit, i.e. $kT >> \hbar\omega$ [143, 148–151] :

$$\Gamma_{12} = \frac{2\pi}{\hbar} \left| H_{12} \right|^2 \frac{1}{\sqrt{4\pi S\hbar\omega kT}} \exp\left(-\frac{\left(S\hbar\omega - \Delta\varepsilon \right)^2}{4S\hbar\omega kT} \right) \tag{4.9}$$

Here, H_{12} denotes the electronic coupling element between the initial and final electronic states of the two Si NCs and $\Delta\varepsilon$ is the energy difference between initial and final electronic state. This equation is mathematically equivalent to the Marcus equation for the electron transfer rate in reactions [152–156], if $S\hbar\omega$ is replaced by the reorganization energy λ as was already introduced in Fig. 4.3(b). The electron-phonon coupling essentially broadens the electronic transition. In addition, the electron transfer faces an activation energy barrier of:

$$E_a = \frac{\left(\lambda - \Delta\varepsilon \right)^2}{4\lambda} \tag{4.10}$$

In fact, the exponential term in eqn. 4.9 can be readily deduced from the configuration coordinate diagram. In case of $\Delta\varepsilon = 0$, there is a barrier of $E_a = \lambda/4$ that has to be overcome for the transition. The activation energy vanishes if the

energy gain for the transition matches the dielectric losses. For the case, where $\Delta\varepsilon$ exceeds the reorganization energy, the activation energy increases again which is called the Marcus inverted region, whose existence has been proven for electron transfer reactions. However, one may not expect the inverted region for quantum dots, since in that case transitions to electronic states of higher energy would occur preferentially (cf. eqn. 4.8).

4.1.5 Reorganization Energy

When eqn. 4.9 is derived from the viewpoint of semiconductor physics, the quantity $S\hbar\omega$ often refers to the electron lattice coupling via acoustical phonons at point defects and the effect of the dielectric environment is not included. In fact, as shown in sec. 4.1.2, the dielectric effect on the electron energy can be accounted for by applying the self-energy correction to the ground state energy (cf. eqn. 4.6).

How does the self-energy Σ of charging a single Si NC relate to the reorganization energy λ for electron transfer between two Si NCs? In fact the answer can be traced back to the beginnings of electron transfer theory in biology and chemistry, where the reorganization energy λ is thought of to be the sum of an inner reorganization energy λ_{in} and an outer reorganization energy λ_{out}. While the former is related to structural changes induced by acoustic phonons, the latter describes the electrostatic coupling to the surrounding matrix by optical phonons. In Si NCs the inner reorganization energy is quite low. In case of excitonic excitations of Si NCs, λ_{in} is on the order of a few meVs for the size range studied here [157] and hence neglible.

More importantly, the outer reorganization energy was derived from dielectric continuum theory for the case of two conducting spheres embedded in a dielectric medium [152, 158, 159]:

$$\lambda \approx \lambda_{out} = \frac{q^2}{4\pi\epsilon_0}\left(\frac{1}{n^2} - \frac{1}{\epsilon_{out}}\right) \cdot \left(\frac{1}{D_1} + \frac{1}{D_2} - \frac{1}{D_1/2 + D_2/2 + s}\right) \tag{4.11}$$

where n is the matrix refractive index and s is the separation distance between the two Si NCs. The last term of eqn. 4.11 in brackets only relates to the geometry of the double sphere system. It suggests that λ is composed of three parts. One part that only depends on D_1 and another one only on D_2. Finally, a part depending on D_1, D_2 and s is subtracted, but vanishes for $s \to \infty$. Hence, the suggested physical

interpretation is that λ is the sum of the self-energies of each dot minus one part that comes from polarization overlap between the two dots when they are brought close together. Interestingly, replacing $1/D_1$ in eqn. 4.6 by the same geometry factor from eqn. 4.11 gives identical results with a constant deviation below 1%.

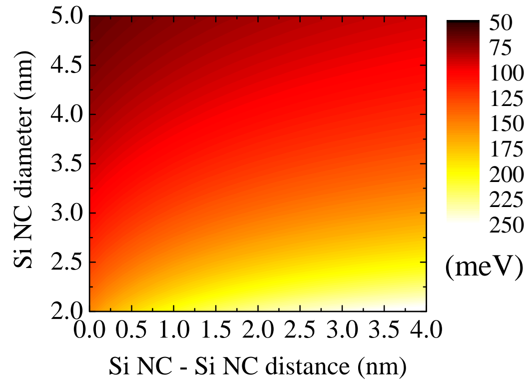

Figure 4.4: Visualization of the reorganization energy λ as calculated from eqn. 4.11 with $\varepsilon_{in} = 11.7$ and $\varepsilon_{out} = 3.9$

In Fig. 4.4, λ is plotted for two Si NCs of equal size with varying distance. As can be seen, the reorganization energy is substantial for all cases and more pronounced for smaller Si NCs and larger separation due to the increased induced polarization changes. Similar arguments hold here as discussed already for the charging energy. The calculated values represent again an upper limit and are likely to be reduced in dense ensembles of Si NCs.

4.1.6 Electronic Coupling between two Si Nanocrystals

The electron transfer rate is directly proportional to the square of the electronic coupling matrix element H_{12} which is defined as the integral overlap between the initial wavefunction in the first Si NC ψ_1 and final state wavefunction ψ_2 in the second Si NC [160]:

$$H_{12} = \int_V \psi_1 \mathcal{H}_2 \psi_2 \mathrm{d}V \tag{4.12}$$

Here, $\mathcal{H}_2$ is the pertubation that causes the electron to transfer to the second Si NC, i.e. the potential of the second Si NC. As shown in sec. 4.1.1, the confinement energy

is directly related to the effective mass in the Si NC. Even though the concept of effective masses is known to be questionable in case of Si nanostructures, it is used here to study the effect of electronic coupling. The confinement energy can be adjusted by tuning the electron effective mass in the Si NC. In this way analytical wavefunctions can be obtained that satisfy the Schrödinger equation for any Si NC diameter and confinement energy.

While this approach may not be physically justified, it appears to yield more physically reasonable results than first principles calculations [161, 162]. The reason is simply that these calculations underestimate the bandgap drastically. As a result the conduction band-offset between Si and SiO_2 is reduced as compared to the realistic case. This will have a dramatic impact on the calculated electronic coupling, because the wave function damping in the matrix is significantly reduced. Given the above assumption, the electronic coupling can be calculated by numeric evaluation of eqn. 4.12. All calculations in the following have been carried out in three dimensions using Matlab and a grid resolution of 0.1 nm. This was sufficient to achieve a numerical accuracy of $< 2\%$.

Fig. 4.5 shows the corresponding calculations evaluated for different input parameters by using contour plots to vary two parameters at a time. First H_{12} is calculated for the two Si NCs in contact, i.e. $s = 0$ (Fig. 4.5(a)). For strong confinement energies and small sizes H_{12} can exceed 100 meV, whereas in case of more realistic values, it is decreased down to few meVs. This is substantiated in Fig. 4.5(c), where the electronic coupling of the lowest conduction band states as calculated from tight-binding (eqn. 4.1) is evaluated at contact distance for different donor and acceptor sizes. The results indicate that the interacting Si NC system may be considered decoupled for any arrangement and the use of a pertubation ansatz to calculate the electronic matrix element is justified.

In addition, the energy-distance dependence is evaluated (see Fig. 4.5(b)) and it can be seen that the damping strongly depends on the energy that is considered for the coupling. Fig. 4.5(d) displays the size and distance dependence of the electronic coupling again at energies according to tight-binding calculations. Clearly, the electronic coupling falls off steeply, when the distance between the Si NCs is increased. This directly reflects the exponential wave-function decrease within the matrix. An interesting side-note concerns the damping factor (i.e. the localization length) which is increased in the range of 5% to 20% as compared to the one-dimensional case.

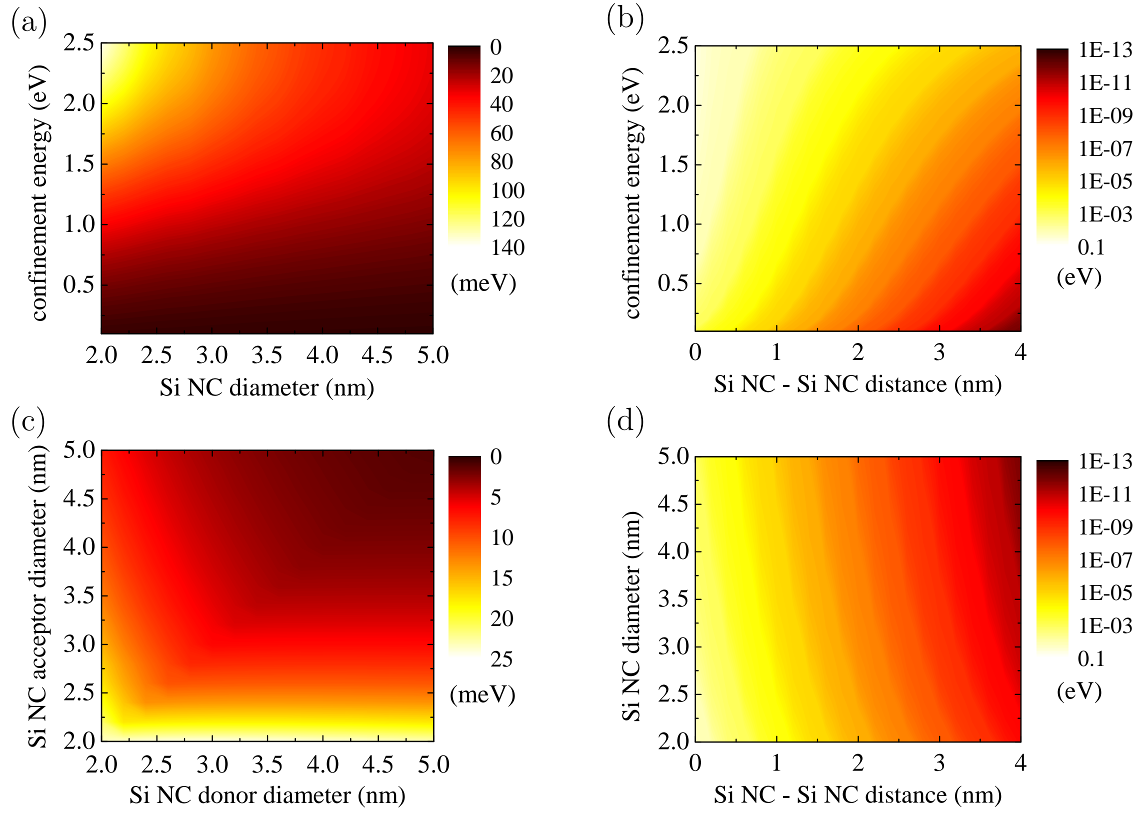

Figure 4.5: Electronic coupling matrix element H_{12} between two Si NCs as calculated from eqn. 4.12: (a) for touching and equally sized Si NCs, (b) equally sized ($d = 3.5$ nm), (c) touching and (d) non-touching Si NCs with the confinement energy calculated by eqn. 4.1 ($T = 300K$)

4.1.7 Electron Transfer Time between Silicon Nanocrystals

Knowing the reorganization energy and the electronic coupling, the electron transfer times $\tau_{12} = 1/\Gamma_{12}$ can be calculated by means of the Marcus equation (eqn. 4.9). Only transitions between the lowest conduction band states are considered and the rate is multiplied by 6 to account for the Si conduction band valley degeneracy. Taking full account of the Si NC density of states will thus result in slightly faster electron transfer times.

In Fig. 4.6(a), the transfer time is plotted for a variation of the Si NC diameter and separation distance. As already expected the transfer time spans several orders of magnitude as a function of distance, because of the strong damping of the electronic coupling that even enters quadraticly in the calculation. It is evident that in order to have ns electron transfer, the separation between the Si NCs has to be in the order of 1 nm. On the other hand, the electron practically remains within the first

Si NC, when the barrier distance is in excess of 3 nm underpinning the need for ultrathin barriers for efficient transport. Please note that in case of touching or nearly touching Si NCs, transfer times in the order of fs are obtained. In this case the physical picture of electron transfer is no longer useful because the electron wavefunction becomes strongly delocalized.

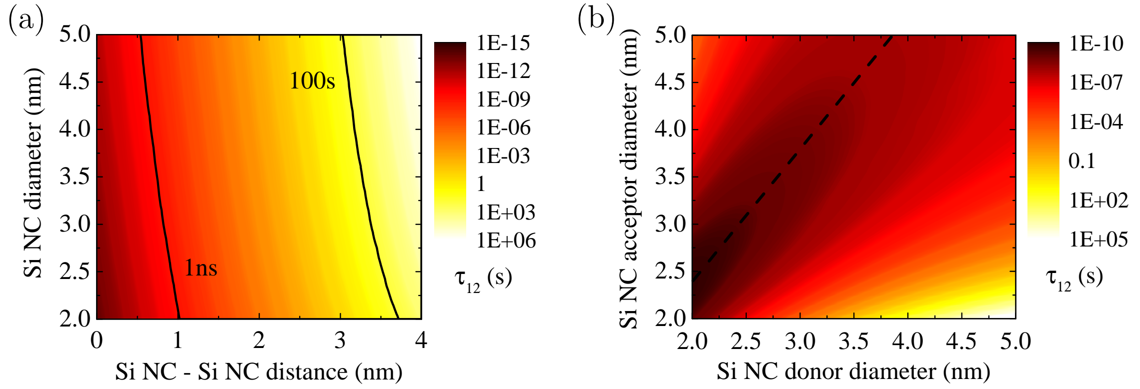

Figure 4.6: Electron transfer times between two Si NC of the same size vs diameter and distance (a) and for different donor and acceptor diameter with $s = 1$ nm (b) ($T = 300K$)

Next, the transfer between Si NCs of different sizes is considered (cf. Fig. 4.6(b)). In general, it is observed that electron transfer is fastest from a smaller Si NC to the energetically more favorable larger one. The dashed line indicates the minimal transfer time, where the required reorganization energy is compensated by the gain in kinetic energy due the energy difference between initial and final states. The values above the dashed line correspond strictly speaking to the Marcus inverted region and a transfer time decrease is observed. This may however not be observed in nanocrystalline systems, because in case of such a large energy difference, the electronic and vibrational coupling to higher energy states beyond the ground states will have to be considered.

4.1.8 The Effect of an Applied Electric Field

In the absence of an applied electric field $\mathcal{E}$, the electron transfer between two identical Si NCs is symmetric, i.e. forward and backward transfer rate are identical. The electron oscillates between the two Si NCs and the effective carrier velocity is neglible. In the presence of size disorder, the electron is thus trapped in a

local energy minimum. In any case, the carrier velocity is ≈ 0. The application of an electric field adds directionality for electron transfer. The average carrier velocity is then determined by the net jump rate in the direction of the electric field $v_z = \Delta z \cdot (\Gamma^+ - \Gamma^-)$. Γ^+ and Γ^- are given by the forward and backward transfer rate between the two Si NCs [163] which can be calculated by the Marcus equation (eqn. 4.9). Even with all the approximations made so far to calculate the transfer rates for the unbiased case, further approximations are needed to calculate the electric field dependence.

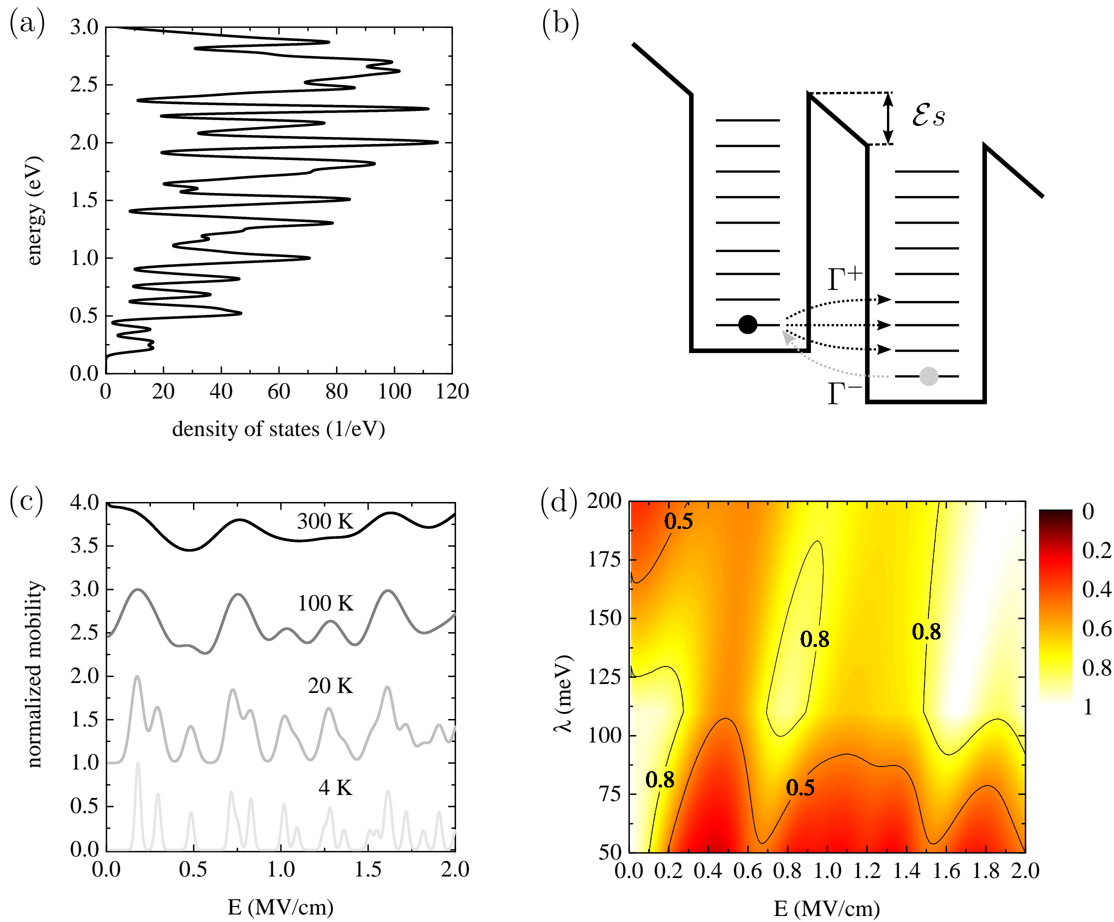

Figure 4.7: (a) density of states of a cubic Si NC with L =4.5 nm (eqn. 4.13) with a Gaussian broadening of 26 meV, (b) schematic of electron transfer between two Si NCs under an applied electric field, (c) normalized mobility for different temperatures with λ =100 meV (shifted by 1 for clarity), (d) normalized mobility contour plot for $T = 300K$

First of all, a complete description of the density of states of a Si NC is needed. Therefore, the effective mass approximation for a cubic Si NC with sidelength L

and infinite potential barriers is used [135]:

$$\varepsilon_{n_x,n_y,n_z} = \frac{\hbar^2\pi^2}{2L}\left(\frac{n_x^2}{m_l} + \frac{n_y^2}{m_t} + \frac{n_z^2}{m_t}\right) \tag{4.13}$$

$m_t = 0.19m_e$ and $m_l = 0.89m_e$ are the transversal and longitudinal effective masses of electrons in the Si conduction band valleys and n_x, n_y, n_z are integer quantum numbers ≥ 1. The calculated density of states is shown in Fig. 4.7(a) for L =4.5 nm.

When a homogeneous electric field as applied across the double quantum dot system embedded in the dielectric, the difference in dielectric constants will lead to surface polarization effects that effectively screen the electric field from the interior of the quantum dot, when $\epsilon_{in} > \epsilon_{out}$ as it is found in the present case. An exact solution of the Laplace equation governing the electrostatic potential is only possible for this double dielectric sphere system in terms of a recursive set of complex equations in bispherical coordinates [164, 165]. Therefore, it is assumed now that all the potential drops across the SiO_2 barrier and only the one-dimensional case is considered (cf. Fig. 4.7(b)). The approximation implies that the inner part of the Si NC wavefunction is not affected significantly.

In addition, transitions to all possible final states have to be considered, but their wavefunction has to be assumed to be s-like. Hence the electronic matrix element H_{12} is only affected by the increased transmission probability through the triangular barrier (Fig. 4.7(b)). The effect is modelled by applying the Wentzels-Kramers-Brillouin approximation for the transmission coefficient TC [166]:

$$TC(\mathcal{E}) = \exp\left(-\frac{2}{\hbar}\int_0^s \sqrt{2m_{ox}(V_0 - \mathcal{E}z - \varepsilon)}\mathrm{d}z\right) \tag{4.14}$$

The electric field dependence of H_{12} is then approximated by:

$$H_{12}(\mathcal{E}) = H_{12}(\mathcal{E} = 0)TC(\mathcal{E})/\lim_{\mathcal{E}\to 0} TC(\mathcal{E}) \tag{4.15}$$

In fact, we are interested in the hopping mobility:

$$\mu_{hop}(\mathcal{E}) = v_z(\mathcal{E})/\mathcal{E} \tag{4.16}$$

which can now be calculated using the approximations explained above.

In Fig. 4.7(c) the mobility is calculated for four different temperatures from 4 K up to 300 K. The distinct mobility peaks visible at low temperature continuously evolve into broad bands at 300 K such that the mobility is constant to within a small factor. However, it is an important finding that there is no pronounced electric field dependence of the mobility.

The mobility may also be strongly affected by the value of the reorganization energy λ, because it directly influences the activation barrier for tunneling. In Fig. 4.7(d), it can be seen that the net effect of λ on the normalized mobility is in fact rather small. Therefore, the effect of λ on the mobility can be easily evaluated by calculating the unbiased electron transfer rates.

A final remark concerns the presence of energy disorder, in particular an energy barrier in the direction of transport. In that case, the mobility is almost neglible until the potential drop across the barrier compensates for the energy difference. An exponential increase of the carrier mobility is thus observed in the transition region.

4.1.9 Interface Defects

Up to now, only well passivated, defect-free Si NCs were considered. However, the amount of Si/SiO_2 interface defects is significant even for well passivated samples [69, 77] and ultimately limit the PL quantum efficiency [56, 57]. A volume density of approximately 1×10^{17} interface defects per cm^3 can be estimated for the samples studied in this work [167]. This value is clearly in the range of common semiconductor dopant concentrations.

The most established Si/SiO_2 interface defect is the paramagnetic P_b defect. This dangling bond (DB) is energetically centered between the Si conduction and valence band and is occupied by one electron in the neutral case. The amphoteric nature of the P_b center allows for three distinct charge states within the Si bandgap. For the bulk interface case, the $\varepsilon(2, 1)$ charge transition level is located at 0.25 eV below the conduction band, whereas the $\varepsilon(1, 0)$ charge transition level is located at 0.3 eV above the valence band [168–170]. Moreover, pure electrostatic arguments lead to the conclusion that the defect energy levels closely follow the band edge shifts imposed by quantum confinement [135]. The whole situation is summarized in Fig. 4.8.

The electronic nature of the Si DBs suggests that they act primarily as carrier trapping sites. Electronic transitions involving a DB exhibit a strong

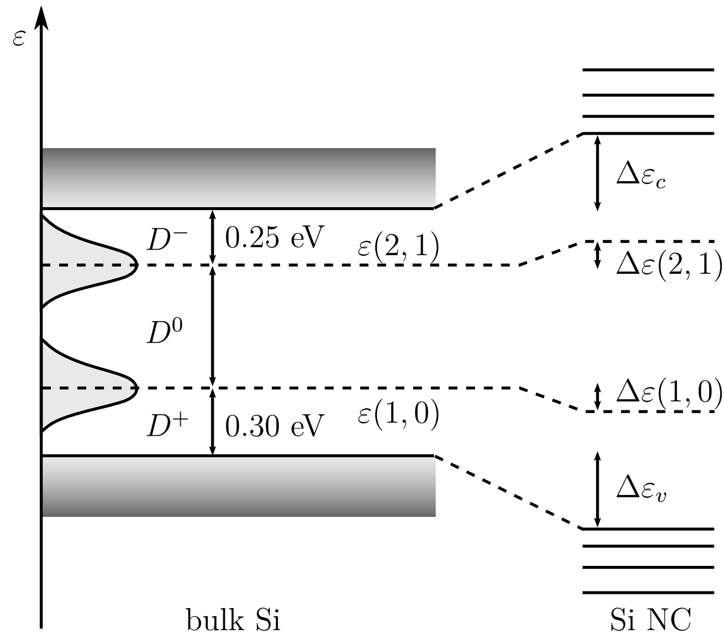

Figure 4.8: Energy representation of the Si surface DB (reproduced from [135]), $\varepsilon(1,0)$ and $\varepsilon(2,1)$ denote the charge transition levels, ε_c and ε_v are the Si conduction and valence band edges, respectively

electron-phonon coupling which renders the calculation challenging. The inner reorganization energy amounts to about 300 meV [135] which has to be added to the value of reorganization energy λ. Hence, it can be qualitatively argued from eqn. 4.10 that such transitions face a substantial energy barrier, but are also significantly broadened.

4.2 Macroscopic Transport

In the previous section, the microscopic details of electron transfer have been described in detail. However, in order to benchmark any nanoscale composite material, macroscopic properties such as the carrier density and mobility have to be determined from the electrical characterization. In the following, limiting cases of the J-E characteristics of Si NC/SiO_2 SLs are derived.

Consider the SL as a black (semiconducting) box with idealized ohmic contacts. Then Ohm's law holds in the form of a drift-diffusion model. Neglecting for simplicity

the diffusion term, it is given by [171]:

$$J = \sigma \mathcal{E} = q n_f(z) \mu \mathcal{E}(z) = const \tag{4.17}$$

where σ is the conductivity, n_f is the volume density of free carriers that are available for transport and μ is their mobility. At this point, it has to be realized, that Si NC/SiO_2 SLs contain only a very small number of carriers available for transport as the Si NCs are nominally undoped. The intrinsic carrier concentration in bulk Si is about $3 \cdot 10^{10} cm^{-3}$ at room temperature and one may expect a further reduced density due to quantum confinement and the reduced volume fraction occupied by Si within the SL. For this reason the majority of conduction electrons has to be injected from the contacts. As a result the SL will charge up, the electric field distribution within the SL is no longer uniform [172] and the current is affected by the resulting space charge [173, 174]. The local potential $\Phi(z)$ and the electric field are related by the Poisson equation [171]:

$$-\frac{\partial \Phi(z)}{\partial z^2} = \frac{\partial \mathcal{E}(z)}{\partial z} = \frac{q n_i(z)}{\epsilon_0 \epsilon_r} = q \frac{n_f(z) + n_t(z)}{\epsilon_0 \epsilon_r} \tag{4.18}$$

where $n_i(z)$ is the total injected charge carrier density that is the sum of the free carrier density n_f and the trapped carrier density n_t. As argued in sec. 4.1.9 the influence of DBs must be included in the analysis in the form of trapping sites, formally represented here as n_t. In order to calculate the J-E characteristics, a general relationship between n_f and n_t must be established.

After Lampert [175], this can be done if the carriers are assumed to be in quasi-equilibrium, i.e. their occupation is given by Fermi distributions for trap occupation and Maxwell-Boltzmann statistics for electrons in the conduction band. Using appropriate boundary conditions, it is then possible to obtain an analytical solution of the coupled equations (eqn. 4.17 and eqn. 4.18) for the specific case of a discrete trap level at energy ε_T below the conduction band [175]. The rather complex results were later simplified by Muller [176], but still capture the essential physics:

$$J = \sigma_0 \mathcal{E} \left(\frac{\mathcal{E}}{\mathcal{E}_0} - 1 + \sqrt{\left(\frac{\mathcal{E}}{\mathcal{E}_0} - 1 \right) + \frac{4 \mathcal{E} \theta}{\mathcal{E}_0}} \right) \tag{4.19}$$

with

$$\theta = \frac{N_C}{N_T} \exp\left(-\frac{\varepsilon_T}{kT}\right) \tag{4.20}$$

$$\sigma_0 = \frac{q\mu\alpha N_T}{2} \tag{4.21}$$

$$\mathcal{E}_0 = \frac{q d_{ox} N_T}{\epsilon_r \epsilon_0 \alpha\beta} \tag{4.22}$$

$$\text{with} \quad 1 < \alpha < 2 \tag{4.23}$$

$$1/2 < \beta < 1 \tag{4.24}$$

N_C is the volume density of states near the conduction band edge, N_T is the volume trap density and α and β are constants, where only the limits are known. Two limiting cases can be derived from eqn. 4.19 (known as the Mott-Gurney law of space-charge limited current) that differ just by a prefactor θ:

$$J = \begin{cases} \theta\mu\epsilon_0\epsilon_r\alpha^2\beta\mathcal{E}_\Omega^2/d_{ox} & \text{if } \mathcal{E} << \mathcal{E}_0 \\ \mu\epsilon_0\epsilon_r\alpha^2\beta\mathcal{E}_\Omega^2/d_{ox} & \text{if } \mathcal{E} >> \mathcal{E}_0 \end{cases} \tag{4.25}$$

Here, $\mathcal{E}_\Omega = V/d_{ox}$ denotes the electric field in the absence of any space-charge, i.e. the Ohmic electric field. As shown in Fig. 4.9, the current rises steeply by orders of magnitude between the two limiting cases when $\mathcal{E}_\Omega \approx \mathcal{E}_0$, marking the transition from a trap dominated region to a region, where the traps are filled and the majority of injected charges is free to contribute to the current.

The preceding considerations and limits are only valid if the mobility of the free carriers is field-independent and for low electric fields. In the presence of a high electric field, trapped electrons might be released to the conduction band meaning that the thermal equilibrium is disturbed. In addition free electrons gain energy from the electric field that is then dissipated to the heat bath by phonon emission [177, 178]. In fact, it has been proposed that the effect of an intense electric field can be included in transport and hopping calculations by changing the effective lattice

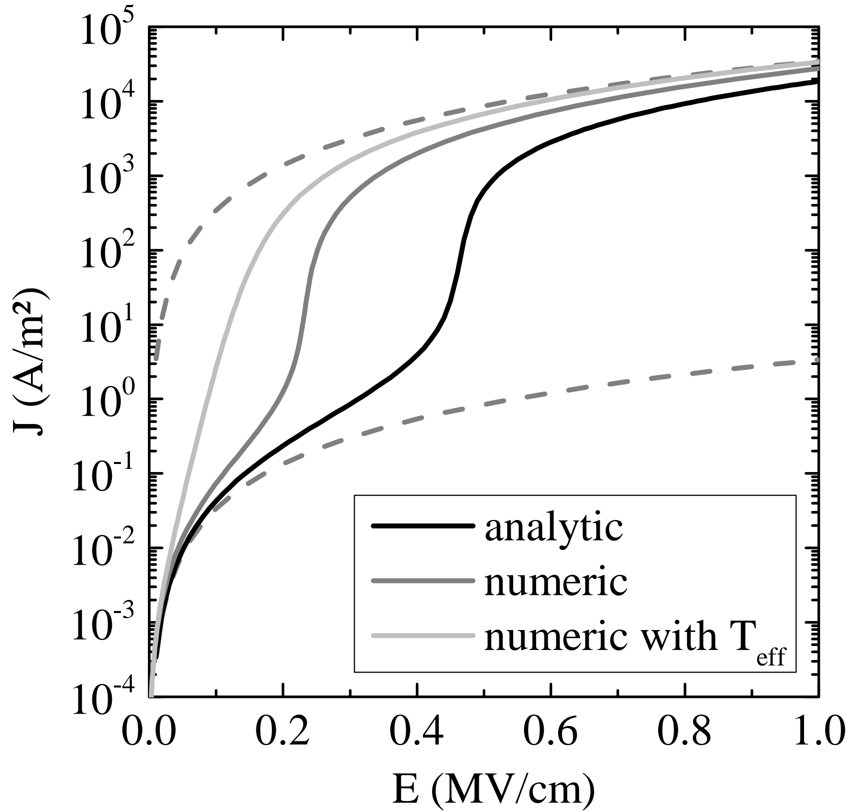

Figure 4.9: Plot of eqn. 4.19 (solid black line) and the two limiting case of eqn. 4.25 (dashed lines) with the parameters $\mu = 1 \cdot 10^{-4}$ cm^2/Vs, $N_T = 1 \cdot 10^{17}$ cm^{-3}, $N_C = 1 \cdot 10^{18}$ cm^{-3}, $\varepsilon_T = 0.3$ eV, $d_{ox} = 100$ nm, $\alpha = 1$ and $\beta = 1$. The numeric simulation were carried out with the same parameters and $\Delta z = 4.5$ nm.

temperature [179, 180]:

$$T_{eff} = \sqrt{T^2 + (0.67 q \mathcal{E} \Delta z / k_B)^2} \tag{4.26}$$

Indeed, the effective temperature concept could well explain some features in the transport characteristics of hydrogenated amorphous Si [181, 182] and is hence worth applying to the present problem. Therefore, a numerical routine is employed in order to calculate the space-charge limited current (SCLC) (cf. sec. A.2 for a detailed description of the calculation).

The results of the numerical simulation are also shown in Fig. 4.9. In the exact numerical solution, the transition from the trap-controlled to the trap-free current density is shifted to lower electric fields which is probably related to the choice of the

α parameter (cf. eqn. 4.22) in the analytical approximation (eqn. 4.19). When the influence of the electric field is included by using the effective temperature principle (eqn. 4.26), the current density rises directly from the trap-limited regime to the trap-free curve.

It was demonstrated that the transport measurements in dark are inherently associated with charge build-up within the SL. Therefore, it is interesting to check the maximum amount of charge Q_{NC} that is stored on a Si NC as a function of $\mathcal{E}_\Omega$. The maximum charge that can be stored in the SL as required by Gauss law is $\overline{C}V = \overline{Q}$. In this limit, one obtains:

$$Q_{NC} = \frac{\epsilon_0 \epsilon_r \mathcal{E}_\Omega}{q A_{NC} n_{bl}} \tag{4.27}$$

where A_{NC} is the areal Si NC density per layer and n_{bl} is the number of bilayers in the sample. Using the areal Si NC density from plane view EF-TEM measurements (sec. 3.2), electric fields in excess of 3 MV/cm are needed to have on average one electron per Si NC for the thinnest samples studied in this work. Increasing n_{bl} also increases this threshold electric field. Given the assumption that the charge is spread homogeneously within the SL, it can be concluded that coulomb charging of individual Si NCs plays a minor role in the transport characteristics.

In summary the following conclusions can be drawn based on the preliminary considerations for carrier transport in Si NC/SiO_2 SLs:

- the current is limited by the injected space charge
- defects on the surface of the Si NCs will act as trapping sites at low electric fields, thus greatly reducing the number of available free carriers
- at larger electric fields, all traps are filled and consequently the number of free carriers is increased dramatically giving rise to a strong current enhancement
- the J-E curve spans orders of magnitude which is related to the number of carriers available for transport in the presence of trapping sites

4.3 Electrical Measurements

4.3.1 Space-Charge Effects

In the first set of samples, the total number of SL bilayers is varied as shown in Tab. 4.1. This variation is interesting, because according to eqn. 4.25 the current density should scale as $1/d_{ox}$ in the expected SCLC regime.

Table 4.1: List of sample set N, where the number of bilayers is changed from 5 to 30. Sample N3 was also measured by TEM in sec. 3.3.

name	SL structure	d_{nom} (nm)
N1=B1.3	5×(1nm SiO_2/3.5nm $SiO_{0.93}$)	22.5
N2	10×(1nm SiO_2/3.5nm $SiO_{0.93}$)	45.0
N3*	20×(1nm SiO_2/3.5nm $SiO_{0.93}$)	90.0
N4	30×(1nm SiO_2/3.5nm $SiO_{0.93}$)	135.0

The J-E characteristics are shown in Fig. 4.10(a). The first general observation is that the J varies by eight orders magnitude over the whole investigated electric field range. As shown in sec. 4.2, it is well explained by a SCLC in the presence of carrier trapping sites. Although, it is not easily distinguished between point defects and energetic disorder imposed by a variation of Si NC size and shape, the observed J-E dependence is in fact quite universal for all samples under investigation.

The trapping characteristics measured by means of a C-V flatband voltage shift is shown in Fig. 4.10(b). Clearly, electron trapping dominates at lower electric fields up to 1 MV/cm for all samples – a strong indication of SCLC.

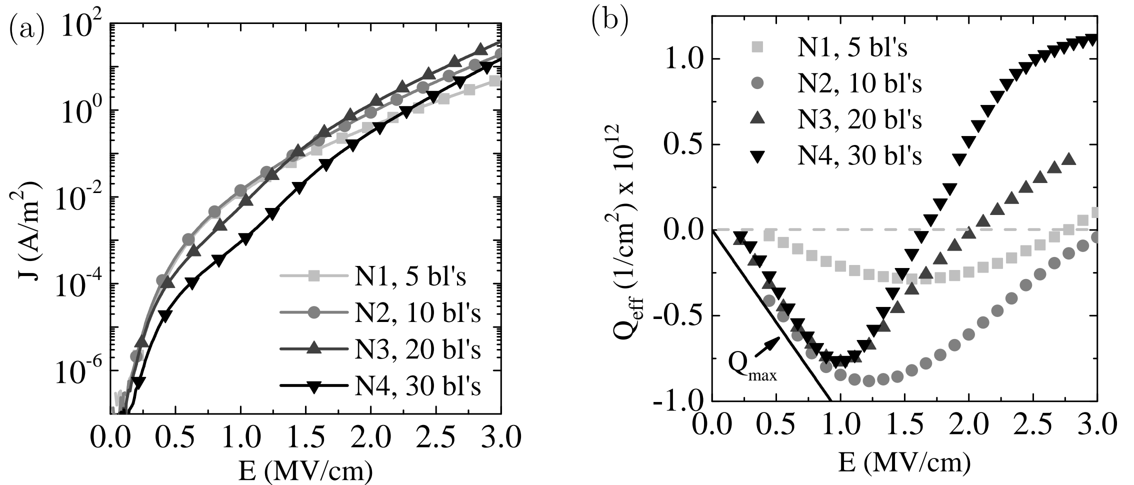

Figure 4.10: Current density (a) and charge trapping (b) measured for sample series N described in Tab. 4.1. The solid line in (b) represents the maximum charge density that can be stored in the samples.

Based on the assumption that the charge is uniformly distributed within the SL, the effective areal charge Q_{max} that would be measured using the C-V trapping technique would amount to:

$$Q_{max} = \frac{\epsilon\epsilon_0\mathcal{E}}{2q} \tag{4.28}$$

As can be seen in Fig. 4.10(b), the injected charge Q_{eff} follows Q_{max} closely for all samples except for sample N1, where the charging is reduced strongly. The reason for the latter might be the extreme thinness of the sample leading to discharging that is much faster than it is possible to measure the flatband voltage. At lower electric fields, the strong electron injection from the Si substrate leads to a reduced current density for increasing the number of bilayers (Fig. 4.10(a)), although it must be noted that the J is not linearly dependent on $1/d_{ox}$. Instead it follows roughly a $1/d_{ox}^l$ dependence with $l \approx 1.75$. A similar dependence was found already for different Si NC films [183, 184] and interpreted in terms of SCLC in the presence of an exponential distribution of trap states [173, 174]. It may therefore reflect to some extent the energetic disorder in the sample. The contact ideality, a silent prerequisit of all SCLC modelling approaches [171], is difficult to assess solely on the basis of room temperature electrical measurements. However, it can be concluded that the contacts are nearly ideal with respect to the SL at lower electric fields due to the fact that the maximum possible charge is almost attained (cf. Fig. 4.10(b)).

At higher electric field in excess of 1 MV/cm J appears enhanced as the number of bilayers is increased, when compared to the lower electric field regime (Fig. 4.10(a)). This pronounced rise in J is accompanied by a concomitant decrease of the measured injected electron charge density (Fig. 4.10(b)). For 20 and 30 bilayers, the effective net charge even turns positive at electric fields exceeding 1.5 MV/cm. As further measurements will show later, this particularity is an intrinsic feature of all Si NC/SiO_2 SLs.

Before discussing the origin of this unexpected charging behaviour, the transient trapping and detrapping characteristics are analyzed. Fig. 4.11(a) shows the current transients in response to the application of step voltages to a virgin device of sample N4 with 30 bilayers. In the lower electric field and electron trapping regime, J continuously decreases with time indicating that the steady state is only reached after a very long time. In contrast, when the electric field is in the range of 1 MV/cm, a minimum appears in the transients that shifts to shorter times, when the electric field is increased. Finally the minimum cannot be resolved with the time resolution

of the measurement system and the current rises steadily until it saturates. The transient curves reflect the time-dependence of the effectively trapped charge in the samples. The increasing current at higher electric fields indicates that the sample is in a self-biasing regime which is not consistent with a SCLC, but is in qualitative agreement with the measurements reported in Fig. 4.10.

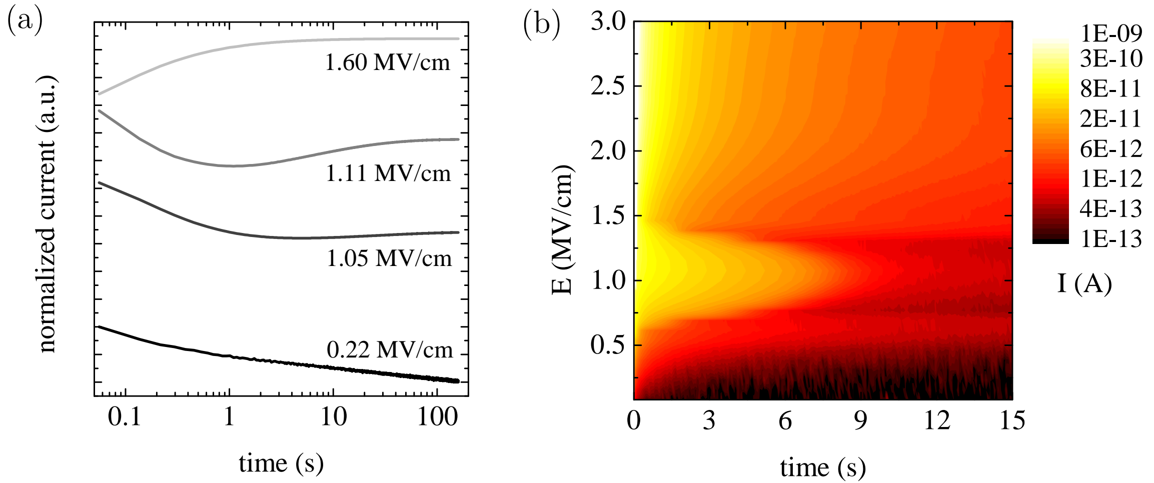

Figure 4.11: Current transients of sample N4 (30 bilayers): (a) Charging transients measured at indicated electric field strengths for virgin devices. The transients are normalized to [0;1] and shifted for clarity. (b) Electric field and temporal current discharge map measured at $V = 0$ after applying a step voltage pulse of 60 s. The step voltage is ramped up continuously.

In Fig. 4.11(b), the discharging current map of the same device is shown. The current is decreasing with time, but again it is observed that the transient times are long. In fact, it takes a very long time to restore the unbiased equilibrium situation that can hardly be achieved at room temperature. The current decay follows a power law $I(t) \propto t^{-\alpha}$ according to the Curie-von Schweidler law of dielectric relaxation [51–54]. For electric fields below 0.5 MV/cm α is increasing up to around 0.7, whereas it exceeds 1 at electric fields exceeding 1.5 MV/cm saturating at $\approx$1.3 for the highest electric fields. There exists some correlation between α and the total amount of charge stored in the SL. The more charge is stored, the higher is the dispersion of time constants and consequently the dispersion parameter α. Strong relaxation occurs also at the point, where no net charge is measured (compare Fig. 4.10(b) with Fig. 4.11(b)). This indicates that substantial amounts of positive and negative charges coexist in the SL. However, excitons in these SLs recombine on a μs timescale [57]. Therefore one has to conclude that these opposite charges cannot be spatially

correlated, if they originate from electrons and holes. From that, it follows directly that the holes are generated in the bulk of the sample, whereas the injected charge sheet is rather non-uniform.

Furthermore, please note that the comparably slow relaxation in the intermediate electric field range from 0.5 to 1.5 MV/cm in Fig. 4.11 is an artifact resulting from non-equilibrium processes in the n-type Si substrate. It is caused by a transient minority carrier generation current which is typical for semiconductors that are pulsed instantly into deep depletion [55]. It occurs here, because the electron charging at the initial bias induces a large positive flatband shift. As a consequence, the n-type substrate is largely depleted of majority carriers, when the bias voltage is switched back to 0 to monitor the discharging transient.

An open question concerns the origin of the positive charge at electric fields exceeding 1 MV/cm. We start by considering positively charged ions. From Fig. 4.10, we estimate the total positive areal charge density to be at least 2×10^{12} cm^{-2} for sample N4 which is less than 1% of a monolayer of Si surface atoms. Distributed within the SL volume, we find a minimum volume density of about 1.5×10^{17} cm^{-3} ions which corresponds to quite a low number of impurities. A single reference SiO_2 does not show any significant mobile charge effects up to high electric fields at 6 MV/cm. Therefore, incorporation of impurities by any post-deposition processes can be excluded. Additionally, it indicates that the positive charges are linked with the presence of the SRON layer. Hence, any positive ion consisting of Si, O, N and H and combinations thereof are possible candidates.

Another possibility is that the positive charges originate from holes. First of all, it has to be stated that these holes cannot be injected at the Al metal top contact of the device. The reason is that the hole tunneling probability is about 1000 times smaller than the electron tunneling probability [185] making it highly unlikely that injected holes can exceed the numbers of electrons. Therefore, the holes have to be generated in the bulk of the sample, a hypothesis supported by the transient current measurements explained above. It is furthermore very reasonable to argue that these holes are not thermally generated as it was concluded from earlier studies [186], because the intrinsic carrier density in bulk Si is only on the order of 1×10^{10} cm^{-3}. A smaller intrinsic carrier density is expected for the present films since the fractional volume of Si is strongly reduced and the energy bands are separated further due to quantum confinement. Previously band-to-band tunneling was proposed as the origin of the holes [187]. Here, a valence electron is expected to tunnel to the

conduction band in the presence of a high electric field. On the basis of the results so far, this mechanism cannot be completely excluded. However, first signs of hole generation are found at around 1 MV/cm, i.e. at a potential drop of only about 0.45 V per bilayer. This seems quite low in comparison to the bandgap of Si at ≈1.1 eV that is even widened due to quantum confinement.

Instead a similar mechanism shall be proposed here which is linked to the presence of Si surface DBs. As already reviewed in sec. 4.1.9, these DBs are amphoteric and energetically centered within the Si bandgap. Hence, ionization of this initially neutral DB may proceed at a sufficiently high electric field, leaving behind a positively charged DB. In fact, this may allow a valence electron to tunnel into this defect state, effectively creating an electron-hole pair in a two step process. The result is then similar to the band-to-band tunneling mechanism, but may set in at lower electric fields. While a pure band-to-band mechanism is difficult to prove experimentally, the defect density can be changed easily by passivation/depassivation treatments. Therefore, this possibility is investigated in the next section.

4.3.2 On the Role of Si Surface Defects

As mentioned in the previous chapter, it is promising to investigate the influence of Si surface defects. In addition, it was established in sec. 4.3.1 that the positive charge is somewhat linked to an intrinsic process within the SL. Therefore, it is desirable to disentangle the effect of charge injection at the contacts from the bulk contribution. This is achieved by preparing samples with carrier injection barriers at both top and bottom contact. For this purpose, a 10 nm SiO_2 layer is used, because electrons can only overcome this barrier by high electric field Fowler-Nordheim injection [188] that is absolutely neglible up to electric fields of 5 MV/cm. All samples investigated in this section are listed in Tab. 4.2.

The results of the electrical characterization of sample set H are shown in Fig. 4.12. We first look at the conducting samples indicated by the circles. An astonishing result is that the unpassivated samples with more DBs are more conductive than the passivated samples by almost two orders of magnitude throughout the whole electric field range (Fig. 4.12(a)), but also have a reduced effect on the effective charge trapping measurement (Fig. 4.12(b)). As we will see in the following sections, an increased conductivity is always linked to a decreased observation of charge trapping.

Table 4.2: List of sample series H that allows to investigate the influence of DBs on the J-E characteristics and to shed light on the occurence of positive charges at high electric fields.

name	SL structure (nm)	d_{nom} (nm)	H_2?
H1	$22\times(1\ SiO_2/3.5\ SiO_{0.93})$	99	yes
H2	$22\times(1\ SiO_2/3.5\ SiO_{0.93})$	99	no
H3	$10\ SiO_2 + 18\times(1\ SiO_2/3.5\ SiO_{0.93}) + 10\ SiO_2$	101	yes
H4	$10\ SiO_2 + 18\times(1\ SiO_2/3.5\ SiO_{0.93}) + 10\ SiO_2$	101	no

The reason is most likely that many injected charges have left the SL already by the time the C-V sweep is accomplished and hence do not contribute to the observed flatband voltage shift. Since holes are inherently less mobile than electrons [185], they might govern the flatband shift in specific cases even though their density is less than the electron density.

In order to understand the enhanced conductivity of the defect-rich sample, it is instructive to look at eqn. 4.25. Qualitatively, the current enhancement might thus be attributed to an increased free carrier mobility. The clarification of this issue is however beyond the feasibility within this work. It can only be speculated that the defects enhance the electronic coupling between the Si NC either directly by modifiying their electronic structure or by enhanced defect-assisted tunneling. Further investigations by means of electron spin resonance experiments might shed light on the detailed mechanism.

We now turn to the samples with current blocking layers, H3 and H4. Fig. 4.12(a) and (b) additionally show their J-E and trapping characteristics respectively. The current density of both samples is orders of magnitude reduced with respect to the conducting samples. At around 2.5 MV/cm there is a rapid current increase for both samples whose onset is slightly delayed for the passivated samples. The current below 2.5 MV/cm is transient and vanishes at long delay times as demonstrated in Fig. 4.12(c). This indicates that the current stems from internal charge transfer within the embedded SL that induces a current in the external circuit according to the Shockley-Ramo theorem [189–191]. At electric fields exceeding 2.5 MV/cm, J is no longer transient and therefore has to be attributed to Fowler-Nordheim injection across the SiO_2 tunneling barriers. The comparably low onset of Fowler-Nordheim

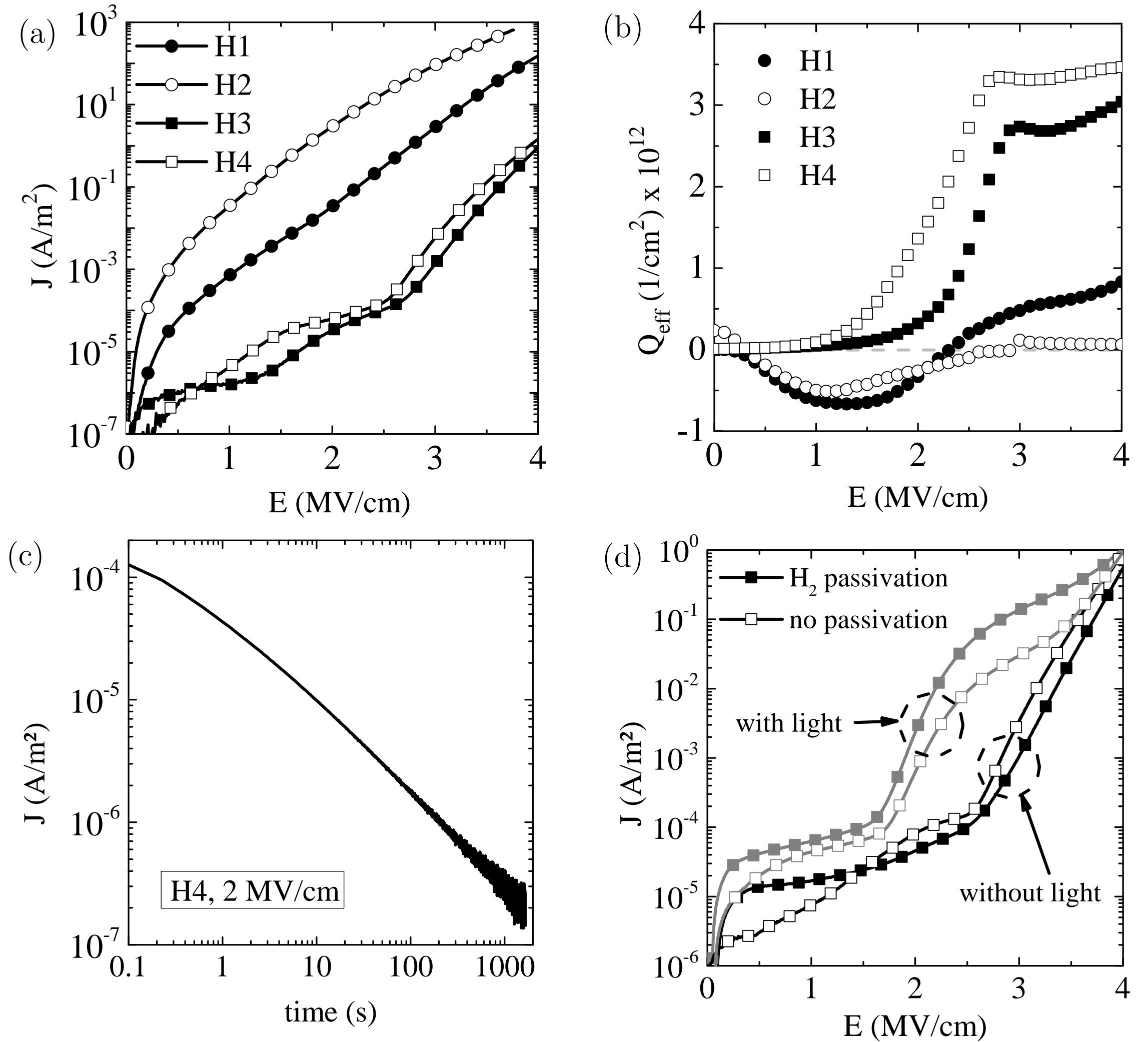

Figure 4.12: Electrical characterization of sample series H: (a) J-E characteristics, (b) Charge trapping characteristics, (c) transient of H4 at 2 MV/cm showing that the J essentially vanishes at long times and (d) J-E characteristics of devices with ITO instead of Al contact with and without microscope illumination. The conducting samples are indicated by circles, whereas the current blocking samples are denoted by squares. The H_2 passivation is indicated by filled symbols.

injection becomes clear, when the charging pattern in Fig. 4.12(b) is taken into consideration. The build-up of positive charge starts at around 1 MV/cm and quickly reaches a plateau region at around 2.5 MV/cm. Since the SL is neutral in the unbiased case and no net charge can be injected prior to the onset of a static continuous current across the device, a kind of charge separation has to occur within SL. Then, positive charges are forced towards the substrate, whereas negative charges are pushed towards the gate electrode. The separated charge is then

effectively canceling the potential applied between the gate and the substrate within the SL. As a consequence, most of the applied potential drops across the insulating current injection barriers. The effect is so strong that it facilitates a Fowler-Nordheim current at only 2.5 MV/cm. For comparison, a Fowler-Nordheim current is usually only observed at electric fields exceeding 5 MV/cm for the contact pad size employed here (cf. Fig. 4.13(a) in the next section). Once the Fowler-Nordheim current becomes dominant, the observed charge roughly saturates.

The important message from the measurements discussed so far is that the H_2 passivation reduces the positive charge accumulation. Hence, mobile ions can be possibly ruled out as the source of positive charge, provided that their presence and diffusivity are not altered by the H_2 passivation. In contrast, it implies that electron-hole pairs are indeed created within the embedded SL and that a clear correlation exists between the electron-hole pair creation and the existence of DBs.

A very impressive back-up of this hypothesis is exemplified in Fig. 4.12(d). Here, the Al contacts were replaced by transparent and conductive ITO contact pads for the current blocking devices H3 and H4. The dark J-E curves are very similar to the ones in Fig. 4.12(a). The ITO allows now to excite electron-hole pairs in the SL and measure the J-E characteristics at the same time. It is observed that the onset of the Fowler-Nordheim current is shifted by about 1 MV/cm to lower electric fields. This effect is now pronounced for the well passivated sample. It means that excitons are more efficiently separated by the electric field in the passivated sample as compared to the unpassivated one. In this case, defects are hampering exciton dissociation, because the non-radiative recombination at Si DBs is so much faster than the radiative defect-free recombination [169, 170]. At electric fields around 4 MV/cm, illuminated and dark J-E curves merge, indicating that the electron-hole pair generation via defects is again becoming the dominating mechanism. One may extrapolate the slope of the Fowler-Nordheim current under illumination towards the current sensitivity limit and obtains an applied electric field of around 1 MV/cm. Since the SiO_2 carrier injection barriers take up about 20% of the film thickness and the Fowler-Nordheim current starts to become measurable at 5 MV/cm, it can be concluded that the potential compensation due to the generated carriers within the SL is fairly ideal in this case.

4.3.3 Effect of the Silicon Oxide Barrier Thickness

It was demonstrated in sec. 4.1 that the electronic coupling between the Si NCs strongly depends on the SiO_2 barrier thickness. Hence it is certainly instructive to carry out measurements on samples with different nominal SiO_2 barrier thickness in order to observe how the microscopic electron transfer rate transfers to the ensemble of Si NCs. Here, two sets of samples are investigated. The first one consists of three samples with coarse barrier thickness variation that were also characterized by TEM presented in sec. 3.3. The second set comprises a finer SiO_2 barrier spacing variation and, in consideration of the TEM results, minimizes the bottom electrode injection barrier. All samples are described in detail in Tab. 4.3.

Table 4.3: List of two sample sets that investigate the effect of the SiO_2 barrier thickness. TEM images of the sample series B1 are shown and discussed in sec. 3.3. In sample set B2, the first SiO_2 barrier is held constant at 1 nm to assure nearly identical injection conditions.

name	SL structure	d_{nom} (nm)
B1.1*	5×(4 nm SiO_2/3.5 nm $SiO_{0.93}$)	37.5
B1.2*	5×(2 nm SiO_2/3.5 nm $SiO_{0.93}$)	27.5
B1.3*	5×(1 nm SiO_2/3.5 nm $SiO_{0.93}$)	22.5
B2.1	1 nm SiO_2 + 17.5×(3.5 nm $SiO_{0.93}$/0.6 nm SiO_2)	74.2
B2.2	1 nm SiO_2 + 17.5×(3.5 nm $SiO_{0.93}$/0.8 nm SiO_2)	77.6
B2.3	1 nm SiO_2 + 17.5×(3.5 nm $SiO_{0.93}$/1.0 nm SiO_2)	81.0
B2.4	1 nm SiO_2 + 17.5×(3.5 nm $SiO_{0.93}$/1.2 nm SiO_2)	84.4
B2.5	1 nm SiO_2 + 17.5×(3.5 nm $SiO_{0.93}$/1.4 nm SiO_2)	87.8
B2.6	1 nm SiO_2 + 17.5×(3.5 nm $SiO_{0.93}$/2.0 nm SiO_2)	98.0
B2.7	1 nm SiO_2 + 17.5×(3.5 nm $SiO_{0.93}$/2.5 nm SiO_2)	106.5

The J-E characteristics of samples B1 are reported in Fig. 4.13(a). When going from 1 nm SiO_2 barrier thickness up to 4 nm, the current decreases by around seven orders of magnitude at a fixed electric field. In fact, the 4 nm sample is

quite close to the pure Fowler-Nordheim current that is also shown in Fig. 4.13(a). However, from Fig. 4.13(b) it is apparent that no electrons are injected into the SL from the Si substrate for the 2 nm and the 4 nm sample. This is explained by the observations made in TEM shown in Fig. 3.11. The bottom SiO_2 barrier impedes electron injection from the Si substrate, because it is much larger than intended due to the parasitic oxidation effect [66]. The results indicate that a thorough investigation on the effect of the SiO_2 barrier thickness requires identical carrier injection properties. Therefore the second set of samples was fabricated.

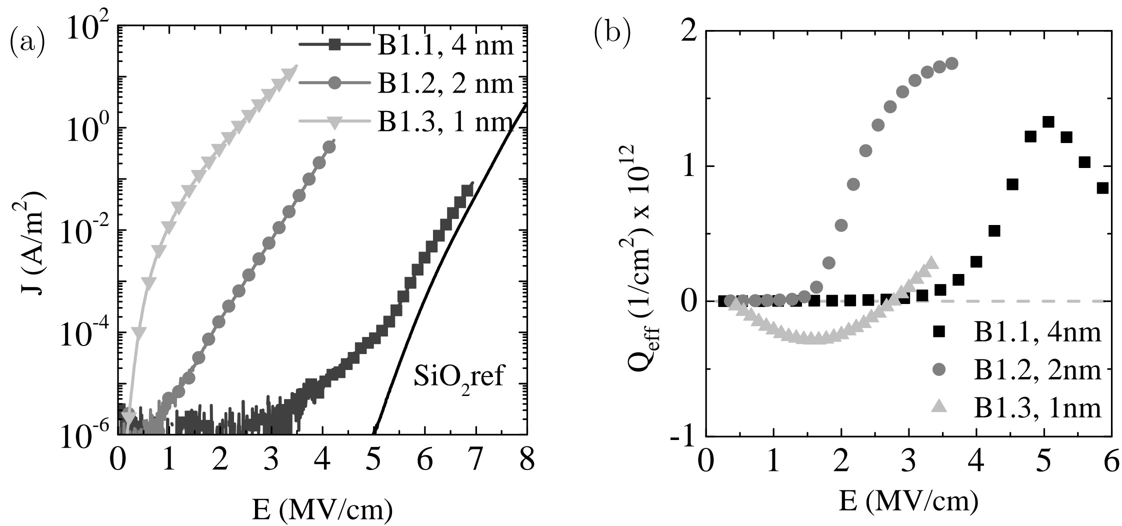

Figure 4.13: Electrical characterization of sample set B1 (cf. Tab. 4.3): (a) J-E characteristics, (b) charge trapping

Fig. 4.14(a) and (b) show the J-E and the charge trapping characteristics of sample set B2 featuring very small steps in the nominal thickness of the SiO_2 barrier. In contrast to the results presented in Fig. 4.13, good electron injection contacts were achieved for all samples (cf. Fig. 4.14(b)). As can be seen in Fig. 4.14(a), J is continuously increased as the SiO_2 barrier thickness is decreased.

From 2.5 nm to 1.5 nm, J rises by about one order of magnitude per 0.5 nm which is one order of magnitude less than predicted by the calculations presented in Fig. 4.6(a). This difference most likely stems from ideality deviations that are assumed in the calculation of the electron transfer time. First, the conduction band offset is not abrupt, but varies continuously within 0.5 nm across the interface [192]. Secondly, an image charge induced barrier lowering may considerably affect the energy barrier especially in case of very thin barriers [193]. Defects within the SiO_2

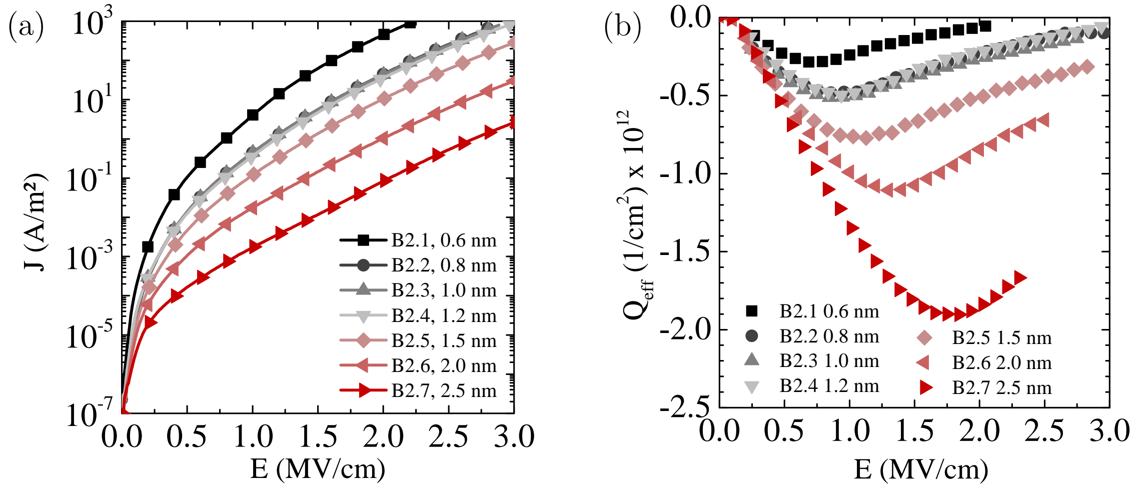

Figure 4.14: Electrical characterization of the B2 sample series: (a) J-E characteristics, (b) charge trapping

matrix may further enhance the barrier transmission probability. All effects strongly influence the electronic coupling between two neighboring Si NCs and render the distance dependence less pronounced.

In the range from 1.2 nm to 0.8 nm, the J-E curves are almost identical, but it is difficult to exclude PECVD process tolerances as a possible origin here due to the extreme thinness of the barrier layers. When going down to 0.6 nm another order of magnitude in current is gained. At this point, the SL integrity is already in question and adjacent Si NC layers might have coalesced. In contrast, from Fig. 4.14(b) it is observed that the magnitude of observed charge trapping is greatly decreased as the conductivity of the films is increased. In addition, the charging minima shifts to higher electric fields which simply reflects the increased efficiency of the C-V flatband shift method as the SL becomes less conductive.

4.3.4 Effect of Silicon Nanocrystal Areal Density and Size

The structural properties of individual Si NC layers can be tuned by varying the stoichiometry or the thickness of the SRON layer as it was demonstrated in sec. 3.2. It is interesting to see how these structural parameters affect the electronic properties. We start by studying the three stoichiometries investigated in Fig. 3.8. The corresponding samples are listed in Tab. 4.4.

Table 4.4: Samples made for electrical characterization with a variation of the SRON stoichiometry.

name	SL structure	d_{nom} (nm)
D1=B1.3	$5\times(1$ nm $SiO_2/3.5$ nm $SiO_{0.93})$	22.5
D2	$5\times(1$ nm $SiO_2/3.5$ nm $SiO_{0.85})$	22.5
D3	$5\times(1$ nm $SiO_2/3.5$ nm $SiO_{0.64})$	22.5

In Fig. 4.15(a), it is demonstrated that a larger Si excess within the SRON layer enhances the conductivity. Increasing the Si excess, increases the average Si NC size, whereas the Si NC areal densities are reduced (cf. Tab. 3.1). Both effects should somewhat reduce the current that can be passed through the device (cf. Fig. 4.6). However, the opposite effect is observed in Fig. 4.15(a). Apparently, the increased area fill fraction at higher Si excess leads to a better network connectivity in vertical direction in terms of a percolation model. This is substantiated at least partly by the observed trapping behaviour in Fig. 4.15(b). As the Si content is increased, the effective charge trapping is reduced. It has to be noted again that this behavior might also arise from the increased conductivity of the SL film in view of the non-equilibrium nature of the C-V measurements.

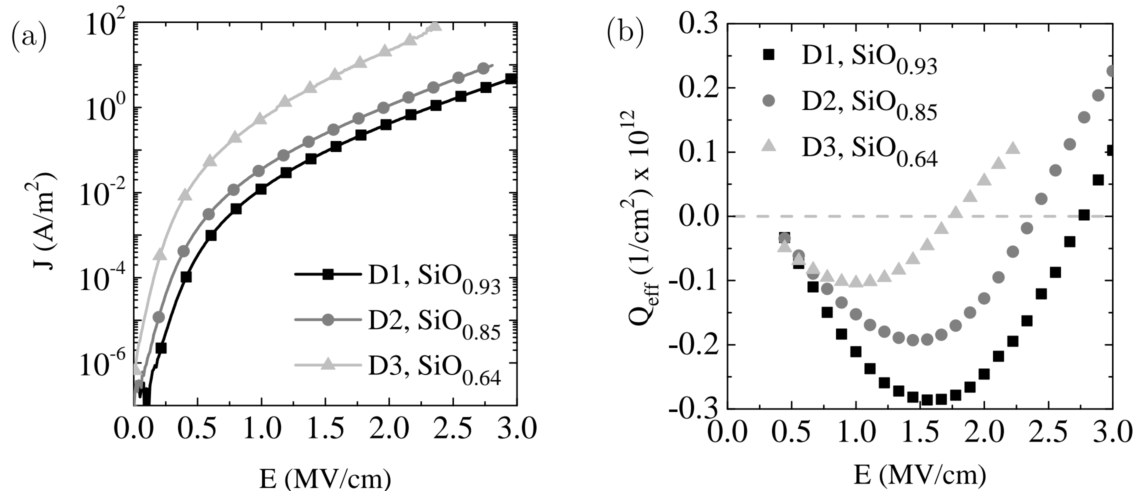

Figure 4.15: Electrical characterization of sample series D described in Tab. 4.4: (a) J-E characteristics, (b) charge trapping

In constrast to changing the SRON stoichiometry, the reduction of the SRON thickness offers better control of the Si NC size and shape (cf. Fig. 3.7) accompanied by an increase of the areal Si NC density (cf. Tab. 3.1). Therefore, samples of different SRON thicknesses were prepared for electrical characterization as listed in Tab. 4.5.

Table 4.5: Samples of different SRON thickness and similar total thickness.

name	SL structure	d_{nom} (nm)
S1	28×(1 nm SiO_2/2.5 nm $SiO_{0.93}$)	98
S2	25×(1 nm SiO_2/3.0 nm $SiO_{0.93}$)	100
S3	22×(1 nm SiO_2/3.5 nm $SiO_{0.93}$)	99
S4	20×(1 nm SiO_2/4.0 nm $SiO_{0.93}$)	100
S5	18×(1 nm SiO_2/4.5 nm $SiO_{0.93}$)	99

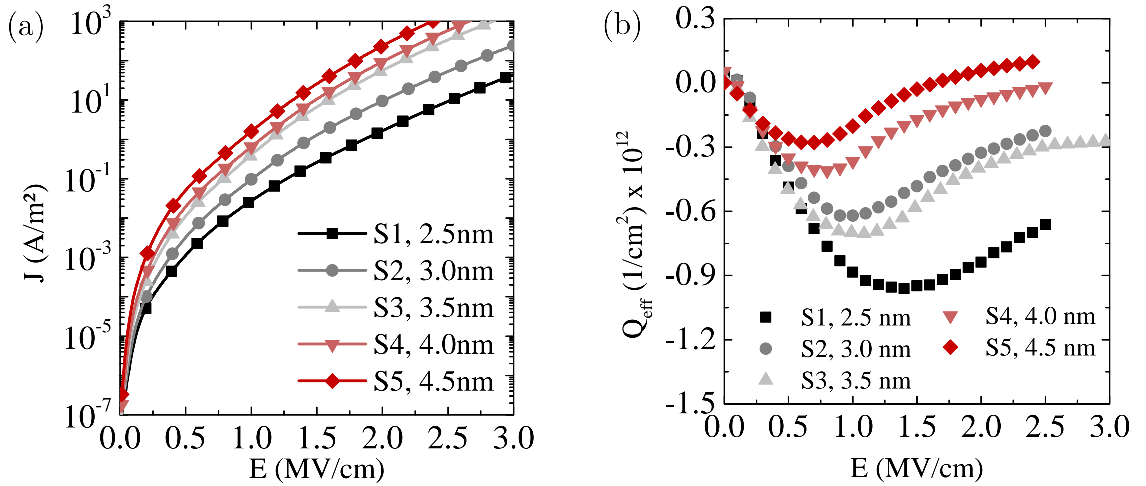

Figure 4.16: Electrical characterization of sample series S described in Tab. 4.5: (a) J-E characteristics, (b) charge trapping

In Fig. 4.16, it is demonstrated that the conductivity as an increasing function of SRON thickness, i.e. of Si NC size. This does neither follow from the structural properties nor from the theoretical predictions. As the Si NC size is increasing, the

areal density is decreasing (cf. Tab. 3.1) and the fill fraction should be constant. In addition, the electron transfer theory predicts that the electron transfer rate should be increased for smaller Si NCs (cf. Fig. 4.6(a)). The result is rather understood in terms of the macroscopic transport model. A reduction in Si NC size leads to a reduced density of states near the conduction band edge and consequently reduces the current as more carriers remain trapped at the defects for smaller Si NCs.

4.3.5 Phosphorus Doped Superlattices

All previous measurements were performed on intrinsic layers such that all charge carriers had to be injected at the contacts. Thus in this section, the electronic properties of P doped SLs are investigated for the samples described in Tab. 4.6.

Table 4.6: Sample description of the investigated P doped samples. The SiO_2 barrier thickness is increased with respect to the undoped samples studied in the previous sections.

name	SL structure (nm)	d_{nom} (nm)	c_p (at%)
P1	1.5 SiO_2 + 16.5×(4 $SiO_{0.93}$/2 SiO_2)	101.5	0
P2	1.5 SiO_2 + 16.5×(4 $SiO_{0.93}$/2 SiO_2)	101.5	0.13
P3	1.5 SiO_2 + 16.5×(4 $SiO_{0.93}$/2 SiO_2)	101.5	0.26
P4	10 SiO_2 + 13.5×(4 $SiO_{0.93}$/2 SiO_2) + 10 SiO_2	102	0
P5	10 SiO_2 + 13.5×(4 $SiO_{0.93}$/2 SiO_2) + 10 SiO_2	102	0.13
P6	10 SiO_2 + 13.5×(4 $SiO_{0.93}$/2 SiO_2) + 10 SiO_2	102	0.26

In Fig. 4.17(a) it is demonstrated that the current of the P doped films is enhanced at lower electric fields, but approaches the intrinsic conductivity at electric fields exceeding 1 MV/cm. The time-resolved current in Fig. 4.17(b) clearly saturates at different levels proving that J in Fig. 4.17(a) is not due to transient charging effects.

In order to decide whether the current enhancement is a result of excess electrons within the SL or is of a different origin, the samples with carrier injection barriers were fabricated. Indeed a displacement current peak at low electric fields in Fig. 4.18 indicates that the current increase in Fig. 4.17(a) is a result of quasi-free electrons.

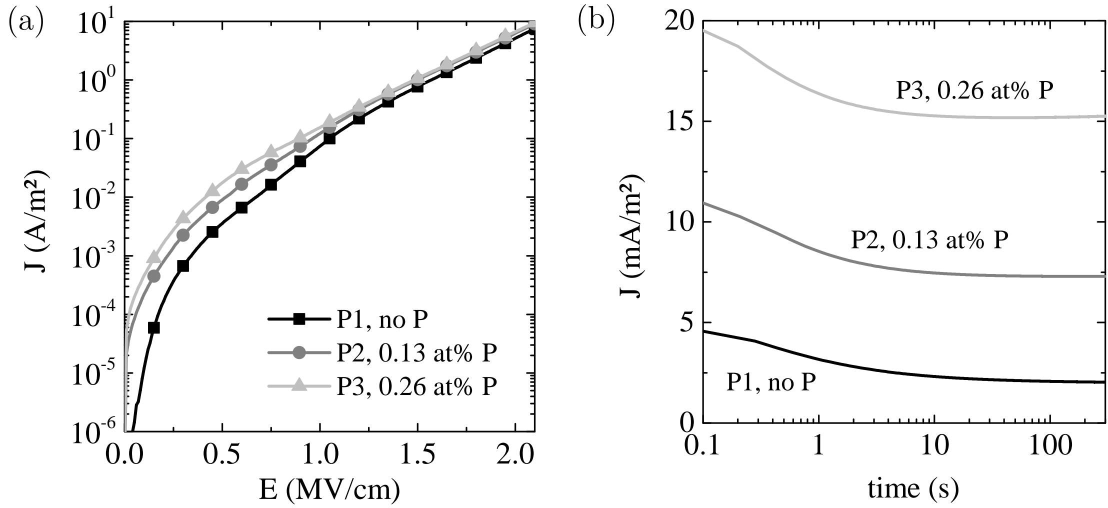

Figure 4.17: (a) J-E characteristics of the conducting P doped samples listed in Tab. 4.6. (b) Transient current of the samples from (a) at 0.5 MV/cm.

In the current blocking device, all donor electrons are attracted towards the gate and leave behind their positively charged donor ions (see inset of Fig. 4.18(a)).

Assuming now that the current peak in Fig. 4.18(a) originates from donor electrons only, one may estimate their average activation energy. This is done by calculating the voltage that drops across the SiO_2 barrier at the electric field, where the current peaks. Considering a capacitive voltage divider between Si and SiO_2, one obtains an approximate activation energy of 110±30 meV. This result supports well the findings of sec. 3.4.2 that P is incorporated within the Si NC, but the donor electron is strongly localized at the P atom.

Furthermore, it is possible to integrate the transient current density in Fig. 4.18(b). Invoking the Shockley-Ramo theorem [189–191], the donor concentration is calculated by

$$N_D = \frac{\int J(t)\mathrm{d}t}{qd_e} \tag{4.29}$$

where $d_e \approx 40$ nm is the average electron travel distance in these samples. We obtain values of $N_{D,P2} = 2.1 \times 10^{17}$ cm^{-3} and $N_{D,P3} = 3.65 \times 10^{17}$ cm^{-3} for samples P2 and P3 respectively. Please note that a full donor ionization and ideal charge separation as depicted in the inset of Fig. 4.18(a) leads to a significant change of the local potential within the SL. Close to the Si substrate, the potential drop between two Si NC planes is enhanced, whereas it is reduced in the vicinity of the

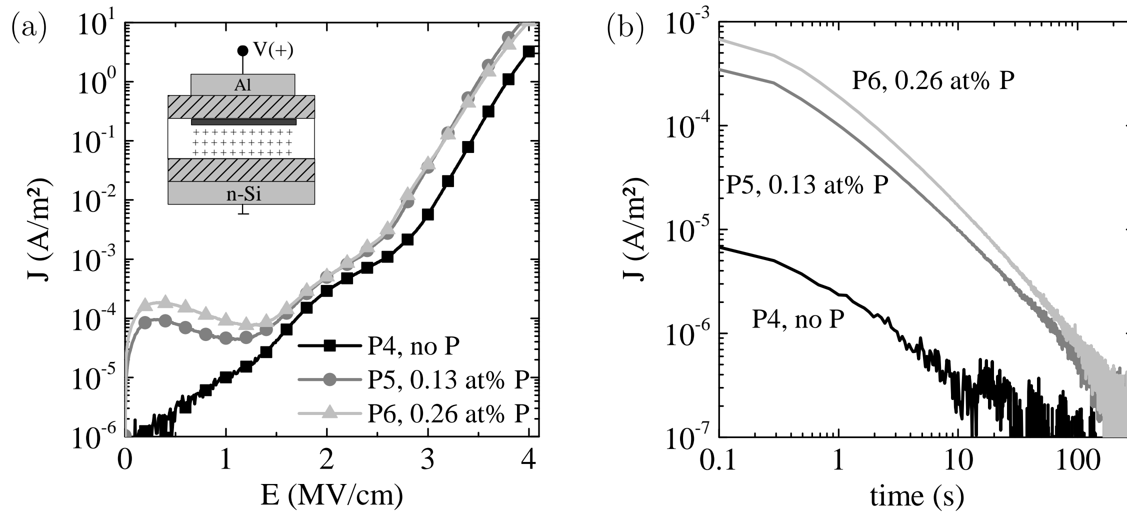

Figure 4.18: J-E characteristics of the non-conducting P doped samples listed in Tab. 4.6. (b) Transient current of the non-conducting samples at 0.5 MV/cm indicating that donor electrons are separated from their host ion (cf. inset of (a)).

Al contact. By applying a Poisson solver to the sample structure, it follows that a complete donor ionization can only be reached for sample P2, whereas the electric field becomes significantly screened by the mobile charge in sample P3 effectively limiting the ionization.

Interpolation of the Si NC areal density for the present samples from the data in Tab. 3.1 gives $\approx 2.6 \times 10^{12}$ cm^{-2}, hence the Si NC volume density becomes $\approx 4.3 \times 10^{18}$ cm^{-3}. Consequently, the average number of donors per Si NC with comparably shallow energy levels is estimated to be 0.05 for P2 and 0.08 for P3. In contrast, drawing upon the APT results from sec. 3.4.2 and applying similar arguments as in sec. 3.4.3, values of 4.8 and 9.6 are deduced for the amount of P atoms within a Si NC. Therefore, only about 1% of incorporated P atoms seem to be electronically active, albeit with a rather high ionization energy well above kT. Please note that these results agree well with PL results (see sec. 3.4.3).

4.4 Charge Transport Regimes and Mechanisms

This section is intended to recapitulate the view on transport properties of Si NC/SiO_2 SLs that emerged within this thesis. Due to the low conductivity of the devices, comparably large electric fields can be applied before electrical breakdown. Thus, four band diagrams are sketched in Fig. 4.19 that represent different transport regimes depending on the applied electric field.

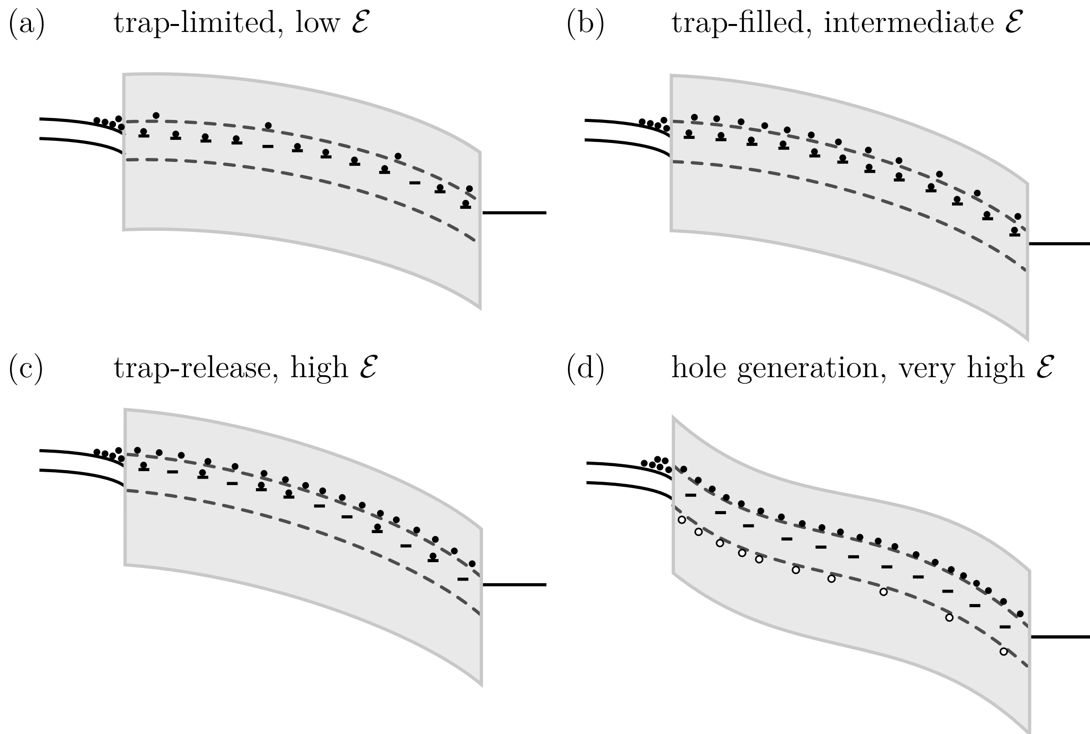

Figure 4.19: Transport regimes that could be identified in the course of this work. The grey box indicates the forbidden bandgap region of the SiO_2. The dotted lines represent a transport conduction band and valence band induced by the presence of the Si NCs. Single dashes within the gap indicate localized defects originating from Si/SiO_2 surface defects. A detailed explanation of the subfigures is given in the text.

The neglible intrinsic carrier concentration requires carrier injection at the contacts leading to SCLC. At low electric fields, the present defects capture most of the injected electrons (Fig. 4.19(a)). Hence, the energy bands are flat at the point of injection and the current is limited by the traps. The conduction band electron density is in quasi-equilibrium with the trapped electrons according to the SCLC theory. It is important to note that in this regime, not only deep defects serve as

electron traps, but also a non-neglible amount of tail states that arise from the Si NC size dispersion.

Increasing the electric field eventually fills all traps and consequently most of the injected carriers contribute to transport (Fig. 4.19(b)). The trapping arises now mostly from deep defects, i.e. Si surface DBs. However, at even higher electric fields, the electric field assisted trap release rate becomes comparable to the trapping rate (Fig. 4.19(c)). This high rate carrier exchange between the trap levels and the conduction band is clearly no longer a thermal equilibrium process although the magnitude of conduction is still limited by the space-charge.

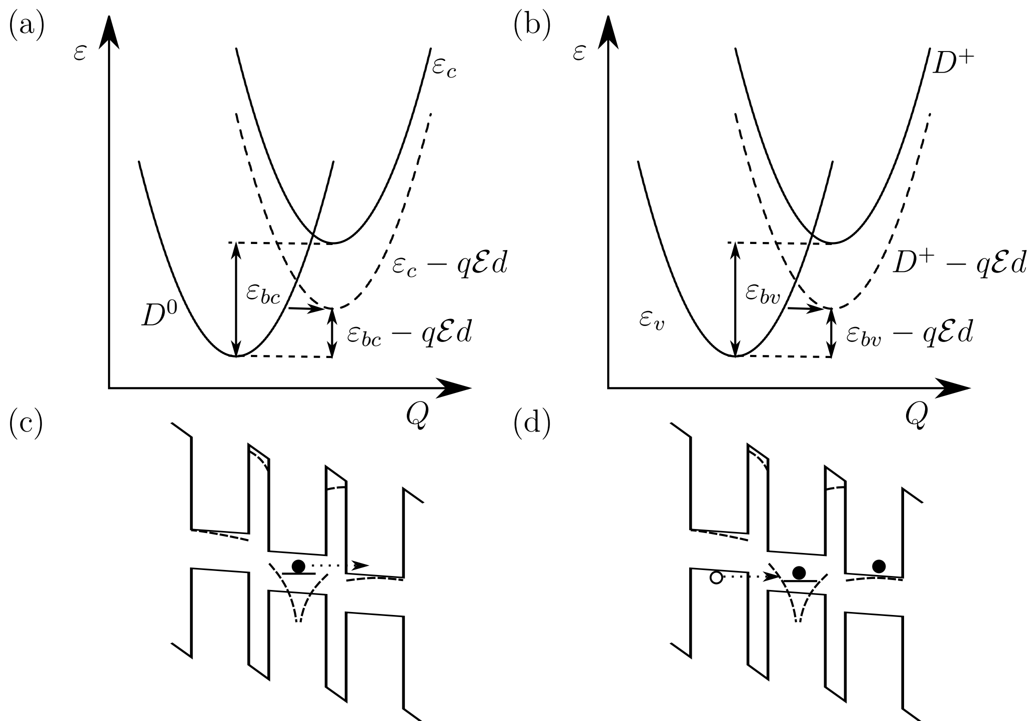

Figure 4.20: (a) and (b) represent configuration coordinate diagrams for the electric field enhanced transitions from (a) a D^0 state to the ground conduction state of a Si NC and (b) tunneling of a valence band electron to a charged defect state D^+, (c) energy band diagram representation of the transition in (a), (d) energy band diagram representation of the transition in (b). The dashed lines in (c) and (d) indicate the positive defect coulomb potential that is seen by the defect electron in (c) and by the valence electrons in case of the charged D^+ state in (d).

The situation becomes complex, when extremely high electric fields are applied. A large amount of holes seems to be created within the film (Fig. 4.19(d)) which was demonstrated to be linked with the presence of DBs. One can imagine that under the application of an electric field, the neutral DB is ionized by the tunneling of the electron to the conduction band of an adjacent SiNC.

This situation is well described by a configuration diagram shown in Fig. 4.20(a). The system energy is plotted as a function of the dimensionless lattice coordinate Q for the neutral DB and the lowest conduction state of a neighboring SiNC. By interaction with the lattice, the electron can increase its energy along the parabola. A tunneling transition to the SiNC conduction state can only occur, if the electron gains enough energy to overcome the energy barrier ε_{bc}. Since this barrier is usually too large, the application of an electric field can reduce its magnitude significantly as shown by the dashed line in Fig. 4.20(a).

The problem of the electric field-assisted tunneling transition of a deep defect state to the conduction band was treated theoretically [194–196] and has been shown to increase as $\propto \exp(a\mathcal{E}^2)$ very similar to the Marcus equation (eqn. 4.9). The corresponding transition is highlighted in the band diagram representation of Fig. 4.20(c). Once this transition has occurred, the DB relaxes to the D^+ charge state by the emission of multiple phonons. This new situation should allow for a second transition between electrons in the valence band and the charged DB. The configuration diagram and the band diagram for this transition are shown in Fig. 4.20(b) and (d), respectively. In this way, a space-separated free electron-hole pair is created by the presence of the defect. Please note that the positive defect potential leads to barrier height decrease as indicated in Fig. 4.20(b) and (d).

5 Summary and Outlook

Understanding the electronic transport properties of Si NC networks in SiO_2 is a challenging task. The main reasons are the complex three-dimensional morphology, the insulating nature of the SiO_2 and the absence of free carriers. The former issues were addressed in this work by studying the structural and electronic properties of Si NC/SiO_2 superlattices, whereas the latter one was tackled by P doping.

In the first part, the Si NC size and order was investigated thoroughly as a function of all three design parameters namely the SRON thickness and stoichiometry as well as the SiO_2 barrier thickness. It was found that interlayer coalescence is constricted down to 1 nm SiO_2 thickness. In addition, it was demonstrated that the Si NC areal density, shape and size can be measured precisely by using in-plane EF-TEM imaging. By increasing the Si excess towards very high Si concentration, the Si NCs become larger and their shape irregular. In contrast, the Si NC areal density is reduced which indicates the transition to a two-dimensional spinodal network. During these studies it was noticed that the excess Si is lost during the annealing procedure which is possibly related to the emanation of SiO molecules.

In the second part, it was demonstrated that the charge transport properties of Si NC/SiO_2 SLs are dominated by the presence of Si surface defects over the complete range of electric fields. The J-E and trapping characteristics reveal that the charge transport is space-charge limited and strongly depends on the number of available free carriers. A quantitative inspection by means of electron paramagnetic resonance should be carried out for the SLs. Although the effects of defects are prominent, it was shown theoretically and experimentally how the structural properties affect the charge transport properties. It appears that an increased conductivity is generally linked to the total Si excess within the SL. It is important to note that neither coulomb blockade nor resonant tunneling effects occur in these samples. Temperature-dependent electrical characterization may yield further insight in the transport mechanism, but great care has to be taken in the analysis of the results.

P doped SLs were prepared and studied with respect to P localization. It was demonstrated by XPS and XANES that P is incorporated into the Si NCs. Moreover, the excellent resolution of APT corrobates this finding by providing direct evidence of P localization within the Si NCs. However, significant amounts of P atoms accumulate at the nanocrystalline interface, whereas most of the dopants reside in the matrix. Additionally, the Si NC size dependence of P incorporation was derived from the APT data clearly evidencing the self-purification mechanism.

A remaining issue concerns the exact chemical surrounding of the P atoms within the Si NCs. Although, APT is in general capable of resolving individual atomic crystal planes [197], the situation is complicated due to the local magnification effect induced by the matrix that severely distorts the data reconstruction. Therefore, P not necessarily occupies a substitutional site within the Si NCs and other configurations such as interstitial P are possible (see [198] and references therein). In addition, XPS and XANES indicate that the donor electron is most likely strongly bound to the P ion at room temperature even if P was incorporated substituitionally into the Si NC. This finding is substantiated by electrical measurements that allow to estimate a donor binding energy on the order of 100 meV. At this point, it should be noted that no free-electron absorption [122] could be measured by infrared absorption measurements which could be due to the low sensitivity. In addition, sensitive low temperature infrared absorption in the range from 12 meV to 50 meV did not give rise to any intraband absorption lines such as in the Si bulk counterpart [199, 200].

Furthermore, it was found from the electrical measurements that only about 1% of P within the Si NCs provide electrons for transport. This result agrees well with the observed low PL quenching in P doped Si NCs allowing to conclude that the majority of P atoms does not change the recombination properties of the Si NCs. Therefore, it is highly desirable to carry out electron paramagnetic resonance measurements in order to quantify the amount of substituitional P in the SLs [33, 123, 125, 201, 202]. Moreover, the contribution of the surface defects and P dopants to transport may be probed directly by means of electrically detected paramagnetic resonance [203]. However, in view of the results so far, future research should concentrate on alternating doping approaches, i.e. the effect of different dopant species as well as the possibility of modulation doping [204]. Any such investigation will require a solid basis in terms of chemical and structural characterization in order to support optical and electrical characterization techniques.

The Si NCs in this work were prepared by high-temperature solid-state precipitation of silicon-rich oxynitride and hence there exists a natural structural disorder whose characteristic lengths are mainly controlled by the thermal budget imposed on the sample. Significant advantages may be offered by colloidal Si NCs [205, 206] due to the ability of size selection to create nearly monodisperse ensembles [207]. Furthermore, organic ligand surface capping was demonstrated to yield an exceptionally low density of surface defects [208] and high absolute quantum yields [209, 210]. In addition, such colloidal quantum dots may be self-assembled while the dot-to-dot distance is precisely controlled by the ligand length [211]. By carefully choosing a suitable solvent material, the dielectric properties of the matrix surrounding can be tuned [212] and even chemical modulation doping can be achieved [213, 214].

A Appendix

A.1 Calculation of the total Wave-function of a Spherical Si Nanocrystal Embedded in Silicon Dioxide

The general three-dimensional Schrödinger equation cannot be solved analytically for a spherically symmetric potential well, but needs to be transformed to the polar coordinate system [215]. In the spherical coordinate system, the Schrödinger equation is separable and can be solved for radial and angular part independently. The radial part ψ_R is then written as:

$$\frac{1}{r^2}\frac{\partial}{\partial r}\left(r^2\frac{\partial\psi_R(r)}{\partial r}\right)+\left(\frac{2m}{\hbar^2}\left(\varepsilon-H(r)\right)-\frac{l(l+1)}{r^2}\right)\psi_R(r)=0 \tag{A.1}$$

where l are positive integers. The potential $H(r)$ for the spherical square well is:

$$H(r)=\begin{cases}-V_0 & \text{if } r\leq R\\ 0 & \text{if } r>R\end{cases} \tag{A.2}$$

where R is the Si NC radius. We now consider the zero angular momentum case ($l=0$), recast eqn. A.1 by substituting $\psi_R(r)=\psi'(r)/r$ and obtain

$$-\frac{\hbar^2}{2m}\frac{\partial^2\psi'_R(r)}{\partial r^2}+\left(H(r)+\frac{l(l+1)\hbar^2}{2mr^2}\right)\psi'_R(r)=\varepsilon\psi'_R(r) \tag{A.3}$$

The solutions of $\psi'_R(r)$ for specific case of $l=0$ (ground state) are:

$$\psi'_R(r)=\begin{cases}A\sin\alpha r+B\cos\alpha r & \text{if } r\leq R\\ Ce^{-\beta r} & \text{if } r>R\end{cases} \tag{A.4}$$

where

$$\alpha = \left[\frac{2m_{Si}(|\varepsilon_1|)}{\hbar^2}\right]^{1/2} \tag{A.5}$$

$$\beta = \left[\frac{2m_{ox}(V_0 - |\varepsilon_1|)}{\hbar^2}\right]^{1/2} \tag{A.6}$$

where m_{Si} and m_{ox} are the electron effective masses in the Si NC and SiO_2, respectively and ε_1 is the ground state energy. The first boundary condition requires $\psi'_R(0) = 0$, because $\lim_{r\to 0} \psi(r)/r$ must not be zero after back substitution, hence $B = 0$. The continuity boundary condition at the Si NC interface is [216]:

$$\frac{1}{\sqrt{m_{Si}}}\frac{\partial\psi}{\partial r}\bigg|_{r=R-\delta} = \frac{1}{\sqrt{m_{ox}}}\frac{\partial\psi}{\partial r}\bigg|_{r=R+\delta} \tag{A.7}$$

and leads directly to the following equation:

$$\alpha R \cot \alpha R = 1 - \sqrt{\frac{m_{Si}}{m_{ox}}} - \beta R\sqrt{\frac{m_{Si}}{m_{ox}}} \tag{A.8}$$

One is now left with three equations eqn. A.5, eqn. A.6 and eqn. A.8 to solve for the unknown variables α, β and E_i. This requires that one knows the effective masses m_{Si} and m_{ox}. The effective mass in the SiO_2 at neglible electric field was determined to be $m_{ox} = 0.3m_e$ [217]. As explained in sec. 4.1.1 of this work, the effective mass theory is questionable in case of Si NCs. However, if one knows the ground state energy from experiment or more elaborated calculations, one may solve for m_{Si} instead of ε_1 and obtain a solution that satisfies the spherical Schrödinger equation. Please note that there is no analytical form to solve this set of equation and hence a numerical solving algorithm has to be employed.

A.2 Numerical Calculation of Space-Charge-Limited Currents

In sec. 4.2 the theory of SCLC was explained. The equations governing the J-E characteristics in the space-charge limited regime are the current continuity equation in the form of Ohm's law

$$J = q\mu n(z)\mathcal{E}(z) = const \tag{A.9}$$

and the Poisson equation

$$-\frac{\partial\Phi(z)}{\partial z^2} = \frac{\partial\mathcal{E}(z)}{\partial z} = \frac{qn(z)}{\epsilon_0\epsilon_r} \tag{A.10}$$

Analytical solutions of the coupled equations exist only for selected special cases. Hence analytical solutions don't offer the versatility of a straightforward numeric solution. In addition, it might be desirable to calculate the J-E characteristics to include a field-dependent mobility that is obtained from other measurements. The numerical solution employed in this work, is described in the following. In the first step, the continuity and Poisson equation are rewritten in such a way to separate the variables $\mathcal{E}$ and z:

$$\mathrm{d}z = f(\mathcal{E})\mathrm{d}\mathcal{E} \tag{A.11}$$

Then the field-dependent function is numerically integrated for the case of specified current density J and the integral form $F(\mathcal{E})$ is obtained. It relates the position coordinate z to the electric field $\mathcal{E}$. Since $\mathcal{E}$ is monotonic in z, it can be inverted to express the electric field $\mathcal{E}$ as a function of distance z:

$$\mathcal{E} = F^{-1}(z) \tag{A.12}$$

Please note that the boundary condition of $\mathcal{E} = 0$ at $z = 0$ is directly included in the

integration procedure. In the last step, the electric field is integrated numerically from the cathode ($z = 0$) to the anode ($z = d_{ox}$) to obtain the applied voltage V and consequently the applied ohmic electric field ($\mathcal{E}_\Omega = V/d_{ox}$) that corresponds to the current density that was chosen at the beginning of the procedure:

$$V = \int_0^{d_{ox}} F^{-1}(z)\mathrm{d}z \tag{A.13}$$

This procedure has to be repeated for each point in the J-E characteristics. All calculations were done with Matlab.

In the following, $f(\mathcal{E})$ is derived for the special case of of a single trap level. The continuity and Poission equation are rewritten in order to incorporate free (n_f) and trapped charges n_t:

$$J = qn_f(z)\mu_f\mathcal{E}(z) \tag{A.14}$$

and

$$\frac{\partial\mathcal{E}(z)}{\partial z} = q\frac{n_f(z) + n_t(z)}{\epsilon_0\epsilon_r} \tag{A.15}$$

Furthermore, an expression relating n_f and n_t is required and readily found by assuming Fermi-Dirac statistics for the defect level and Maxwell-Boltzmann statistics for the conduction band:

$$n_t = \frac{N_T}{1 + \frac{N_C}{n_f}\exp\left(-\frac{E_T}{kT}\right)} \tag{A.16}$$

Finally, $f(\mathcal{E})$ becomes:

$$f(\mathcal{E}) = \frac{\epsilon_0\epsilon_r}{q\left(\frac{J}{q\mu_f\mathcal{E}} + \frac{N_T}{1+\frac{qN_C\mu_f\mathcal{E}}{J}\exp\left(-\frac{E_T}{kT}\right)}\right)} \tag{A.17}$$

Bibliography

[1] V. Lehmann and U. Gösele. “Porous Silicon Formation: A quantum wire effect”. In: *Applied Physics Letters* 58 (1991), pp. 856–858.

[2] L. T. Canham. “Silicon quantum wire array fabrication by electrochemical and chemical dissolution of wafers”. In: *Applied Physics Letters* 57 (1990), pp. 1046–1048.

[3] G. Franzo, A. Irrera, E.C.Moreira, M. Miritello, F. Iacona, D. Sanfilippo, G. D. Stefano, P. Fallica, and F. Priolo. “Electroluminescence of silicon nanocrystals in MOS structures”. In: *Applied Physics A* 74 (2002), pp. 1–5.

[4] R. J. Walters, G. I. Bourianoff, and H. A. Atwater. “Field-effect electroluminescence in silicon nanocrystals”. In: *Nature Materials* 4 (2005), pp. 143–146.

[5] F. Maier-Flaig, J. Rinck, M. Stephan, T. Bocksrocker, M. Bruns, C. Kübel, A. K. Powell, G. A. Ozin, and U. Lemmer. “Multicolor Silicon Light-Emitting Diodes (SiLEDs)”. In: *Nano Letters* 13 (2013), pp. 475–480.

[6] M. A. Green, J. Zhao, A. Wang, P. J. Reece, and M. Gal. “Efficient silicon light-emitting diodes”. In: *Nature* 412 (2001), pp. 805–808.

[7] L. Pavesi, L. D. Negro, C. Mazzoleni, G. Franzo, and F. Priolo. “Optical gain in silicon nanocrystals”. In: *Nature* 408 (2000), pp. 440–444.

[8] M. Cazzanelli, D. Navarro-Urrios, F. Riboli, N. Daldosso, L. Pavesi, J. Heitmann, L. X. Yi, R. Scholz, M. Zacharias, and U. Gösele. “Optical gain in monodispersed silicon nanocrystals”. In: *Journal of Applied Physics* 96 (2004), pp. 3164–3171.

[9] H. Rong, R. Jones, A. Liu, O. Cohen, D. Hak, A. Fang, and M. Paniccia. “A continuous-wave Raman silicon laser”. In: *Nature* 433 (2005), pp. 725–728.

[10] H. Rong, A. Liu, R. Jones, O. Cohen, D. Hak, R. Nicolaescu, A. Fang, and M. Paniccia. “An all-silicon Raman laser”. In: *Nature* 433 (2005), pp. 292–294.

[11] I. Pelant. “Optical gain in silicon nanocrystals: Current status and perspectives”. In: *physica status solidi (a)* 208 (2011), pp. 625–630.

[12] G. Conibeer, M. Green, R. Corkish, Y. Cho, E.-C. Cho, C.-W. Jiang, T. Fangsuwannarak, E. Pink, Y. Huang, T. Puzzer, T. Trupke, B. Richards, A. Shalav, and K.-l. Lin. “Silicon nanostructures for third generation photovoltaic solar cells”. In: *Thin Solid Films* 511-512 (2006), pp. 654–662.

[13] M. C. Beard, K. P. Knutsen, P. Yu, J. M. Luther, Q. Song, W. K. Metzger, R. J. Ellingson, and A. J. Nozik. “Multiple Exciton Generation in Colloidal Silicon Nanocrystals”. In: *Nano Letters* 7 (2007), pp. 2506–2512.

[14] R. J. Walters, P. G. Kik, J. D. Casperson, H. A. Atwater, M. G. R. Lindstedt, and G. Bourianoff. “Silicon optical nanocrystal memory”. In: *Applied Physics Letters* 85 (2004), pp. 2622–2624.

[15] S. Tiwari, F. Rana, H. Hanafi, A. Hartstein, E. F. Crabbe, and K. Chan. “A silicon nanocrystals based memory”. In: *Applied Physics Letters* 68 (1996), pp. 1377–1379.

[16] D. Kovalev and M. Fujii. “Silicon Nanocrystals: Photosensitizers for Oxygen Molecules”. In: *Advanced Materials* 17 (2005), pp. 2531–2544.

[17] L. T. Canham. “Bioactive Silicon Structure Fabrication Through Nanoetching Techniques”. In: *Advanced Materials* 7 (1995), pp. 1033–1037.

[18] J.-H. Park, L. Gu, G. von Maltzahn, E. Ruoslahti, S. N. Bhatia, and M. J. Sailor. “Biodegradable luminescent porous silicon nanoparticles for in vivo applications”. In: *Nature Materials* 8 (2009), pp. 331–336.

[19] M. Zacharias, L. Yi, J. Heitmann, R. Scholz, M. Reiche, and U. Gösele. “Size-Controlled Si Nanocrystals for Photonic and Electronic Applications”. In: *Solid State Phenomena* 94 (2003), pp. 95–104.

[20] I. Balberg, E. Savir, J. Jedrzejewski, A. G. Nassiopoulou, and S. Gardelis. “Fundamental transport processes in ensembles of silicon quantum dots”. In: *Physical Review B* 75 (2007), p. 235329.

[21] I. Balberg. “Electrical transport mechanisms in three dimensional ensembles of silicon quantum dots”. In: *Journal of Applied Physics* 110 (2011), p. 061301.

[22] L. Tsakalakos. *Nanotechnology for Photovoltaics*. Ed. by L. Tsakalakos. Taylor & Francis, 2009.

[23] A. Wacker and A.-P. Jauho. “Quantum Transport: The Link between Standard Approaches in Superlattices”. In: *Physical Review Letters* 80 (1998), pp. 369–372.

[24] A. Wacker. “Semiconductor superlattices: a model system for nonlinear transport”. In: *Physics Reports* 357 (2002), pp. 1–111.

[25] M. T. Björk, O. Hayden, H. Schmid, H. Riel, and W. Riess. “Vertical surround-gated silicon nanowire impact ionization field-effect transistors”. In: *Applied Physics Letters* 90 (2007), p. 142110.

[26] V. Schmidt, H. Riel, S. Senz, S. Karg, W. Riess, and U. Gösele. “Realization of a Silicon Nanowire Vertical Surround-Gate Field-Effect Transistor”. In: *small* 2 (2006), pp. 85–88.

[27] M. T. Björk, J. Knoch, H. Schmid, H. Riel, and W. Riess. “Silicon nanowire tunneling field-effect transistors”. In: *Applied Physics Letters* 92 (2008), p. 193504.

[28] J. Appenzeller, J. Knoch, M. T. Björk, H. Riel, H. Schmid, and W. Riess. “Toward Nanowire Electronics”. In: *IEEE Transactions on Electron Devices* 55 (2008), pp. 2827–2845.

[29] J. Knoch, S. Mantl, and J. Appenzeller. “Impact of the dimensionality on the performance of tunneling FETs: Bulk versus one-dimensional devices”. In: *Solid-State Electronics* 51 (2007), pp. 572–578.

[30] J. Knoch, W. Riess, and J. Appenzeller. “Outperforming the Conventional Scaling Rules in the Quantum-Capacitance Limit”. In: *IEEE Electron Device Letters* 29 (2008), pp. 372–374.

[31] M. T. Björk, H. Schmid, J. Knoch, H. Riel, and W. Riess. “Donor deactivation in silicon nanostructures”. In: *Nature Nanotechnology* 4 (2009), pp. 103–107.

[32] M. Diarra, Y.-M. Niquet, C. Delerue, and G. Allan. “Ionization energy of donor and acceptor impurities in semiconductor nanowires: Importance of dielectric confinement”. In: *Physical Review B* 75 (2007), p. 045301.

[33] R. N. Pereira, A. R. Stegner, T. Andlauer, K. Klein, H. Wiggers, M. S. Brandt, and M. Stutzmann. “Dielectric screening versus quantum confinement of phosphorus donors in silicon nanocrystals investigated by magnetic resonance”. In: *Physical Review B* 79 (2009), 161304(R).

[34] R. Tsu and D. Babic. “Doping of a quantum dot”. In: *Applied Physics Letters* 64 (1994), pp. 1806–1808.

[35] P. Löper, D. Stüüwe, M. Künle, M. Bivour, C. Reichel, R. Neubauer, M. Schnabel, M. Hermle, O. Eibl, S. Janz, M. Zacharias, and S. W. Glunz. “A Membrane Device for Substrate-Free Photovoltaic Characterization of Quantum Dot Based p-i-n Solar Cells”. In: *Advanced Materials* 24 (2012), pp. 3124–3129.

[36] P. Löper, M. Canino, J. Lopez-Vidrier, M. Schnabel, F. Schindler, F. Heinz, A. Witzky, M. Bellettato, M. Allegrezza, D. Hiller, A. Hartel, S. Gutsch, S. Hernandez, R. Guerra, S. Ossicini, B. Garrido, S. Janz, and M. Zacharias. “Silicon nanocrystals from high-temperature annealing: Characterization on device level”. In: *physica status solidi (a)* 210 (2013), pp. 669–675.

[37] G. M. Dalpian and J. R. Chelikowsky. “Self-Purification in Semiconductor Nanocrystals”. In: *Physical Review Letters* 96 (2006), p. 226802.

[38] D. J. Norris, A. L. Efros, and S. C. Erwin. “Doped Nanocrystals”. In: *Science* 319 (2008), pp. 1776–1779.

[39] T.-L. Chan, M. L. Tiago, E. Kaxiras, and J. R. Chelikowsky. “Size Limits on Doping Phosphorus into Silicon Nanocrystals”. In: *Nano Letters* 8 (2008), pp. 596–600.

[40] M. Lannoo, C. Delerue, and G. Allan. “Screening in Semiconductor Nanocrystallites and Its Consequences for Porous Silicon”. In: *Physical Review Letters* 74 (1995), pp. 3415–3418.

[41] G. Allan, C. Delerue, M. Lannoo, and E. Martin. “Hydrogenic impurity levels, dielectric constant, and coulomb charging effects in silicon crystallites”. In: *Physical Review B* 52 (1995), pp. 11982–11988.

[42] D. V. Melnikov and J. R. Chelikowsky. “Quantum Confinement in Phosphorus-Doped Silicon Nanocrystals”. In: *Physical Review Letters* 92 (2004), p. 046802.

[43] S. Ossicini, F. Iori, E. Degoli, E. Luppi, R. Magri, R. Poli, G. Cantele, F. Trani, and D. Ninno. “Understanding Doping In Silicon Nanostructures”. In: *IEEE Journal of Selected Topics in Quantum Electronics* 12 (2006), pp. 1585–1591.

[44] A. R. Stegner, R. N. Pereira, R. Lechner, K. Klein, H. Wiggers, M. Stutzmann, and M. S. Brandt. “Doping efficiency in freestanding silicon nanocrystals from the gas phase: Phosphorus incorporation and defect-induced compensation”. In: *Physical Review B* 80 (2009), p. 165326.

[45] P. Y. Yu and M. Cardona. *Fundamentals of Semiconductors*. Springer, 1996.

[46] E. H. Nicollian and J. R. Brews. *MOS Physics and Technology*. Wiley, 1982.

[47] S. C. Erwin, L. Zu, M. I. Haftel, A. L. Efros, T. A. Kennedy, and D. J. Norris. "Doping semiconductor nanocrystals". In: *Nature* 436 (2005), pp. 91–94.

[48] J. D. Bryan and D. R. Gamelin. "Doped Semiconductor Nanocrystals: Synthesis, Characterization, Physical Properties, and Applications". In: *Progress in Inorganic Chemistry* 54 (2005), pp. 47–126.

[49] M. Zacharias, J. Heitmann, R. Scholz, U. Kahler, M. Schmidt, and J. Bläsing. "Size-controlled highly luminescent silicon nanocrystals: A SiO/SiO2 superlattice approach". In: *Applied Physics Letters* 80 (2002), pp. 661–663.

[50] A. Hartel, D. Hiller, S. Gutsch, P. Löper, S. Estrade, F. Peiro, B. Garrido, and M. Zacharias. "Formation of size-controlled silicon nanocrystals in plasma enhanced chemical vapor deposition grown SiOxNy/SiO2 superlattices". In: *Thin Solid Films* 520 (2011), pp. 121–125.

[51] E. R. v. Schweidler. "Studien über die Anomalien im Verhalten der Dielektrika". In: *Annalen der Physik* 24 (1907), pp. 711–770.

[52] A. K. Jonscher. "The universal dielectric response". In: *Nature* 267 (1977), pp. 673–679.

[53] K. S. Cole and R. H. Cole. "Dispersion and Absorption in Dielectrics II. Direct Current Characteristics". In: *Journal of Chemical Physics* 10 (1942), pp. 98–105.

[54] H. Reisinger, G. Steinlesberger, S. Jakschik, M. Gutsche, T. Hecht, M. Leonhard, U.Schröder, H.Seidl, and D. Schwann. "A comparative study of dielectric relaxation losses in alternative dielectrics". In: *Digest of IEEE International Electron Device Meeting*. Digest of IEEE International Electron Device Meeting 01 (2001), pp. 267–270.

[55] D. K. Schroder. *Semiconductor Material and Device Characterization 3rd Edition*. Wiley, 2006.

[56] A. M. Hartel, S. Gutsch, D. Hiller, and M. Zacharias. "Fundamental temperature-dependent properties of the Si nanocrystal band gap". In: *Physical Review B* 85 (2012), p. 165306.

[57] A. M. Hartel, S. Gutsch, D. Hiller, and M. Zacharias. "Intrinsic nonradiative recombination in ensembles of silicon nanocrystals". In: *Physical Review B* 87 (2013), p. 035428.

[58] D. B. Williams and C. B. Carter. *Transmission Electron Microscopy - A Textbook for Materials Science*. Ed. by D. B. Williams and C. B. Carter. Springer, 2009.

[59] S. Schamm, C. Bonafos, H. Coffin, N. Cherkashin, M. Carrada, G. B. Assayag, A. Claverie, M. Tence, and C. Colliex. "Imaging Si nanoparticles embedded in SiO2 layers by (S)TEM-EELS". In: *Ultramicroscopy* 108 (2008), pp. 346–357.

[60] G. B. Assayag, C. Bonafos, M. Carrada, A. Claverie, P. Normand, and D. Tsoukalas. "Transmission electron microscopy measurements of the injection distances in nanocrystal-based memories". In: *Applied Physics Letters* 82 (2003), pp. 200–202.

[61] J. Stöhr. *NEXAFS Spectroscopy*. Ed. by Springer. Springer, 1992.

[62] H. Gnaser and H. Oechsner. "SIMS depth profile analysis using MCs + molecular ions". In: *Fresenius Journal of Analytical Chemistry* 341 (1991), pp. 54–56.

[63] H. Gnaser. "Improved quantification in secondary-ion mass spectrometry detecting MCs+ molecular ions". In: *Journal of Vacuum Science and Technology A* 12 (1994), pp. 452–456.

[64] T. F. Kelly and D. J. Larson. "Atom Probe Tomography 2012". In: *Annual Review of Materials Research* 42 (2012), pp. 1–31.

[65] D. Hiller, S. Goetze, F. Munnik, M. Jivanescu, J. W. Gerlach, J. Vogt, E. Pippel, N. Zakharov, A. Stesmans, and M. Zacharias. "Nitrogen at the Si-nanocrystal / SiO2 interface and its influence on luminescence and interface defects". In: *Physical Review B* 82 (2010), p. 195401.

[66] A. M. Hartel, S. Gutsch, D. Hiller, C. Kübel, N. Zakharov, P. Werner, and M. Zacharias. "Silicon nanocrystals prepared by plasma enhanced chemical vapor deposition: Importance of parasitic oxidation for third generation photovoltaic applications". In: *Applied Physics Letters* 101 (2012), p. 193103.

[67] T. Müller, K.-H. Heinig, and W. Möller. "Size and location control of Si nanocrystals at ion beam synthesis in thin SiO2 films". In: *Applied Physics Letters* 81 (2002), pp. 3049–3051.

[68] S. Cheylan and R. G. Elliman. "Effect of hydrogen on the photoluminescence of Si nanocrystals embedded in a SiO2 matrix". In: *Applied Physics Letters* 78 (2001), pp. 1225–1227.

[69] D. Hiller, M. Jivanescu, A. Stesmans, and M. Zacharias. "Pb0 centers at the Si-nanocrystal/SiO2 interface as the dominant photoluminescence quenching defect". In: *Journal of Applied Physics* 107 (2010), p. 084309.

[70] J. Lopez-Vidrier, S. Hernandez, A. Hartel, D. Hiller, S. Gutsch, P. Löper, L. L.-C. S. Estrade, F. Peiro, M. Zacharias, and B. Garrido. "Structural and optical characterization of size controlled silicon nanocrystals in SiO2/SiOxNy multilayers". In: *Energy Procedia* 10 (2011), pp. 43–48.

[71] R. L. Pfeffer. "Damage center formation in SiO2 thin films by fast electron irradiation". In: *Journal of Applied Physics* 57 (1985), pp. 5176–5180.

[72] G. S. Chen and C. J. Humphreys. "Study of sample thickness dependence in electron-beam irradiation of selfdeveloping inorganic materials". In: *Journal of Applied Physics* 85 (1999), pp. 148–152.

[73] R. Egerton, P. Li, and M. Malac. "Radiation damage in the TEM and SEM". In: *Micron* 35 (2004), pp. 399–409.

[74] R. F. Egerton, F. Wang, and P. A. Crozier. "Beam-Induced Damage to Thin Specimens in an Intense Electron Probe". In: *Microscopy and Microanalysis* 12 (2006), pp. 65–71.

[75] R. Egerton, R.McLeod, F.Wang, and M.Malac. "Basic questions related to electron-induced sputtering in the TEM". In: *Ultramicroscopy* 110 (2010), pp. 991–997.

[76] M. Uematsu, H. Kageshima, Y. Takahashi, S. Fukatsu, K. M. Itoh, K. Shiraishi, and U. Gösele. "Modeling of Si self-diffusion in SiO2: Effect of the Si/SiO2 interface including time-dependent diffusivity". In: *Applied Physics Letters* 84 (2004), pp. 876–878.

[77] M. Jivanescu, D. Hiller, M. Zacharias, and A. Stesmans. "Size dependence of Pb-type photoluminescence quenching defects at the Si nanocrystal interface". In: *Europhysics Letters* 96 (2011), p. 27003.

[78] V. Beyer, J. von Borany, and K.-H. Heinig. "Dissociation of Si+ ion implanted and as-grown thin SiO2 layers during annealing in ultra-pure neutral ambient by emanation of SiO". In: *Journal of Applied Physics* 101 (2007), p. 053516.

[79] A. Sarikov, V. Litovchenko, I. Lisovskyy, I. Maidanchuk, and S. Zlobin. "Role of oxygen migration in the kinetics of the phase separation of nonstoichiometric silicon oxide films during high-temperature annealing". In: *Applied Physics Letters* 91 (2007), p. 133109.

[80] S. Boninelli, F. Iacona, G. Franzo, C. Bongiorno, C. Spinella, and F. Priolo. "Formation, evolution and photoluminescence properties of Si nanoclusters". In: *Journal of Physics: Condensed Matter* 19 (2007), p. 225003.

[81] T. M. Rogers and R. C. Desai. "Numerical study of late-stage coarsening for off-critical quenches in the Cahn-Hilliard equation of phase separation". In: *Physical Review B* 39 (1989), pp. 11956–11964.

[82] J. W. Cahn. "Phase Separation by Spinodal Decomposition in Isotropic Systems". In: *Journal of Chemical Physics* 42 (1965), pp. 93–99.

[83] A. S. Abyzov and J. W. Schmelzer. "Nucleation versus spinodal decomposition in confined binary solutions". In: *Journal of Chemical Physics* 127 (2007), p. 115504.

[84] V. E. Brunini, C. A. Schuh, and W. C. Carter. "Percolation of diffusionally evolved two-phase systems". In: *Physical Review E* 83 (2011), p. 021119.

[85] K. Binder, S. Puri, S. K. Das, and J. Horbach. "Phase Separation in Confined Geometries". In: *Journal of Statistical Physics* 138 (2010), pp. 51–84.

[86] T. Z. Lu, M. Alexe, R. Scholz, V. Talalaev, R. J. Zhang, and M. Zacharias. "Si nanocrystal based memories: Effect of the nanocrystal density". In: *Journal of Applied Physics* 100 (2006), p. 014310.

[87] J. F. Moulder, W. F. Stickle, P. E. Sobol, and K. D. Bomben. *Handbook of X-Ray Photoelectron Spectroscopy*. Ed. by J. Chastain and R. C. King. Physical Electronics, 1995.

[88] A. Thøgersen, M. Syre, B. R. Olaisen, and S. Diplas. "Studies of the oxidation states of phosphorus gettered silicon substrates using X-ray photoelectron spectroscopy and transmission electron microscopy". In: *Journal of Applied Physics* 113 (2013), p. 044307.

[89] M. Perego, C. Bonafos, and M. Fanciulli. "Phosphorus doping of ultra-small silicon nanocrystals". In: *Nanotechnology* 21 (2010), p. 025602.

[90] E.-C. Cho, S. Park, X. Hao, D. Song, G. Conibeer, S.-C. Park, and M. A. Green. "Silicon quantum dot/crystalline silicon solar cells". In: *Nanotechnology* 19 (2008), p. 245201.

[91] S. H. Baker, S. C. Bayliss, S. J. Gurman, N. Elgun, and E. A. Davis. "A structural and optical study of sputtered InP films as a function of preparation temperature". In: *Journal of Physics: Condensed Matter* 8 (1996), pp. 1591–1605.

[92] W. Ying, Y. Mizokawa, Y. Kamimura, K. Kawamoto, and W. Yang. "The Chemical Composition Changes of Silicon and Phosphorus in the Process of Native Oxide Formation of Heavily Phosphorus Doped Silicon". In: *Applied Surface Science* 181 (2001), pp. 1–14.

[93] Y. Sano, W. Ying, Y. Kamiura, and Y. Mizokawa. "Annealing induced phosphorus protrusion into thin-oxide films from heavily phosphorus-doped silicon (100)". In: *Thin Solid Films* 516 (2008), pp. 1788–1795.

[94] R. Franke and J. Hormes. "The P K-near edge absorption spectra of phosphates". In: *Physica B* 216 (1995), pp. 85–95.

[95] Y. H. Tang, T. K. Sham, A. Jürgensen, Y. F. Hu, C. S. Lee, and S. T. Lee. "Phosphorus-doped silicon nanowires studied by near edge x-ray absorption fine structure spectroscopy". In: *Applied Physics Letters* 80 (2002), pp. 3709–3711.

[96] A. Jürgensen. "The P(1s) and P(2p) XAFS Spectra of Elemental Phosphorus, Theory and Experiment". In: *Physica Scripta* T115 (2005), pp. 548–551.

[97] R. Sammynaiken, S. J. Naftel, T. K. Sham, K. W. Cheah, B. Averboukh, R. Huber, Y. R. Shen, G. G. Qin, Z. C. Ma, and W. H. Zong. "Structure and electronic properties of SiO2/Si multilayer superlattices: Si K edge and L3,2 edge x-ray absorption fine structure study". In: *Journal of Applied Physics* 92 (2002), pp. 3000–3006.

[98] X. Hao, E.-C. Cho, G. Scardera, E. Bellet-Amalric, D. Bellet, Y. Shen, S. Huang, Y. Huang, G. Conibeer, and M. Green. "Effects of phosphorus doping on structural and optical properties of silicon nanocrystals in a SiO2 matrix". In: *Thin Solid Films* 517 (2009), 5646–5652.

[99] H. Gnaser, S. Gutsch, M. Wahl, R. Schiller, M. Kopnarski, D. Hiller, and M. Zacharias. "Phosphorus Doping of Si Nanocrystals Embedded in Silicon Oxide Determined by Atom Probe Tomography". In: *to be published* (2013).

[100] S. Gutsch, A. M. Hartel, D. Hiller, N. Zakharov, P. Werner, and M. Zacharias. "Doping efficiency of phosphorus doped silicon nanocrystals embedded in a SiO2 matrix". In: *Applied Physics Letters* 100 (2012), p. 233115.

[101] O. C. Hellman, J. A. Vandenbroucke, J. Rüsing, D. Isheim, and D. N. Seidman. “Analysis of Three-dimensional Atom-probe Data by the Proximity Histogram”. In: *Microscopy and Microanalysis* 6 (2000), pp. 437–444.

[102] M. Miller and M. Hetherington. “Local magnification effects in the atom probe”. In: *Surface Science* 246 (1991), pp. 442–449.

[103] F. Vurpillot, A. Bostel, and D. Blavette. “Trajectory overlaps and local magnification in three-dimensional atom probe”. In: *Applied Physics Letters* 76 (2000), pp. 3127–3129.

[104] C. Oberdorfer and G. Schmitz. “On the Field Evaporation Behavior of Dielectric Materials in Three-Dimensional Atom Probe: A Numeric Simulation”. In: *Microscopy and Microanalysis* 17 (2011), pp. 15–25.

[105] E. Talbot, R. Larde, F. Gourbilleau, C. Dufour, and P. Pareige. “Si nanoparticles in SiO2: An atomic scale observation for optimization of optical devices”. In: *Europhysics Letters* 87 (2009), p. 26004.

[106] M. Roussel, E. Talbot, F. Gourbilleau, and P. Pareige. “Atomic characterization of Si nanoclusters embedded in SiO2 by atom probe tomography”. In: *Nanoscale Research Letters* 6 (2011), p. 164.

[107] A. L. Tchebotareva, M. J. de Dood, J. S. Biteen, H. A. Atwater, and A. Polman. “Quenching of Si nanocrystal photoluminescence by doping with gold or phosphorous”. In: *Journal of Luminescence* 114 (2005), pp. 137–144.

[108] D. Blavette, F. Vurpillot, P. Pareige, and A. Menand. “A model accounting for spatial overlaps in 3D atom-probe microscopy”. In: *Ultramicroscopy* 89 (2001), pp. 145–153.

[109] F. A. Trumbore. “Solid Solubilities of Impurity Elements in Germanium and Silicon”. In: *The Bell System Technical Journal* 39 (1960), pp. 205–233.

[110] H.-D. Chiou. “Phosphorus Concentration Limitation in Czochralski Silicon Crystals”. In: *Journal of the Electrochemical Society* 147 (2000), pp. 345–349.

[111] T. Y. Tan and U. Gösele. “Point Defects, Diffusion Processes, and Swirl Defect Formation in Silicon”. In: *Applied Physics A* 37 (1985), pp. 1–17.

[112] H. Strunk, U. Gösele, and B. O. Kolbesen. “Interstitial supersaturation near phosphorus diffused emitter zones in silicon”. In: *Applied Physics Letters* 34 (1979), pp. 530–532.

[113] R. M. Harris and D. A. Antoniadis. “Silicon selfinterstitial supersaturation during phosphorus diffusion”. In: *Applied Physics Letters* 43 (1983), pp. 937–939.

[114] P. Fahey, R. W. Dutton, and S. M. Hu. “Supersaturation of selfinterstitials and undersaturation of vacancies during phosphorus diffusion in silicon”. In: *Applied Physics Letters* 44 (1984), pp. 777–779.

[115] J. C. C. Tsai, D. G. Schimmel, R. E. Ahrens, and R. B. Fair. “Point Defect Generation during Phosphorus Diffusion in Silicon II. Concentrations below Solid Solubility, Ion-Implanted Phosphorus”. In: *Journal of the Electrochemical Society* 134 (1987), pp. 2348–2356.

[116] R. N. Ghoshtogore. “Phosphorus Diffusion Processes in SiO2 Films”. In: *Thin Solid Films* 25 (1975), pp. 501–513.

[117] A. S. Grove, O. Leistiko, and C. T. Sah. “Redistribution of Acceptor and Donor Impurities during Thermal Oxidation of Silicon”. In: *Journal of Applied Physics* 35 (1964), pp. 2695–2701.

[118] X. D. Pi, R. Gresback, R. W. Liptak, S. A. Campbell, and U. Kortshagen. “Doping efficiency, dopant location, and oxidation of Si nanocrystals”. In: *Applied Physics Letters* 92 (2008), p. 123102.

[119] M. Fujii, A. Mimura, S. Hayashi, K. Yamamoto, C. Urakawa, and H. Ohta. “Improvement in photoluminescence efficiency of SiO2 films containing Si nanocrystals by P doping: An electron spin resonance study”. In: *Journal of Applied Physics* 87 (2000), pp. 1855–1857.

[120] M. Fujii, A. Mimura, S. Hayashi, and K. Yamamoto. “Photoluminescence from Si nanocrystals dispersed in phosphosilicate glass thin films: Improvement of photoluminescence efficiency”. In: *Applied Physics Letters* 75 (1999), pp. 184–186.

[121] D. Tetelbaum, S. Trushin, V. Burdov, A. Golovanov, D. Revin, and D. Gaponova. “The influence of phosphorus and hydrogen ion implantation on the photoluminescence of SiO2 with Si nanoinclusions”. In: *Nuclear Instruments and Methods in Physics Research B* 174 (2001), pp. 123–129.

[122] A. Mimura, M. Fujii, S. Hayashi, D. Kovalev, and F. Koch. “Photoluminescence and free-electron absorption in heavily phosphorus-doped Si nanocrystals”. In: *Physical Review B* 62 (2000), pp. 12625–12627.

[123] M. Fujii, A. Mimura, S. Hayashi, Y. Yamamoto, and K. Murakami. “Hyperfine Structure of the Electron Spin Resonance of Phosphorus-Doped Si Nanocrystals”. In: *Physical Review Letters* 89 (2002), p. 206805.

[124] K. Murakami, R. Shirakawa, M. Tsujimura, N. Uchida, N. Fukata, and S.-i. Hishita. “Phosphorus ion implantation in silicon nanocrystals embedded in SiO2”. In: *Journal of Applied Physics* 105 (2009), p. 054307.

[125] T. Makimura, Y. Yamamoto, S. Mitani, T. Mizuta, C. Q. Li, D. Takeuchi, and K. Murakami. “Phosporus-doped Si nanocrystallites embedded in SiO2 films”. In: *Applied Surface Science* 197-198 (2002), pp. 670–673.

[126] V. A. Belyakov, A. I. Belov, A. N. Mikhaylov, D. I. Tetelbaum, and V. A. Burdov. “Improvement of the photon generation efficiency in phosphorus-doped silicon nanocrystals: Lambda–X mixing of the confined electron states”. In: *Journal of Physics: Condensed Matter* 21 (2009), p. 045803.

[127] E. L. de Oliveira, E. L. Albuquerque, J. S. de Sousa, and G. A. Farias. “Radiative transitions in P- and B-doped silicon nanocrystals”. In: *Applied Physics Letters* 94 (2009), p. 103114.

[128] R. N. Pereira, A. J. Almeida, A. R. Stegner, M. S. Brandt, and H. Wiggers. “Exchange-Coupled Donor Dimers in Nanocrystal Quantum Dots”. In: *Physical Review Letters* 108 (2012), p. 126806.

[129] A. J. Almeida, R. N. Pereira, and M. S. Brandt. “Exchange-coupled dopants in Si quantum dots”. In: *Applied Physics Letters* 101 (2012), p. 093108.

[130] A. Sahu, M. S. Kang, A. Kompch, C. Notthoff, A. W. Wills, D. Deng, M. Winterer, C. D. Frisbie, and D. J. Norris. “Electronic Impurity Doping in CdSe Nanocrystals”. In: *Nano Letters* 12 (2012), pp. 2587–2594.

[131] D. Mocatta, G. Cohen, J. Schattner, O. Millo, E. Rabani, and U. Banin. “Heavily Doped Semiconductor Nanocrystal Quantum Dots”. In: *Science* 332 (2011), pp. 77–81.

[132] L. E. Brus. “Model for carrier dynamics and photoluminescence quenching in wet and dry porous silicon thin films”. In: *Physical Review B* 53 (1996), pp. 4649–4656.

[133] G. Allan and C. Delerue. “Fast relaxation of hot carriers by impact ionization in semiconductor nanocrystals: Role of defects”. In: *Physical Review B* 79 (2009), p. 195324.

[134] Y. M. Niquet, C. Delerue, G. Allan, and M. Lannoo. "Method for tight-binding parametrization: Application to silicon nanostructures". In: *Physical Review B* 62 (2000), pp. 5109–5116.

[135] C. Delerue and M. Lannoo. *Nanostructures: Theory and Modelling*. Springer, 2004.

[136] P. Hapala, K. Kusova, I. Pelant, and P. Jelinek. "Theoretical analysis of electronic band structure of 2- to 3-nm Si nanocrystals". In: *Physical Review B* 87 (2013), p. 195420.

[137] M. V. Wolkin, J. Jorne, P. M. Fauchet, G. Allan, and C. Delerue. "Electronic States and Luminescence in Porous Silicon Quantum Dots: The Role of Oxygen". In: *Physical Review Letters* 82 (1999), pp. 197–200.

[138] D. König, J.Rudd, M. Green, and G. Conibeer. "Impact of interface on the effective bandgap of Si quantum dots". In: *Solar Energy Materials & Solar Cells* 93 (2009), pp. 753–758.

[139] D. König, J. Rudd, M. A. Green, and G. Conibeer. "Role of the interface for the electronic structure of Si quantum dots". In: *Physical Review B* 78 (2008), p. 035339.

[140] B. K. Ridley. *Quantum Processes in Semiconductors 4th Edition*. Oxford, 1999.

[141] J. Franck. "Elementary Processes of Photochemical Reactions". In: *Transaction of the Faraday Society* 21 (1926), pp. 536–542.

[142] E. U. Condon. "Nuclear Motions Associated with Electron Transitions in Diatomic Molecules". In: *Physical Review* 32 (1928), pp. 858–872.

[143] I. G. Austin and N. F. Mott. "Polarons in crystalline and non-crystalline materials". In: *Advances in Physics* 50 (2001), pp. 757–812.

[144] H. Fröhlich. "Electrons in lattice fields". In: *Advances in Physics* 3 (1954), pp. 325–361.

[145] P. A. M. Dirac. "The Quantum Theory of the Emission and Absorption of Radiation". In: *Proceedings of the Royal Society of London. Series A* 114 (1927), pp. 243–265.

[146] E. Lampin, C. Delerue, M. Lannoo, and G. Allan. "Frequency-dependent hopping conductivity between silicon nanocrystallites: Application to porous silicon". In: *Physical Review B* 58 (1998), pp. 12044–12048.

[147] M. Born and R. Oppenheimer. “Zur Quantentheorie der Molekeln”. In: *Annalen der Physik* 389 (1927), pp. 457–484.

[148] D. Emin. “Semiclassical small-polaron hopping in a generalized molecular-crystal model”. In: *Physical Review B* 43 (1991), pp. 11720–11724.

[149] C. H. Henry and D. V. Lang. “Nonradiative capture and recombination by multiphonon emission in GaAs and GaP”. In: *Physical Review B* 15 (1977), pp. 989–1016.

[150] P. C. Sercel. “Multiphonon-assisted tunneling through deep levels: A rapid energy-relaxation mechanism in nonideal quantum-dot heterostructures”. In: *Physical Review B* 51 (1995), pp. 14532–14541.

[151] D. Goguenheim and M. Lannoo. “Theoretical and experimental aspects of the thermal dependence of electron capture coefficients”. In: *Journal of Applied Physics* 68 (1990), pp. 1059–1069.

[152] R. A. Marcus. “On the Theory of Oxidation Reduction Reactions Involving Electron Transfer. I”. In: *Journal of Chemical Physics* 24 (1956), pp. 966–978.

[153] R. A. Marcus. “Chemical and Electrochemical Electron-Transfer Theory”. In: *Annual Review of Physical Chemistry* 15 (1965), pp. 155–196.

[154] R. Marcus and N. Sutin. “Electron transfers in chemistry and biology”. In: *Biochimica et Biophysica Acta* 811 (1985), pp. 265–322.

[155] R. A. Marcus. “Electron transfer reactions in chemistry. Theory and experiment”. In: *Reviews of Modern Physics* 65 (1993), pp. 599–610.

[156] C. C. Moser, J. M. Keske, K. Warncke, R. S. Farid, and P. L. Dutton. “Nature of biological electron transfer”. In: *Nature* 355 (1992), pp. 796–802.

[157] E. Martin, C. Delerue, G. Allan, and M. Lannoo. “Theory of excitonic exchange splitting and optical Stokes shift in silicon nanocrystallites: Application to porous silicon”. In: *Physical Review B* 50 (1994), pp. 18258–18267.

[158] E. D. German and A. M. Kuznetsov. “Outer Sphere Energy of Reorganization in Charge Transfer Processes”. In: *Electrochimica Acta* 26 (1981), pp. 1595–1608.

[159] E. German and Y. Kharkats. “Calculation of the polar media reorganization energy for the model of two dielectric spheres”. In: *Chemical Physics Letters* 246 (1995), pp. 427–430.

[160] H. Haken and H. C. Wolf. *The physics of Atoms and Quanta - Introduction to Experiments and Theory*. Ed. by Springer. Springer, 2004.

[161] J.-W. Luo, P. Stradins, and A. Zunger. “Matrix-embedded silicon quantum dots for photovoltaic applications: a theoretical study of critical factors”. In: *Energy and Environmental Science* 4 (2011), pp. 2546–2557.

[162] K. Seino, F. Bechstedt, and P. Kroll. “Tunneling of electrons between Si nanocrystals embedded in a SiO2 matrix”. In: *Physical Review B* 86 (2012), p. 075312.

[163] G. Verbeek, M. V. der Auweraer, F. D. Schryver, C. Geelen, D. Terrell, and S. D. Meuter. “The decrease of the hole mobility in a molecularly doped polymer at high electric fields”. In: *Chemical Physics Letters* 188 (1992), pp. 85–92.

[164] R. D. Stoy. “Solution procedure for the Laplace equation in bispherical coordinates for two spheres in a uniform external field: Parallel orientation”. In: *Journal of Applied Physics* 65 (1989), pp. 2611–2615.

[165] R. D. Stoy. “Solution procedure for the Laplace equation in bispherical coordinates for two spheres in a uniform external field: Perpendicular orientation”. In: *Journal of Applied Physics* 66 (1989), pp. 5093–5095.

[166] M. Razavy. *Quantum Theory of Tunneling*. Ed. by M. Razavy. World Scientific, 2003.

[167] S. Gutsch, J. Laube, A. M. Hartel, D. Hiller, N. Zakharov, P. Werner, and M. Zacharias. “Charge transport in Si nanocrystal/SiO2 superlattices”. In: *Journal of Applied Physics* 113 (2013), p. 133703.

[168] N. M. Johnson, D. K. Biegelsen, M. D. Moyer, S. T. Chang, E. H. Poindexter, and P. J. Caplan. “Characteristic electronic defects at the Si-SiO2 interface”. In: *Applied Physics Letters* 43 (1983), pp. 563–565.

[169] M. Lannoo, C. Delerue, and G. Allan. “Theory of radiative and nonradiative transitions for semiconductor nanocrystals”. In: *Journal of Luminescence* 70 (1996), pp. 170–184.

[170] M. Lannoo, C. Delerue, and G. Allan. “Nonradiative recombination on dangling bonds in silicon crystallites”. In: *Journal of Luminescence* 57 (1993), pp. 243–247.

[171] M. A. Lampert and P. Mark. *Current Injection in Solids*. Ed. by M. A. Lampert and P. Mark. Academic Press Inc, 1970.

[172] M. A. Lampert. “Injection Currents in Insulators”. In: *Proceeding of the IRE* 50 (1962), pp. 1781–1796.

[173] A. Rose. “Space-Charge-Limited Currents in Solids”. In: *Physical Review* 97 (1955), pp. 1538–1544.

[174] P. Mark and W. Helfrich. “Space Charge Limited Currents in Organic Crystals”. In: *Journal of Applied Physics* 33 (1962), pp. 205–215.

[175] M. A. Lampert. “Simplified Theory of Space-Charge-Limited Currents in an Insulator with Traps”. In: *Physical Review* 103 (1956), pp. 1648–1656.

[176] R. S. Muller. “A Unified Approach to the Theory of Space-Charge-Limited Currents in an Insulator with Traps”. In: *Solid-State Electronics* 6 (1963), pp. 25–32.

[177] H. Fröhlich. “On the Theory of Dielectric Breakdown in Solids”. In: *Proceedings of the Royal Society of London. Series A, Mathematical and Physical Sciences* 188 (1947), pp. 521–532.

[178] H. Fröhlich. “Energy Distribution and Stability of Electrons in Electric Fields”. In: *Proceedings of the Royal Society of London. Series A, Mathematical and Physical Sciences* 188 (1947), pp. 532–541.

[179] S. Marianer and B. I. Shklovskii. “Effective temperature of hopping electrons in a strong electric field”. In: *Physical Review B* 46 (1992), pp. 13100–13103.

[180] B. Cleve, B.Hartenstein, S. D. Baranovskii, M. Scheidler, P. Thomas, and H. Baessler. “High-field hopping transport in band tails of disordered semiconductors”. In: *Physical Review B* 51 (1995), pp. 16705–16713.

[181] C. E. Nebel, R. A. Street, N. M. Johnson, and J. Kocka. “High-electric-field transport in a-Si:H. I. Transient photoconductivity”. In: *Physical Review B* 46 (1992), pp. 6789–6802.

[182] C. E. Nebel, R. A. Street, N. M. Johnson, and C. C. Tsai. “High-electric-field transport in a-Si:H. II. Dark conductivity”. In: *Physical Review B* 46 (1992), pp. 6803–6814.

[183] M. A. Rafiq, Y. Tsuchiya, H. Mizuta, S. Oda, S. Uno, Z. A. K. Durrani, and W. I. Milne. “Charge injection and trapping in silicon nanocrystals”. In: *Applied Physics Letters* 87 (2005), p. 182101.

[184] T. A. Burr, A. A. Seraphin, E. Werwa, and K. D. Kolenbrander. “Carrier transport in thin films of silicon nanoparticles”. In: *Physical Review B* 56 (1997), pp. 4818–4824.

[185] J. Cai and C.-T. Sah. “Gate tunneling currents in ultrathin oxide metal-oxide-silicon transistors”. In: *Journal of Applied Physics* 89 (2001), pp. 2272–2285.

[186] V. I. Turchanikov, A. N. Nazarov, V. S. Lysenko, J. Carreras, and B. Garrido. “Charge trapping in Si-implanted SiO2-Si memory devices at high electric fields and elevated temperatures”. In: *Journal of Physics: Conference Series* 10 (2005), pp. 409–412.

[187] I. Crupi, S. Lombardo, E. Rimini, B. F. C. Gerardi, and M. Melanotte. “Location of holes in silicon-rich oxide as memory states”. In: *Applied Physics Letters* 81 (2002), pp. 3591–3593.

[188] M. Lenzlinger and E. H. Snow. “Fowler Nordheim Tunneling into Thermally Grown SiO2”. In: *Journal of Applied Physics* 40 (1969), pp. 278–283.

[189] W. Shockley. “Currents to Conductors Induced by a Moving Point Charge”. In: *Journal of Applied Physics* 9 (1938), pp. 635–636.

[190] S. Ramo. “Currents Induced by Electron Motion”. In: *Proceeding of the IRE* 27 (1939), pp. 584–585.

[191] M. D. Sirkis and N. Holonyak. “Currents Induced by Moving Charges”. In: *American Journal of Physics* 34 (1966), pp. 943–946.

[192] K. Seino, F. Bechstedt, and P. Kroll. “Band alignment at a nonplanar Si/SiO2 interface”. In: *Physical Review B* 82 (2010), p. 085320.

[193] M. Kleefstra and G. C. Herman. “Influence of the image force on the band gap in semiconductors and insulators”. In: *Journal of Applied Physics* 51 (1980), pp. 4923–4926.

[194] S. Makram-Ebeid and M. Lannoo. “Quantum model for phonon-assisted tunnel ionization of deep levels in a semiconductor”. In: *Physical Review B* 25 (1982), pp. 6406–6424.

[195] V. Karpus and V. Perel. "Thermoionization of deep centers in semiconducters in an electric field". In: *JETP Letters* 42 (1985), pp. 497–500.

[196] V. Karpus and V. I. Perel. "Multiphoton ionization of deep centers in semiconductors in an electric field". In: *Soviet Physics JETP* 64 (1986), pp. 1376–1383.

[197] D. E. Perea, E. R. Hemesath, E. J. Schwalbach, J. L. Lensch-Falk, P. W. Voorhees, and L. J. Lauhon. "Direct measurement of dopant distribution in an individual vapour–liquid–solid nanowire". In: *Nature Nanotechnology* 4 (2009), pp. 315–319.

[198] P. Pichler. *Intrinsic Point Defects, Impurities, and Their Diffusion in Silicon.* Ed. by P. Pichler. Springer, 2004.

[199] C. Jagannath, Z. Grabowski, and A. Ramdas. "Linewidths of the electronic excitation spectra of donors on silicon". In: *Physical Review B* 23 (1981), pp. 2082–2098.

[200] M. Porrini, M. Pretto, R. Scala, A. Batunina, H. Alt, and R. Wolf. "Measurement of boron and phosphorus concentration in silicon by low-temperature FTIR spectroscopy". In: *Appl. Phys. A* 81 (2005), pp. 1187–1190.

[201] K. Sumida, K. Ninomiya, M. Fujii, K. Fujio, and S. Hayashi. "Electron spin-resonance studies of conduction electrons in phosphorus-doped silicon nanocrystals". In: *Journal of Applied Physics* 101 (2007), p. 033504.

[202] K. Murakami, M. Tsujimura, R. Shirakawa, N. Uchida, and N. Fukata. "Electronic States of P Donors in Si Nanocrystals Embedded in Amorphous SiO2 Layer Studied by Electron Spin Resonance: Hydrogen Passivation Effects". In: *Japanese Journal of Applied Physics* 48 (2009), p. 081201.

[203] A. R. Stegner, R. Pereira, K. Klein, R. Lechner, R. Dietmueller, M. S. Brandt, M. Stutzmann, and H. Wiggers. "Electronic Transport in Phosphorus-Doped Silicon Nanocrystal Networks". In: *Physical Review Letters* 100 (2008), p. 026803.

[204] D. König and J. Rudd. "Formation of Si or Ge nanodots in Si3N4 with in-situ donor modulation doping of adjacent barrier material". In: *AIP Advances* 3 (2013), p. 012109.

[205] D. Vanmaekelbergh and P. Liljeroth. “Electron-conducting quantum dot solids: novel materials based on colloidal semiconductor nanocrystals”. In: *Chemical Society Reviews* 34 (2005), pp. 299–312.

[206] D. V. Talapin, J.-S. Lee, M. V. Kovalenko, and E. V. Shevchenko. “Prospects of Colloidal Nanocrystals for Electronic and Optoelectronic Applications”. In: *Chemistry Review* 110 (2010), pp. 389–458.

[207] M. L. Mastronardi, F. Hennrich, E. J. Henderson, F. Maier-Flaig, C. Blum, J. Reichenbach, U. Lemmer, C. K. and| Di Wang, M. M. Kappes, and G. A. Ozin. “Preparation of Monodisperse Silicon Nanocrystals Using Density Gradient Ultracentrifugation”. In: *Journal of the American Chemical Society* 133 (2011), pp. 11928–11931.

[208] R. N. Pereira, D. J. Rowe, R. J. Anthony, and U. Kortshagen. “Freestanding silicon nanocrystals with extremely low defect content”. In: *Physical Review B* 86 (2012), p. 085449.

[209] M. L. Mastronardi, F. Maier-Flaig, D. Faulkner, E. J. Henderson, C. Kübel, U. Lemmer, and G. A. Ozin. “Size-Dependent Absolute Quantum Yields for Size-Separated Colloidally-Stable Silicon Nanocrystals”. In: *Nano Letters* 12 (2012), pp. 337–342.

[210] D. Jurbergs, E. Rogojina, L. Mangolini, and U. Kortshagen. “Silicon nanocrystals with ensemble quantum yields exceeding 60%”. In: *Applied Physics Letters* 88 (2006), p. 233116.

[211] Y. Liu, M. Gibbs, J. Puthussery, S. Gaik, R. Ihly, H. W. Hillhouse, and M. Law. “Dependence of Carrier Mobility on Nanocrystal Size and Ligand Length in PbSe Nanocrystal Solids”. In: *Nano Letters* 10 (2010), pp. 1960–1969.

[212] A. J. Houtepen, D. Kockmann, and D. Vanmaekelbergh. “Reappraisal of Variable-Range Hopping in Quantum-Dot Solids”. In: *Nano Letters* 8 (2008), pp. 3516–3520.

[213] M. Shim and P. Guyot-Sionnest. “n-type Colloidal Semiconductor Nanocrystals”. In: *Nature* 407 (2000), pp. 981–983.

[214] J. H. Engel, Y. Surendranath, and A. P. Alivisatos. “Controlled Chemical Doping of Semiconductor Nanocrystals Using Redox Buffers”. In: *Journal of the American Chemical Society* 134 (2012), pp. 13200–13203.

[215] J. Singh. *Quantum Mechanics: Fundamentals and Applications to Technology.* Ed. by J. Singh. Wiley VCH, 1996.

[216] W. A. Harrison. "Effects of matching conditions in effective-mass theory: Quantum wells, transmission, and metal-induced gap states". In: *Journal of Applied Physics* 110 (2011), p. 113715.

[217] D. König, M. Rennau, and M. Henker. "Direct tunneling effective mass of electrons determined by intrinsic charge-up process". In: *Solid-State Electronics* 51 (2007), pp. 650–654.

List of Abbreviations

APT	atom probe tomography
C-V	capacitance-voltage
DB	dangling bond
EDX	energy dispersive x-ray spectroscopy
EELS	electron energy loss spectroscopy
EF-TEM	energy-filtered TEM
ERDA	elastic recoil detection analysis
FIB	focussed ion beam
FLY	fluoroescence yield
HF	hydrofluoric acid
HR-TEM	high-resolution TEM
ITO	indium tin oxide
I-V	current-voltage
J-E	current density vs. electric field
LED	light emitting device
MCs^+	molecular Cs^+ secondary ion mass spectrometry
MOS	metal-oxide-semiconductor
PECVD	plasma-enhanced chemical vapor deposition
PL	photoluminescence
PV	photovoltaic
SCLC	space-charge limited current
SIMS	secondary ion mass spectrometry

Si NC	silicon nanocrystal
SiO_2	silicon dioxide
SiON	silicon oxynitride
SRON	silicon-rich oxynitride
SL	superlattice
TEM	transmission electron microscopy
ToF-SIMS	time-of-flight secondary ion mass spectrometry
XANES	X-ray absorption near-edge structure
XAS	X-ray absorption spectroscopy
XPS	X-ray photoelectron spectroscopy

List of Symbols

ψ electron wavefunction . . . 7
ε energy . . . 7
T temperature . . . 9
γ N_2O to SiH_4 gas flow ratio during PECVD . . . 11
$\mathcal{E}$ electric field . . . 13
t time . . . 13
ΔV_{FB} flatband voltage measured during a C-V sweep . . . 14
Q_{eff} effective net mobile charge per unit area . . . 14
C_{ox} oxide capacitance . . . 14
q elementary charge . . . 14
$\mathcal{D}_{Si}$ diffusion coefficient of Si in SiO_2 . . . 28
c_i atomic concentration of element i . . . 36
λ_p expectation value of the Poisson distribution . . . 46
ρ atomic density . . . 46
η overlap rate arising from projection artifacts in APT . . . 48
c_i^* true concentration of element i after overlap correction . . . 48
c_i^s surface concentration of element i . . . 48
V_0 conduction band offset . . . 55
$\hbar$ reduced Planck's constant . . . 55
m effective mass . . . 55
Σ self-energy . . . 55
ϵ relative dielectric constant . . . 55
ϵ_0 dielectric constant . . . 55
U charging energy . . . 55
S Huang-Rhys factor . . . 57
$\hbar\omega$ phonon energy . . . 57
Q unified lattice coordinate . . . 56
Γ electron transfer rate . . . 58
M_{if} matrix element between initial and final state . . . 58

k Boltzmann constant ... 58
H electronic matrix element ... 58
E_a activation energy ... 58
λ reorganization energy ... 59
$\mathcal{H}$ pertubation potential ... 60
τ electron transfer time ... 62
v electron velocity ... 64
μ carrier mobility ... 65
σ conductivity ... 68
Φ electrostatic potential ... 68
n_f free carrier density ... 68
n_i injected carrier density ... 68
n_t trapped carrier density ... 68
N_C conduction band density of states ... 69
N_T trap density ... 69
N_D donor density ... 86

Publication List

Peer-Reviewed Journals

S. Gutsch, J. Laube, A.M. Hartel, D. Hiller, N. Zakharov, P. Werner, M. Zacharias, *Charge transport in Si nanocrystal/SiO_2 superlattices*, J. Appl. Phys. 113, 133703 (2013)

S. Gutsch, A.M. Hartel, D. Hiller, N. Zakharov, P. Werner, M. Zacharias, *Doping efficiency of phosphorus doped silicon nanocrystals embedded in a SiO_2 matrix*, Appl. Phys. Lett. 100, 233115 (2012)

A.M. Hartel, S. Gutsch, D. Hiller, C. Kübel, N. Zakharov, P. Werner, M. Zacharias, *Silicon nanocrystals prepared by plasma enhanced chemical vapor deposition: Importance of parasitic oxidation for third generation photovoltaic applications*, Appl. Phys. Lett. 101, 193103 (2012)

A.M. Hartel, S. Gutsch, D. Hiller, M. Zacharias, *Fundamental temperature-dependent properties of the Si nanocrystal band gap*, Phys. Rev. B 85, 165306 (2012)

A.M. Hartel, S. Gutsch, D. Hiller, M. Zacharias, *Intrinsic nonradiative recombination in ensembles of silicon nanocrystals*, Phys. Rev. B 87 (2013) 035428

A.M. Hartel, D. Hiller, S. Gutsch, P. Löper, S. Estradé, F. Peiró, B. Garrido, M. Zacharias, *Formation of size-controlled silicon nanocrystals in plasma enhanced chemical vapor deposition grown SiO_xN_y/SiO_2 superlattices*, Thin Solid Films 520, 121-125 (2011)

M. Zacharias, D. Hiller, A. Hartel, S. Gutsch, *Defect engineering of Si nanocrystal interfaces*, Physica Status Solidi A 209, 2449-2454 (2012)

J. López-Vidrier, Y. Berencén, S. Hernández, O. Blázquez, S. Gutsch, J. Laube, D. Hiller, P. Löper, M. Schnabel, S. Janz, M. Zacharias, B. Garrido, *Charge transport and electroluminescence of silicon nanocrystals/SiO2 superlattices*, J. Appl. Phys. 114, 163701 (2013)

M. Kozák, M. Kořínek, F. Trojánek, D. Hiller, S. Gutsch, M. Zacharias, P. Malý, *Hot-phonon-induced indirect absorption in silicon nanocrystals*, J. Appl. Phys. 114, 173103 (2013)

M. Kořínek, M. Kozák, F. Trojánek, D. Hiller, A. Hartel, S. Gutsch, M. Zacharias, P. Malý, *Photoexcited charge carrier dynamics in silicon nanocrystal/*SiO_2 *superlattices*, Physica E 56, 177-182 (2014)

M. Schnabel, P. Löper, S. Gutsch, P.R. Wilshaw, S. Janz, *Thermal oxidation and encapsulation of silicon-carbon nanolayers*, Thin Solid Films 527, 193-199 (2013)

Conference Talks

Transport and Doping in Si Nanocrystal / SiO_2 *Superlattices*, E-MRS Spring Meeting, NASCEnT Tutorial, Strasbourg, France, May 27-31, 2013

Non-radiative recombination in ensembles of silicon nanocrystals, E-MRS Spring Meeting, Talk D16.4, Strasbourg, France, May 27-31, 2013

Transport Regimes in Silicon Nanocrystal/SiO2 Superlattices, E-MRS Spring Meeting, Talk Y5.5, Strasbourg, France, May 14-18, 2012

Doping Efficiency of Phosphorus Doped Silicon Nanocrystals in SiO_xN_y *Matrix*, E-MRS Spring Meeting, Talk A3.6, Strasbourg, France, May 14-18, 2012

Dotiereffizienz phosphordotierter Silizium-Nanokristalle in einer Siliziumdioxidmatrix, DPG (German Physics Society) Spring Meeting, Talk HL 5.4, Berlin, Germany, Mar. 25-30, 2012

Mass Spectrometry for ALD, Oxford Instruments Workshop on Dry Processing for Nanoelectronics and Micromechanics, Talk, Freiburg, Germany, Sept. 27 – 28, 2010

Acknowledgements

I want to express my deepest gratitude to all the people who contributed to this thesis by experimental support, discussions and motivation.

First of all, I thank Margit Zacharias for continuous support and motivation in realizing my experiments and ideas, for many helpful discussions and her patience. Special thanks go to Daniel Hiller and Andreas Hartel for their extensive experimental support, the excellent teamwork and the numerous discussions. In addition, I acknowledge Rebecca Michiels, Rahul Valecha, Jan Laube for their contribution to my thesis beyond their bachelor and master theses.

I thank the following collaborators for their contribution and discussions:

- Christian Kübel from the Institute of Nanotechnology at Karlsruhe Institute of Technology for the extensive and instructive TEM sessions
- Blas Garrido Fernández, Sonia Estradé and Francesca Peiró from the University of Barcelona and Peter Werner and Nikolai Zakharov from Max-Planck-Institute of Microstructure Physics in Halle for cross-section TEM imaging
- Michael Bruns from Karlsruhe Institute of Technology for XPS measurements
- Ralph Steininger and Jörg Göttlicher from the SUL-X beamline at the synchrotron radiation facility of Karlsruhe Institute of Technology for the X-ray absorption measurements
- the IFOS team in Kaiserslautern and in particular Michael Wahl and Hubert Gnaser for SIMS and APT measurements
- Philipp Löper from Fraunhofer ISE, Freiburg, for FT-IR measurements and ITO deposition and structuring
- Hans Christian Alt from the University of Applied Sciences in Munich for the low temperature FT-IR measurements
- the cleanroom staff at IMTEK for excellent technological support

Furthermore, I thank Dirk König (University of New South Wales, Sydney), Friedhelm Bechstedt (Friedrich-Schiller-University Jena) and Christophe Delerue (ISEN, Lille) for spending their precious time on insightful discussions on theory.

The financial support of the German Research Foundation (ZA191/24-1 and 27-1) and the European Commission (FP7-245977) is gratefully acknowledged. This work was also supported by the Karlsruhe Nano Micro Facility (KNMF).

Finally, I thank my family for their enduring understanding, support and belief without reservation.

I dedicate this thesis to my girlfriend.